ThomX - Conceptual Design Report

C. Bruni, R. Chiche, R. Cizeron, Y. Fedala, J. Haissinski, M. Jacquet, D. Jehanno, M. Lacroix, L. Meignien, B. Mercier, et al.

C. Bruni, R. Chiche, R. Cizeron, Y. Fedala, J. Haissinski, et al.. ThomX - Conceptual Design Report. 2009, pp.1-136. in2p3-00448278

HAL Id: in2p3-00448278
https://in2p3.hal.science/in2p3-00448278v1

LAL RT 09/28
SOLEIL/SOU-RA-2678

THOMX
Conceptual Design Report

Editors:
A.Variola
A.Loulergue
F.Zomer

This Conceptual Design Report is dedicated to
Joseph Salomon

LIST OF CONTRIBUTORS

LAL CNRS, Université Paris-Sud 11, Batiment 200, 91898 Orsay, France:
C.Bruni, R.Chiche, R.Cizeron, Y.Fedala, J.Haissinski, M.Jacquet, D.Jehanno, M.Lacroix, L.Meignien, B.Mercier, B.Mouton, Y.Peinaud, C.Prevost, R.Roux, V.Soskov, A.Variola, G.Wormser, F.Zomer

Synchrotron-SOLEIL,Saint-Aubin, France :
P.Brunelle, M.E.Couprie, J.C.Denard, J.M.Filhol, N.Guillotin, P.Lebasque, A.Loulergue, P.Marchand, O.Marcouillé, F.Marteau, R.Nagaoka

Centre Lasers Intenses et Application, CNRS – Université de Bordeaux 1:
P.Balcou, E. Cormier, M.C. Nadeau

C2RMF-UMR171 du CNRS/Ministère de la Culture :
P.Walter

ILE, Ecole Polytechnique, CNRS, Palaiseau, France :
N. Artemiev

L.M.A. CNRS, 7, Avenue Pierre de Coubertin VILLEURBANNE, France *:*
R. Flaminio, C. Michel, L. Pinard, B. Sassolas.

THALES :
J.P. Brasile, Marie-Christine Nadeau

ESRF : European Synchrotron Radiation Facility, Grenoble 38403 France
A.Bravin, G.LeDuc

For information: variola@lal.in2p3.fr

ACKNOWLEDGEMENTS

We would like to thank S.Bielawski, P.Georges, V.Leflanchet, F.Meot, A.Mosnier, J.M Ortega, W.Scandale and M.Svanderlik for improving the text by providing valuable suggestions and remarks.

INTRODUCTION

Compton based photon sources generate a lot of interest since the rapid advancement in laser and accelerator technologies allows envisaging their utilisation for ultra-compact radiation sources. These should provide X-rays short pulses with a relatively high average flux. Moreover, the univocal dependence between the emitted photon energy and its scattering angle gives the possibility to obtain a quasi-monochromatic beam by a simple diaphragm system. For the most ambitious projects, such as the one presented here, the envisaged performances take into account a rate of 10^{12}-10^{13} photons/s, an angular divergence of few mrad, an X ray energy cut-off of few tens of keV and a bandwidth $\Delta E/E \sim 1$-10%. Even if the integrated rate cannot compete with the synchrotron radiation sources, the cost and the compactness of these Compton based machines make them attractive for a wide spectrum of applications. For example the ThomX machine design footprint fits in a 70m^2 surface (see fig.1).

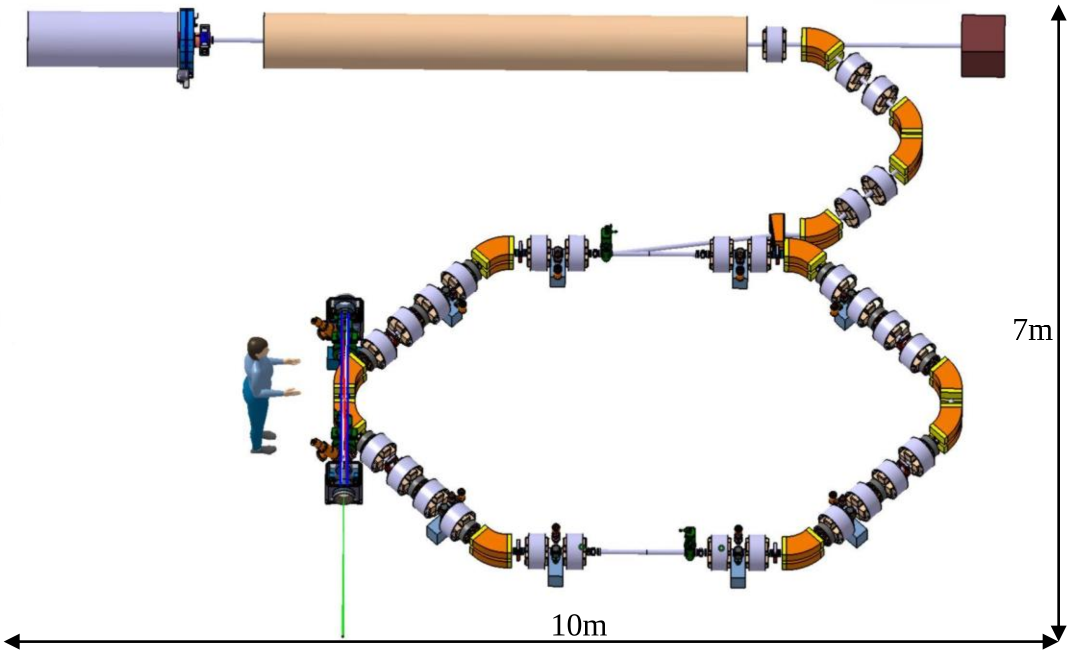

Figure 1: Footprint of the ThomX machine.

Compton compact sources are extremely interesting as far as the chemistry component analysis field is concerned. One of the most promising applications is the cultural heritage preservation and associated domains. Tuneable and highly monochromatic hard X-rays can be obtained in Compton machines with the use of diaphragms (1-10% bandwidth) or monochromators (0.1% bandwidth). Diffraction techniques, laminography and painting components chemical analysis should take advantages of such radiation sources. A great advantage should be acquired by exploiting the complementarity between the analysis worked out by employing ion sources like elastic scattering (RBS, ERDA), the use of nuclear reactions for the detection of light elements, and the hard X-Ray techniques. Heavy elements analysis, absorption spectrometry, X-ray diffraction and diffusion, tomography and phase contrast imaging will allow an important widening of the application range in the masterpieces analysis domain. To detect the interesting elements associated to the cultural heritage preservation (Mn, Co, Fe, Cu, Zn, Zr, Ag, Cd, Sb, Sn, Ba, Hg, Pb), by XANES or analysis at the absorption edge, different photon energies are necessary. They correspond to the K edge of the overmentioned metals and to the Pb and Au L_{III} threshold. This means that a photon energy ranging from 6.5 to 89 keV is necessary. The following table illustrates the required radiation performances for different analysis techniques:

	XRF	**XRD**	**XANES**	**Tomography**	**Edge enhancement**	**Phase contrast**	**Magnification**
Energy range [keV]	6.5-89	10-89	6.5-89	20-100	7-100	10-30	10-100
$\Delta E/E$	1-3%	3 – 10 %	5 – 10 %	3% bw	3 – 10 %	3% bw	3% bw
Source size				10-100 µm	10-100 µm	Very small	Very small
Size on the object	10-20 µm	10-20 µm	10-20 µm	10-50 cm	50 cm	50 cm	1-50 mm
Flux on the object [ph/s]	10^9-10^{10}	10^9 ph/s	10^7 ph/s	10^{11}	10^9	10^{11}	10^{11}
Acquisition time	1s - 5 min	1s - 5 min	30 min				
Coherence				No	No	Yes	Yes

Table 1: Requirements table for the analysis techniques used in heritage studies

So, by combining ion and photon measurement techniques on the same object, it is possible to assume that a complete material analysis will be worked out. These techniques provide precious information for the dating of the work of art, the employed techniques and the attribution [1]. Carbon detection can show the primitive sketch of the original drawing thus revealing the modifications during its realisation. Non destructive analysis of paintings permits also to reveal underlying drawings. An important synergy can be developed in integrated laboratories where physicists, chemists, art critics and historians collaborate in the same framework. Here the compactness of the Compton machine plays a fundamental role. The possibility to place such a source in an integrated laboratory gives to the expert direct access to the masterpieces in the Museum [2]. On the other side, an external facility, will involve extremely important insurance, security and transportation costs.

As far as the medical science applications are concerned an important benefit is, first of all given in the imaging field, by the development of the phase contrast method. Other applications are possible, for example, in static and dynamic imaging [3,4], 3D compressionless mammography [3,5], broncography, catheterless coronary arteries angiography [6] and in the K-edge radiography and therapy.

An important feature of Compton sources is the tunability at specific wavelength obtainable by varying the energy of the electron beam (quadratic dependence) or the wavelength of the impinging laser (linear dependence). This is attractive since a resonant reaction can be triggered by the interaction between the X rays with a determined energy, and an electronic shell of a contrast agent (like K-shell extraction with a subsequent energy release by Auger cascade). Contrast agents (like Gadolinium or Platinum) based cancer imaging and therapy [3] could represent the real breakthrough of the Compton machines in the medical field. The importance of the monochromaticity in biological tissue K-edge interactions is described in [3], where the imaging and therapy applications are illustrated.

Other interesting domains can be identified in the fields that usually operate synchrotron radiation sources but that do not need a very high average flux. A spin-off of the SLAC laboratory has created a commercial Compton source for X-ray diffraction protein crystallography [7] where performances close to the synchrotron light sources ones are attained. This is the first example of a working mini-synchrotron based on the Compton effect.

Moreover, due to the quadratic dependence of the Compton energy cut-off on the electron beam energy, it is easy to imagine harder photon production. This allows one to envisage different applications in the nuclear waste management and treatment industry [8] and in the field of nuclear isotope detection applied to infrastructures security. In this framework the atomic number identification by means of hard-X or gamma rays allows for nuclear application of the Compton scattering [9]. The high penetration power of these photons is extremely attractive when applied to security and to the radiography of shielded material. Also in this case resonant detection can be applied; one may take advantage from the relative monochromaticity degree of the photons pulses.

As one may expect, the required X-ray beam characteristics are different for different applications. Interesting rates range between 10^6 to 10^{13} photons/s. The Compton energy cut-off must vary from few keV for medical applications to the MeV range for nuclear applications. In this context one should point out that the Compton spectrum is continuous and quasi-constant (there is only a factor ~ 2 between its maximum and minimum) up to the energy cut-off (See fig. 2, Chapter 2). Therefore all the techniques requiring tunability can make use of monochromators at different wavelengths if X-ray optics is available in the explored range. Pulse length requirements can be very demanding in fast biochemistry studies (hundreds of fs range). Nevertheless other applications need to be exploited starting from the picosecond range. A general common requirement is the compactness: the main appeal of the Compton sources is to provide a high quality x ray beam from a source that can be easily hosted in a University laboratory, a Hospital, a Museum. The price is consequently strongly reduced with respect to the synchrotron sources.

Taking into account all these considerations several French laboratories [10] started to evaluate the feasibility of a compact Compton source: the project ThomX. This was the natural outcome of the different important technological results on Fabry-Perot optical resonators and fibre lasers obtained in these laboratories, and by their strong experience in design and building electron accelerators and storage rings. This allowed, as a first evaluation, to consider a prototype machine with performances at the top of the existing ones. In fact, an already financed ANR program aims to demonstrate the coupling of a high average power fibre laser with a very high finesse optical cavity. This will permit storing an incredible photon pulses average energy, in the order of 100kW-1MW. This system will be installed in the ATF ring (KEK – Tsukuba – Japan) as a demonstration of gamma factory for polarised positron production. The same system integrated in a low energy storage ring allows one to consider a very ambitious program, as far as the X Compton sources are concerned.

The ThomX French consortium is formed by different leading laboratories in the Compton associated technology. At present, accelerators systems, lasers and optical resonators are being developed by these teams reaching exceptional performances. This scenario ensures that the ThomX project should be implemented reaching the top of the actual performances in this domain.

Due to the wide spectrum of applications and requirements form different scientific communities, the ThomX project starts with a pre-defined performances range table permitting to summarize the needs in high average flux, photon energy (tens of keV), bandwidth, divergence etc etc. Moreover this prototype will allow acquiring an important experience in operating such a machine and in understanding the subtleties of the beam dynamics under Compton collision regime. Only when the specific user community requirements will be definitively defined, it will be possible to finalise the operation mode and to fine tune this complex device required performances. Table 2 summarizes the design main parameters range of the ThomX project.

Source explored range	
X energy	50-90 keV
Flux	$10^{11} – 10^{13}$ ph/s
Bandwidth	10 %
Divergence	< 2 mrad
Accelerator and laser	
Ring and injector energies	50 MeV
Charge	1 nC
Emittance (normalised rms,)	< 5□ π□ mm mrad
β^*	10 cm =>IP ~ 70□μm
Intracavity average power	> 100 kW
Compton f_{rep}	50-200 MHz

Table 2 ThomX parameters ranges

It is important to stress that Compton sources are complementary to the third and fourth generation radiation facilities since they cannot compete in integrated emitted rates and in brightness. The performances of the most ambitious backscattering sources can be placed near the first generation synchrotron sources but with more attractive characteristics (flux, directivity, monochromaticity, tunability) than other X-ray sources like, for example, X-tubes. Classical bremsstrahlung X-ray tubes can deliver typical spectral rays with a large emission spectrum and different intensities (rotating anode or microfocus tubes with adaptive optics). At present the rotating anode X-ray tubes associated to a system for X Rays optics, are the most efficient sources if a laboratory integration is taken into account. The Rigaku FR-E model with the Vari-max HF optics (Osmic distr.) and a 2.475 kW tube, provide 7.10^9 ph/s maximum flux on a 200 µm diameter surface. Nevertheless these sources do not allow developing more ambitious techniques as far as diffraction, diffusion, absorption, imaging and spectroscopy are concerned. For this reasons these techniques are commonly used only at the synchrotron radiation facilities.

In fig.2 the general X-ray sources framework is illustrated by plotting the average brightness and average emitted flux of different facilities and devices. One notices that the proposed ThomX Compton sources, ranging in 10^{10} - 10^{11} brightness, can be compared with the old generation synchrotron sources, with the great advantages that the emitted photons energy cut-off allows one to provide for much harder X-ray beams.

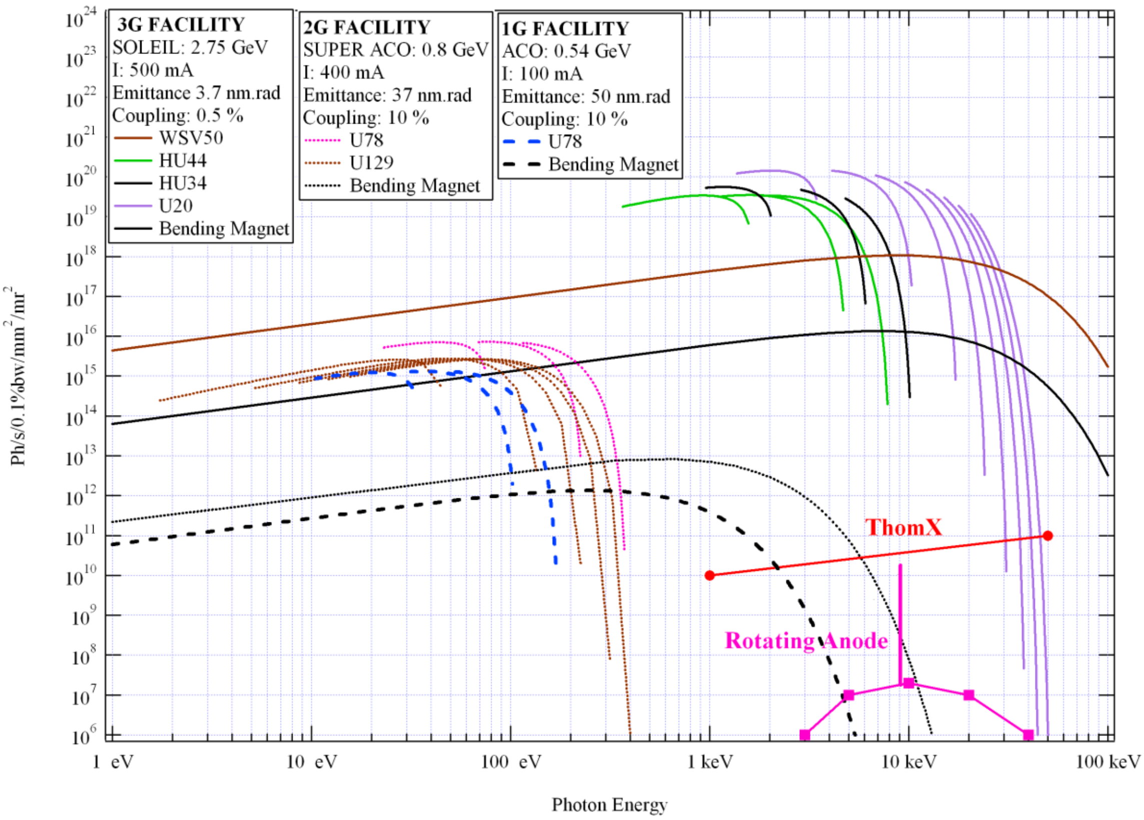

Figure 2 : The performances of different generation synchrotron radiation sources are displayed. The Compton source is also visible in the figure to highlight the high energy cut-off. The considered photon emission is provided by an electron beam of 50 MeV, respectively a factor ten, sixteen and fifty-five less than the first, second and third generation facilities. Increasing the energy of the Compton source will reduce the beam emittance at the injection. The result is an increase of the brightness as the square root of the Lorentz gamma factor.

- The ThomX working scheme

To better introduce the ThomX project a first basic illustration of its working principle is presented. Actually, Compton sources devices are based on collisions between light pulses and electron beams. Nevertheless, diverse schemes are possible depending on the required performances. In fact, subject to the applications, average or peak brilliance, monochromaticity or peak energy cut off, beam source size or emission cone are preferred. In this framework different electron and laser systems can be chosen. Electron bunches should be provided by normal or super conductive linacs, recirculated in Energy Recovery Linacs (ERL) or accumulated in storage rings. On the other hand, light pulses can be delivered by laser systems after either active or passive amplification in optical cavities.

The ThomX machine is conceived to provide the maximum average flux in a fixed bandwidth. Consequently, the basic scheme takes into account a very important collision repetition frequency and therefore the possibility to have Compton interaction in a storage ring:

Electron bunches are injected and stored in the ring and discarded in a beam dump after 20 ms.

To increase the pulse power of the light pulse the high average power laser is injected into a passive optical resonator (Fabry Perot cavity). Here the laser pulse is stacked on the pulse circulating in the cavity up to its limit given by the cavity finesse. The two systems are synchronised in a way that every turn the electron beam interacts with a laser pulse.

So, to better summarise the ThomX operation, the different working steps of the two systems are separately listed:

- Accelerator.
1) Electron bunches (~1nC) are produced in a RF gun at 50 Hz
2) A post-acceleration linac brings the electron energy to 50 MeV
3) The bunch is injected into the storage ring whose revolution frequency is 20.7 MHz
3) For 20 ms the bunch undergoes Compton collision in the storage ring
4) After 20 ms the bunch is discarded on a beam dump, and a new "fresh" bunch is injected

-Laser
1) Laser pulses are produced at 41.4 MHz
2) They are continuously injected into a four-mirror optical resonator
3) If the system is locked, the injected pulses are stacked in phase with the pulse circulating in the cavity
4) Energy amplification takes place up to the limit imposed by the mirrors losses
5) In stable regime the amplified pulse circulates in the cavity at 41.4 MHz

In a stable working condition, every turn the electron bunch impinges on the light pulse stored in the cavity with an angle of two degrees. The collision angle is imposed to allow the produced x ray beams to be extracted without damaging the high finesse cavity mirrors. Since the Fabry-Perot cavity operating frequency is a harmonic 2 of the storage ring, the operation with two stored bunches is suitable.

A sketch of the different ThomX components is shown in fig.3.

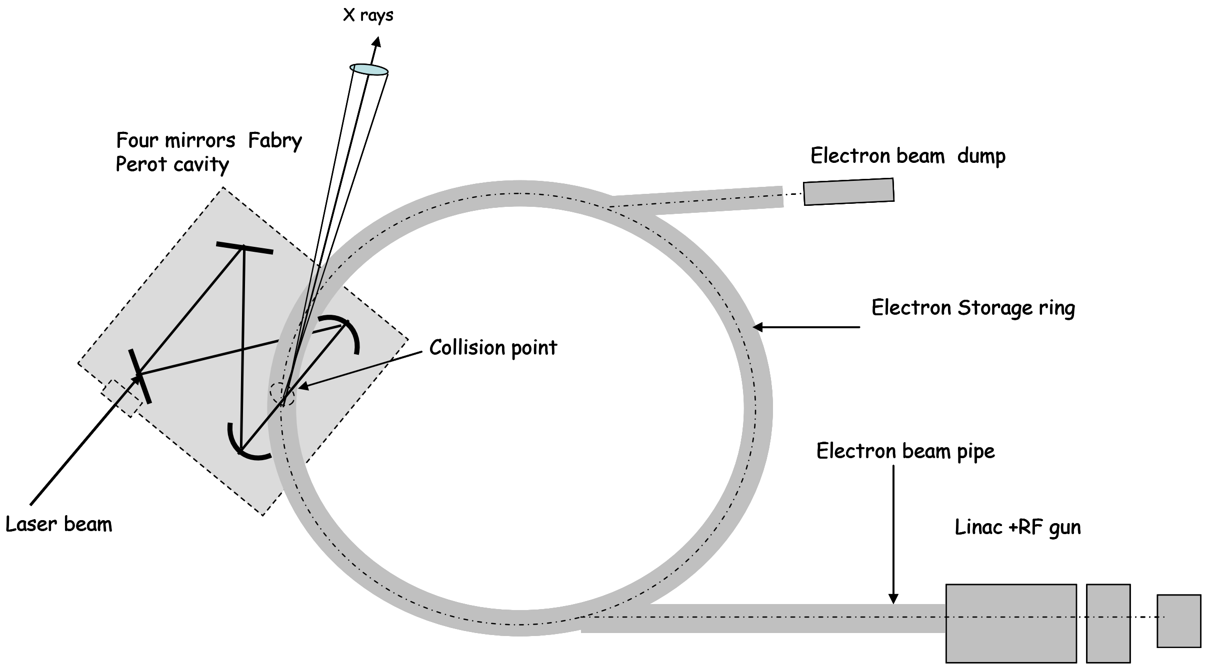

Figure 3 : ThomX different components. The electron beam is produced in the RF gun, accelerated in the linac and injected into the ring. Laser pulses are stored in the four-mirror optical resonator that is integrated in the collision region.

- *X rays sources, Compton and alternative schemes. The ThomX positioning*

As previously said Compton machines and other alternative compact x rays sources are becoming extremely attractive due to the technology advance allowing the increasing in the sources brilliance. To have a better estimation of the ThomX performances in respect to the other projects, an overview of the principal other Compton backscattering based sources is provided followed by a short description of the other possible compact devices based on bremsstralhung or on alternative radiation mechanisms.

- *Compton*

As far as the Compton sources are concerned, currently the most ambitious projects aim to produce 10^{12}-10^{13} ph/sec. The spectrum energy cut ranges in the few tens of KeV with a bandwidth of the order of 1-10%. In Table 3 an overview of the Compton compact sources projects and their main characteristics is illustrated.

	Type	Energy [KeV]	Flux (@ 10% bandwidth)	Source size (μm)
*PLEIADES (LLNL) [11,12]	Linac	10-100	10^7 (10 Hz)	18
*Vanderbilt [13,14]	Linac	15-50	10^8 (few Hz)	30
*SLAC [15]	Linac	20-85		
*Waseda University [16,17]	Linac	0.25-0.5	2.5 10^4 (5 Hz)	
*AIST, Japan [18]	Linac	10-40	10^6	30
*Tsinguha University [19]	Linac	4.6	1.7 10^4	
*LUCX (KEK) [20]	Linac	33	5 10^4 (12.5 Hz)	80
+ UTNL, Japan [21,22]	Linac	10-40	10^9	
MIT project [23]	Linac	3-30	3 10^{12} (100 MHz)	2
MXI systems [24]	Linac	8-100	10^9 (10Hz)	
SPARC –PLASMONX [25]	Linac	20-380	2 10^8 -2 10^{10}	0.5-13
Quantum Beam (KEK) [26,27]	Linac		10^{13}	3
*TERAS (AIST) [28]	Storage ring	1-40	5 10^4	2
*Lyncean Tech [29,30,31]	Storage ring	7-35	~ 10^{12}	30
Kharkov (SNC KIPT) [32]	Storage ring	10-500	2.6 10^{13} (25 MHz)	35
TTX (THU China) [33,34]	Storage ring	20-80	2 10^{12}	35
ThomX France [35]	Storage ring	50	10^{13} (25 MHz)	70

Table 3: Compact Compton X ray sources. Symbols * and + refers respectively to machines in operation and to machines in construction.

At present the experiments in operation [11,13,15,16,18,19,20,29] have already demonstrated the feasibility of X-rays production by inverse Compton scattering, but the delivered flux is not sufficient to exploit it for different applications where a higher brightness is required.

The ThomX scheme, based on the multiple electron bunches-laser pulses collisions, is the one adopted for the already working Lyncean Tech machine [29,30,31] and for all the future sources which aim to produce an high average flux [23,32,33,34,35].

Although the MIT project [23] is not based on a storage ring it is able to foresee a very important average flux and brightness thanks to the use of a very low normalised emittance (< 1 π mm mrad) superconductive linac at 100 MHz. Also the already funded Japanese project "Quantum Beam" foresees a multi-bunch electron linac impinging on a pulsed amplified laser stacking device [26,27], producing an high quality and flux X ray beam.

It is important to stress that, the only machine in operation providing a flux comparable to the first generation synchrotron machines is the Lyncean Tech one. This project started in 2002 under the direction of R.Ruth. Today the machine provides a tuneable X ray beam of

10^{12}ph/sec in 2% bandwidth [36] and the first phase contrast imaging has been recently obtained [37]

- *Other sources*

The X-ray technologies are driven by the imaging market with a trend towards high spectral brightness sources. A wide variety of technologies permit to produce X-rays but the potential alternative to Compton devices for quasi-monochromatic high flux are mainly represented by bremstralhung based sources. Therefore a lot of effort is performed to circumvent the inherent drawbacks of bremstrahlung sources, namely

- The limited flux due to thermal constraints
- The finite size of the anode,
- The angular and spectral of the X-ray beam

This has conducted to development of microfocus rotating anode with specific conditioning of the extracted beam. Rigaku [38], as an example, proposed an X-ray generator with 1.6 10^{11} photons/mm²/s (full spectrum) and possible dual wavelengths selection for phasing (chromium and copper K_α line selection at respectively 5.4 keV and 8 keV energies) also if the energy selection of the K_α line is not very efficient

The inherent thermal limitations of the interaction of the electron beam with matter have lead to two innovative designs, both connected to targets operating at higher temperature:

- A metal-Jet-Anode Microfocus X-ray source with a potential 100 factor increase in brightness [39]. This technique remains at a research stage. It uses tin metal for the liquid anode, with a K_α line of 25.3 keV, below our requirements and with the same losses for the energy selection as mentioned above
- A tungsten plasma X-ray generator [40] that provides a high instantaneous quasi-monochromatic flux at 59 keV (10^9 photons/cm² at 1 m from the source). This system is operating at present in single shot and evolution to repetitive operation remains problematic because of the plasma spread inside the tube during the shot.

MIRRORCLE [41]

Mirrorcle is based on the interaction of a high energy electron beam (up to 20 MeV), previously stored in a ring with a wire. The spectrum is therefore widespread.

The projected claimed brilliance is impressive (up to 10^{14} photons/s/mm²/mrad/0.1% BW for the 20 MeV system) but to date, the achieved level is lower (10^{11} photons/s/mm²/mrad²/0.1% BW - according to [42]. If monochromatic X-rays are requested, a monochromator can be used with the associated losses. We can assume that, at higher power, the inherent thermal limitation of the interaction between the beam and the wire target will appears

Alternative radiation mechanisms

Alternate exotic technologies, with their limitations to achieve high monochromatic flux, have been analyzed in [43]:

- Channeling radiation,
- Coherent bremstrahlung,
- Microundulator radiation,
- Parametric-X-Radiation (PXR),
- Smith Purcell Radiation,
- Transition Radiation.

Among them, PXR can, achieve both monochromaticity and tunability, but the expected flux remains low, typically 6 10^5 photons/s within a 10^{-4} sr with a 6 MeV-100µA electron beam [44]

The following Conceptual Design Report is divided in seven chapters. The first chapter concerns the project scientific case. Among the different possible applications the cultural heritage and the medical applications are highlighted. In the second chapter an extensive introduction to the Compton backscattering physics is given. The first part covers the basic concepts taking into account the collision of an electron with a photon, whereas in the second part the parameterization of the collision between an electron bunch and a laser pulse is provided in the framework of the proposed source. The third chapter describes all the optical set-up sub-systems. It illustrate the laser and the optical cavity design and integration. Then, in the fourth chapter, the design of the electron injector and transfer line and the estimation of the emittance of the injected electron bunch are given. Successively the full description of the storage ring optics, beam dynamics, instabilities and collective effects is provided together with the general description of the hardware components like the magnets, the RF system, the injection septum and kicker, the diagnostics and the vacuum system. In the fifth chapter a short description of the radioprotection requirements, associated to the machine integration, are taken into account. Other intense X-ray source configurations are considered in the sixth chapter, where the electron drive beam is provided either by a Linac or an ERL. In the last chapter a first approximate costs evaluation of the various set-up items is given allowing an estimation of the required budget.

References

[1] M. Cotte et al., Anal. Chem., 79, 6988-6994 (2007).
[2] See the Louvre laboratory web site: http://www.c2rmf.fr/
[3] Reviews of medical applications of Syncrotron radiation :
M.Ando and C Uyama, “Medical Application of Syncrotron Radiation”, Springer and Verlag (1998).
P. Suortti and W. Thomlinson, “Medical applications of synchrotron radiation”, Phys. Med. Biol. 48(2003)R1.
G. Margaritondo et al., “Synchrotron in medical and materials science technology”, Rev. Nuov. Cim. 7 (2004) 1.
[4] E.Rubistein et al. Proc SPIE 314,42,(1981).
[5] F.Carroll, Journal of Cellular Biochemistry 90 (2003)502.
[6] E.G.Bessonov et al arXiv:physics/0405003 v1 (2004).
[7] http://www.lynceantech.com/
[8] R.Hajima et al.,Proposal of Nondestructive Radionuclide Assay Using a High-Flux Gamma-Ray Source and Nuclear Resonance Fluorescence, Journal of Nuclear Science and Technology, Vol. 45 (2008), No. 5 p.441-451
[9] C.P.J Barthy and F.V Hartemann. UCRL-TR 206825, LLNL laboratory report
[10] http://sera.lal.in2p3.fr/thomx/
[11] W.J Brown et al, Phys.Rev ST-AB 7, 060702 (2004)
[12] D.J Gibson et al, Phys Plasmas 11 (2004), 2857-2864
[13] F.E. Carroll , AJR :179 (2002) 583-590
[14] F.E. Carroll et al, AJR :181 (2003) 1197-1202
[15] A.E Vlieks et al. Europen Particle Accelerator Conference EPAC04 Proceedings, Lucerne, Switzerland, (2004)
[16] S.Kashiwagi et al, J.Appl. Phys. 98, 123302 (2005)

[17] K.Sakaue et al, Rad.Phys.Chem. 77 (2008), 1136-1141
[18] K.Yamada et al, Nucl.Inst. and Meth. A 608 (2009) S7-S10
[19] C.X.Tang et al CPC(HEP&NP), 33 (2009) 146-150
[20] K.Sakaue et al, Particle Accelrator Conference, PAC 07 Proceedings, Albuquerque, New Messico USA (2007)
[21] M. Uesaka et al, Nucl. Inst and Meth. B 261 (2007) 867-870
[22] F.Sakamoto et al, Nucl. Inst and Meth. A (2009), doi 10.1016/j.nima.2009.05.089
[23] W.S.Graves et al, Nucl. Inst and Meth. A (2009), doi 10.1016/j.nima.2009.05.042
[24] See http://www.mxisystems.com/specifications.html
[25] L.Serafini, Compton Sources for x/gamma rays Workshop, Alghero Italy, 7-12 September 2008
[26] K.Sakaue et al, LINAC08 Proceedings, Victoria BC Canada (2008)
[27] J.Urakawa, FJPPL/Compton meeting / LAL Orsay, France, 1-2 December 2008
[28] H Toyokawa et al, Nucl. Inst and Meth. A (2009), doi 10.1016/i.nima.2009.05.62
[29] Z.Huang and R .Ruth, Phys. Rev.Lett 80 (1998), 976-979
[30] R.Loewen, Thesis
[31] See http://www.lynceantech.com/sci_tech_cls.html
[32] E.Bulyak et al, Nucl.Inst. and Meth. A 487 (2002) 241-248
[33] C.X Tang et al, Nucl.Inst. and Meth. A 608 (2009) S70-S74
[34] P.Yu and W.Huang, Nucl.Inst. and Meth. A 592 (2008) 1-8
[35] C.Bruni et al, Europen Particle Accelerator Conference EPAC08 Proceedings Genova, Italy, (2008)
[36] J.Rifkin, POSIPOL workshop 2007, LAL Orsay France, 25-25 May 2007
[37] M Beck et al, J.Synchrotron Rad. 16 (2009) 43-47
[38] Rigatu FR-E+SuperBright ™
[39] A Compact High-Brightness Liquid-Metal-Jet X-Ray Source
[40] K-edge angiography utilizing a tungsten plasma X-ray generator in conjunction with gadolinium-based contrast media, E Sato & als, Radiation Physics and Chemistry 75 (2006) 1841-1849
[41] MIRRORCLE-6X - Photon Production Laboratory, Ltd.
[41] High Resolution X-Ray Imaging by Portable Synchrotron Radiation Source", MIRRORCLE - 6X, Yamada et al
[43] Exotic sources for iodine K-edge angiography - Roger Carr SLAC-PUB-634
[44] Tunable Source of Parametric X-Ray Radiation A.S Gogolev & A.P. Potylitsyn, ISSN 1063-7842, Technical Physics, 2008, Vol. 53, No 11

CHAPTER 1: Scientific Case

1.1] Cultural Heritage Applications

1.1.1] Introduction

Nowadays the cultural heritage plays a crucial role, as far as the quality of the surrounding environment and the attractiveness of France are concerned, and has significant economic effects in many fields. The public at large takes great interest in it, as testified by the high number of visitors flocking to the many French monuments and museums. Consequently, knowing one's cultural heritage and preserving it in order to hand it over to future generations, is an increasingly important and shared concern in every country, especially those belonging to the European Union. At present in France all levels of society - government, regions, municipalities and companies - are involved in this effort.

Therefore the need was felt to carry out fundamental and applied research in order to best preserve this heritage and allow the public to access as many works of art as possible and learn about their history. This situation was described in the parliamentary report assessing the scientific and technological decisions on restoration techniques of works of art and the conservation of the national heritage [1]. On the one hand, in order to make progress in unveiling the history of works of art and in archeology it is necessary to identify the materials used; on the other hand, when conserving and restoring artifacts the effects of the aging of the materials cannot be neglected. To this end, the methods commonly used in materials science can prove extremely useful, especially those enabling researchers to perform a non-destructive analysis directly on the works of art or on tiny samples.

Research work on materials characterization is a big challenge from an analytical point of view, since there are many materials, they are often available in very small quantities, they have been processed or synthesized and then used by man, they have deteriorated in the natural environment or in the buildings in which they have been kept (museums, libraries, historical monuments, etc.). This is the case for paintings and graphical documents made up of various layers including mineral and organic ones (pigments, colorings, inks, binders, etc.): the chemical interaction between the different elements results in specific change or deterioration over a very long time. It is therefore necessary to develop and implement a number of innovative techniques to analyze works of arts.

A wide variety of instruments is commonly used. Most of them are classical laboratory techniques, whose set enables to probe samples at different levels (atomic, molecular, structural), at different scales (from millimeters to nanometers), and with different sensitivities (major to trace elements). Although lab instruments become more and more powerful and remain the prime equipment for the study of Cultural Heritage objects, two recent evolutions can be underlined. On the one hand, the necessity of reaching sites (excavation sites, museums, monuments…) fostered the development of portable instruments enabling *in-situ* analyses. On the other, specific studies require higher level of performance and are only possible on large-scale facilities (ion beam "microprobe" accelerator such as AGLAE in the Louvre, synchrotron radiation, neutron sources) which provide brighter and smaller spots.

For this reason the setting-up of a “micro-probe”particle accelerator on the Louvre premises in late 1988 was a major step in the development of this research work. It made possible to investigate the composition of the museum’s works of art directly, with a 20-30 µm spatial resolution which was ideal to study very complex and heterogeneous materials [2]. Today AGLAE is a unique and powerful analytical tool for the characterization of the materials of the museums’ works of art and available to foreign researchers in the framework of a EU-financed program.

The AGLAE2 project aims at developing a new tool for the direct analysis and imaging of works of arts and archaeological items thanks to the co-localization of the present ion accelerator and a very intense X-ray source in a laboratory specialized in “non-invasive” analysis of works of art to be set up in the Louvre security area.
These two sources will make it possible to develop additional analysis and imaging methods which would pave the way for the development of a new tridimensional analytical method of the museums’ works of art to be combined with materials science methods. This could mark a radical change in what we know about works of art thanks to much more accurate scientific imaging. This device would be very useful for museums as it would be strategically positioned inside the Louvre. There would therefore be no cost constraints and no danger resulting from the need to move the museum’s most precious works of art, namely Louvre’s paintings, drawings and art objects.

1.1.2] Expected scientific impact

1.1.2.1] Analytical methods

Nowadays, the main research activities carried out in the laboratories working in the Cultural Heritage field focus on the identification of materials from a chemical and structural point of view (mineral, organic, hybrid, condense matter), the study of processes used for the elaboration of the works of art (origin of the materials, recipes of chemical synthesis, metallurgy, mechanical treatments and thermal annealing) and the study of alteration and ageing behavior, including the issues concerning the preventive conservation and the restoration. The ancient materials may be of natural origin, such as the gemstones, or stem from an artificial preparation at high temperature (glasses, ceramics and metals), or by wet chemistry, for the synthesis of pigments or pharmaceuticals for instance. Other materials have plant or animal origins, such as residues found in vases, sculptures made of wax, and human remains. Sometimes, it is the understanding of a diffusion mechanism, the observation of a patina on metals or the nature of nanocrystallized inclusions which are the purpose of the researches.

These activities require developing specific and appropriate physico-chemical analytical methods for the study of the cultural heritage masterpieces. The following table illustrates the techniques as far as painting is concerned [3]. It is possible to highlight the importance of applying a combination of different techniques to detect the underlying nature of the materials employed by the artists. Another important aspect of differentiation is that whereas in certain techniques a sample must be taken, the others allow for an in-situ analysis of the objects of art.

Technique	Probe			Probe Size	Sensibility	Invasive?	Portable?
	Atomic	Molecular	Structural				
FTIR		+++	+	+	+	No	Yes
Raman		+++	+	+++	+	depends	Yes
SEM-EDS	+++		+	+++	+	Yes	No
EPMA	+++			+++	++	Yes	No
PIXE-XRF	+++			++	+++	depends	No
XRF	+++			+	+	No	Yes
XRD			+++	+	+	No	Yes
SIMS	+++	+++		+++	+	~No	No
SR-µ-FTIR		+++	+	+++	+	No	No
SR-µ-XRD			+++	+++	+++	No	No
SR-µ-XRF	+++			+++	+++	No	No
µ-XANES		+++	++	+++	+++	No	No

Table 1: summary of classical and emerging techniques used for chemical analysis of ancient paintings.

The integration of a high flux monochromatic X-ray source, complementary to AGLAE, will provide a unique opportunity to have at one's disposal methods for non invasive elementary and structural analysis. A 20µm resolution, similar to that currently attained in AGLAE, is particularly well suited to the non-invasive study of ancient materials that often represent complex and heterogeneous samples.

Such an instrument should solve many problems in the context of different scientific cases. The ion beams are unique for the detection of light elements and the measurement of concentration gradients by nuclear reactions and also by elastic scattering (RBS and ERDA). Hard X-rays offer the opportunity to analyze heavy elements with high accuracy, to explore their environment by absorption spectrometry and to better understand the material organization by X-ray diffraction or small angle X-ray scattering (SAXS). By combining these two measurement categories on the same object, it is possible to assume that a "*total analysis of the material*" will be worked out. This will remove any ambiguity in the interpretation of their nature in all the possible cases, independently from the metal, crystalline or amorphous nature of the sample.

1.1.2.2] X-ray imaging based on different physical properties

The use of radiography for the study of museum masterpieces has developed very rapidly after the discovery of X-rays by Röntgen in 1895. Today, C2RMF has 5 conventional radiography devices on the Louvre site. In the case of paintings, radiography provides information on the artist's techniques, the primitive draft variations, the paint overlays, and the conservation of the work. It reveals, for example, cracks in the paint layer. But the interpretation of the work of arts is much more than a mere conservation status analysis; it falls into the depths of the personality of the artist and sometimes shows the path of an artist toward its work creation. Radiography is very important to characterize objects, in particular in view of their restoration and to better understand the internal structure, i.e. the inhomogeneities (earth, plaster, bronze, inclusions, and bubbles), the formatting procedures (hammering, casting, lost wax or reversed ...), the assemblies, the alterations and the restorations.

An X-ray monochromatic intense source offers the opportunity to develop some techniques for three-dimensional imaging analysis of works of art aiming to a "*perfection level in direct imaging techniques*": combining other imaging techniques in the visible, UV and near IR ranges, it will allow providing a new scientific imaging report on each studied artefact, from the surface to the heart of the matter, with a spatial resolution of recording up to the micrometer scale. These scientific records will complement the documentation about its provenance and its historical and cultural environment.

The possibility of using a point source, monochromatic and coherent X ray beam makes it possible to consider different approaches:

(1) Absorption Tomography

This technique, commonly used in medicine, shows a fast development in the recent years. However, to provide the access to high quality of reconstruction and to quantitative data, an excellent signal to noise ratio is essential. It allows rapid data acquisition at very high spatial resolutions, resulting in precise mapping of the internal structures of the artefact. The use of an intense monochromatic beam is also preferable to conventional X-ray tubes because it avoids beam hardening effects that are frequently strong.

This technique is hardly used when dealing with objects almost flat, such as paintings: in this case the X-ray laminography technique should be used.

(2) Distribution of specific chemical elements analysis:

The edge-enhancement imaging technique is based on the same principle as the angiography of blood vessels in medicine. It is considered that each chemical element, with enough quantity in the work of art, may serve as a contrast agent when imaging with different X-ray energies. In medicine, ions are usually injected the vascular system. On the other side, as far as the paintings are concerned, lead, tin and mercury are characteristic of the different employed pigments. Therefore these images will map the spatial distribution of the chemical element. In practice, two images on each side of the K (or L) atomic absorption edge are measured. This technique and the resulting quantitative measurements can provide new information on the artists painting methodology: the substructure of a painting provides insight into the genesis of the object. Underlying layers may include the underdrawing, underpainting and modifications to the original sketch. In a growing number of cases conservators have discovered abandoned compositions on paintings, illustrating the artists' practice to re-use a canvas or panel and paint new compositions on top of existing ones. A painting from Vincent Van Gogh has been recently revealed by synchrotron-based XRF mapping [4].

(3) the phase contrast:

An inverse Compton scattering source should allow developing techniques of phase contrast imaging. These present the important advantage of the contrast enhancement in the case of low density materials. This is possible since the acquired image records the phase variations of the electromagnetic wave that occur when a variation of the refractive index occurs. The interest of this technique has been demonstrated on fossils in paleontology and on amber samples [5].

(4) magnification:

When the X-ray source sizes are very small and the emitted radiation sufficiently divergent (conical beam), it is possible to obtain a geometric magnification factor of the image by moving the detector away from the object. Thus, the projection of the object image is magnified, allowing a better accuracy in detecting details.

Other approaches could also be useful (Diffraction enhanced imaging, holo-tomography, X-ray grating interferometry, etc.).

We see therefore that the installation of a new X-rays source, simultaneously coupled with visible imagery, will provide useful data for the study of the paintings and the archaeological objects. Obtaining images of the surface and the core of the work of art, with spatial resolutions of the order of micrometers, is expected to provide to the researchers the access to digital reconstructions, with a much easier access than the original works. This will avoid to endanger the conservation of museum pieces particularly fragile: human rests and bones, wood or ivory masterpieces of the prehistoric era from the Musée de l'Homme, the National Museum of Prehistory and the National Archaeological Museum, the objects of ancient or medieval art from the Louvre Museum and the National Museum of the Middle Ages, etc.

1.2] BioMedical Applications

Biomedical applications of synchrotron radiation have been developed at Hasylab (Germany), Photon Factory (Japan), ELETTRA (Italia) and at the ESRF (France). Despite the fact that there are only a few dedicated beamlines in the world (two new ones are under construction at the Australian and Canadian synchrotrons), medical research is carried out in almost all synchrotron facilities through preclinical and clinical research protocol.

1.2.1] Radiotherapy programs

Gliomas are among the most frequent primary brain tumors in adults, with an incidence of approximately $(5–11)/10^5$ in industrial countries [6]. This pathology constitutes a major health problem. The treatment of high-grade gliomas is palliative rather than curative, despite a combination of surgery, chemotherapy and radiotherapy. Gliomas are extremely radioresistant, while surrounding normal tissues remain radiosensitive, especially in infants. The fundamental goal of radiation therapy is to deliver a high therapeutic dose of ionizing radiation to the tumor without exceeding normal tissue tolerance. This limitation is particularly severe in the case of brain tumors because of the high risk of adverse normal tissue morbidity. The needs, in particular for radioresistant tumours, are particularly high and may require very large facilities. For example, hadrontherapy [7] uses the enhanced energy deposition in the Bragg peak to achieve good conformity of the dose to the target, while sparing the healthy tissues. The main drawback of such large systems is the cost (in the range of 100 M€) and the accessibility.

At the ESRF, two radiotherapy techniques were developed, namely

- the Microbeam Radiation Therapy (MRT) and
- the Stereotactic Synchrotron Radiation Therapy (SSRT)

and clinical trials are foreseen to start in few years.

The Stereotactic Synchrotron Radiation Therapy (SSRT) consists in irradiating a tumour loaded with a contrast agent with quasi-monochromatic X-rays tuned at the energy above the K_α line of the contrast agent. The requested bandwidth is not a tight constraint and is naturally achieved with Inverse Compton Scattering without the need of a monochromator. The increase in the absorbing properties of the tumour relative to the surrounding tissue results in an internal dose enhancement based on the photoelectric effect as shown in fig.1**.** The photoelectric interactions generate photoelectrons, X-ray fluorescence and Auger electrons with the consequent cascade, which in turn increase the local radiation dose. In the energy range of medical imaging (15–120 keV), the photoelectric effect plays a dominant role. As it displays a Z^3-dependency, where Z is the atomic number, heavy elements absorb X-rays more strongly than the biological tissue light elements. This technique can be slightly optimized by loading the tumour with cis-platinum (cis-diamminedichloroplatinum or CDDP).The X-ray beam will induce a dose enhancement due to the high Z value of Pt in parallel with direct DNA damage as the chemotherapeutic effect of CisPt [8,9]

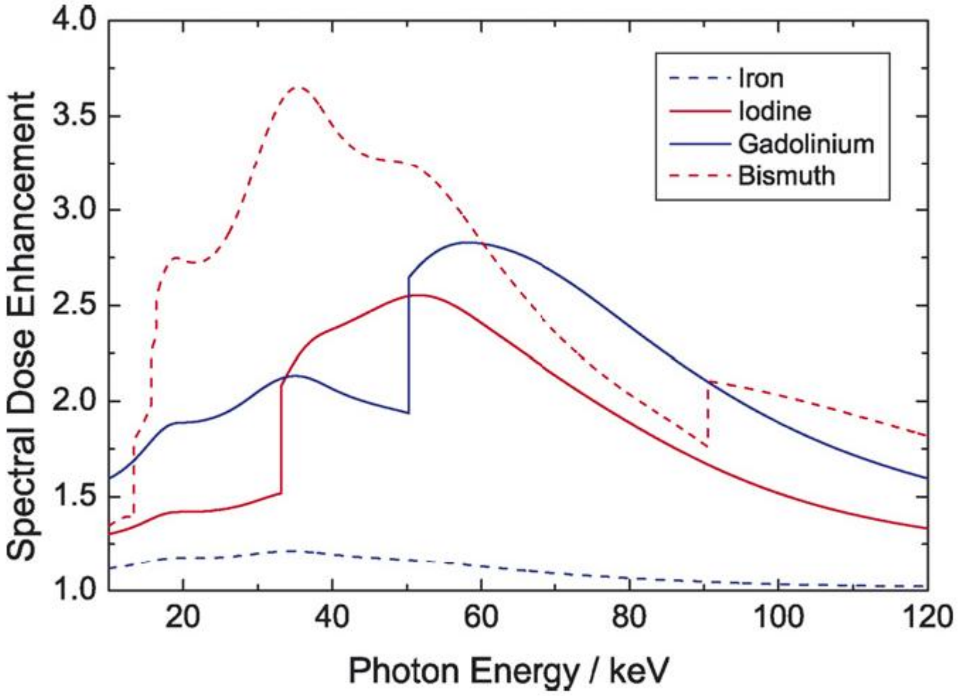

Figure 1: Dose enhancement versus X-ray energy for various contrast agents

In SSRT, the best survival curves were obtained by Biston et al. [8]. The brain tumor bearing rats were first inoculated with cisplatinum and then irradiated with X-rays of 78.8 keV. Median Survival Time (MeST) of untreated rats was 26 days. When cisplatin or SR alone was applied, the MeST was found to be 37 and 48 days, respectively, while when both treatments were combined, a very large increase in life span was obtained (MeST = 206.5 days) compared to the controls. One year after treatment, 6 out of the 18 rats treated cisplatinum and radiation were still alive and cured. This is the largest life span increase obtained to date with this particular glioma model.

The Microbeam Radiation Therapy (MRT) [10] is an alternate approach for treating tumours and neurological disorders. It uses arrays of parallel, thin microplanar beams with two noticeable effects (fig. 2):

- single exposure MRT largely spare normal tissues including normal eyes, brain, spinal cord, and skin in spite of using an in-beam dose up to 20 times larger than those tolerated in broad beam radiotherapies,
- single exposure unidirectional MRT ablates intracerebral gliosarcomas in rats at an in-beam dose tolerated by contiguous normal tissues.

Experiments performed at the ESRF and BNL on the brains of adult rats, suckling rats, duck embryos and piglets have confirmed the sparing effect on normal tissues when using microbeams. In parallel, it was shown that MRT protocols can ablate highly aggressive

tumors like 9L brain gliomas, EMT-6 carcinoma and SCCVII carcinoma in animal models. Smilowitz et al. (2006) obtained 44% of longterm survivors (>300 days) in brain tumor bearing rats by combining MRT (entrance dose 625Gy, 50 microbeams, 25µm wide and 200 µm spaced) and gene mediated immunoprophylaxis. Furthermore, rats irradiated with MRT alone exhibited 20% long-term survivors [11].
This technique requests high flux density and high brightness beams that can only be provided by 3rd generation synchrotron to deliver very high doses (several hundreds of Gy) in an array of spatially fractionated quasi-parallel microbeams (25-75µm wide and spaced 100-400µm on-center). The 3rd generation sources are characterized by an adequate dose rate and energy spectrum which allows a minimal divergence of microscopic beams and consequently, the preservation of the steep gradients dose between parallel microbeams. ICS sources (as they are presently described) are below 3rd generation source flux by a factor of 100 approximatively. Present ICS source do not exhibit characteristics that are adequate for clinical trials, due to the fact the lack of flux will slow down the irradiation and increase the risk of blurring effects of the microbeams. However, ICS source could be used for performing MRT preclinical experiments on cells and animals as it is performed at the National Synchrotron Light Source (Brookhaven, National Laboratory, USA).

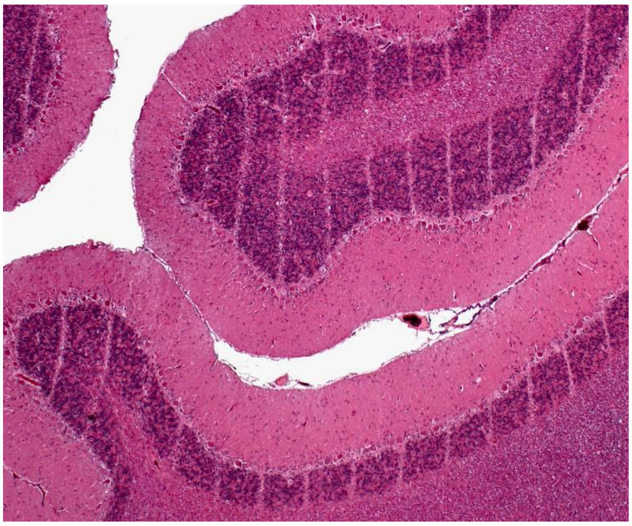

Figure 2: H&E staining of the horizontal section of piglet cerebellum, ≈15 months after irradiation (skin entrance dose: 300 Gy), 25 µm width. The microbeam paths are clearly visible although the piglets had a normal survival and no neurological signs or deficits.

1.2.2] Imaging

For imaging, it is necessary to avoid current radiograms that use 5-75 keV bremsstrahlung imaging, since the lowest energy part of the spectrum provides skin dose and no contrast while the highest part induces tissue dose and low contrast. Furthermore the traditional absorption imaging is very poor in differentiating soft tissues. Better in vivo systems need X-ray beams with the following characteristics (i) delivery of a very low integral dose and skin dose as small as possible (ii) high spatial resolution and in the same time high temporal resolution due to in vivo constraints (i) assess to quantitative information mimicking physiopathology or any functions of an organ. Among the techniques developed in synchrotron facilities, 2 of them have noticeably contributed to the biomedical field.

The K-edge digital subtraction imaging (KEDSI) method utilizes the sharp rise in the photoelectric component of the attenuation coefficient of a given element at the binding energy of the K-electron (e.g. 33.17 keV for I, 34.56 keV for Xe, 50.25 keV for Gd). Depending on the specific needs and constraints, experiments can be carried out either using two beams of energies bracketing the K-edge or by a single beam set at energy above the K edge. In the first case, the technique is indicated as “energy subtraction” and the map of the contrast agent concentration is obtained by logarithmically subtracting the two energy images; In the second case, indicated as “temporal subtraction mode,” the map is obtained by logarithmically subtracting the images taken at an energy above the K-edge, before and after the injection of the contrast agent. This latter modality is used when dealing with fixed samples and when the signal to noise ratio should be the best possible (brain imaging) [12]. Experiments have been performed in order to understand the uptake of Gd contrast agents in hepatitis-affected livers and in brain tumor-bearing animal models. In the frame of the radiotherapy programs, investigations have been carried out to optimize the delivery of drugs such as iodine, platinum, gold and/or gadolinium nanoparticles after intravenous of intracerebral delivery [13], in order to follow up their biodistribution and to study the tumor filling. From concentration maps of the contrast agent, brain perfusion parameters such as the cerebral blood volume and permeability can be derived using perfusion models [14](fig. 3).

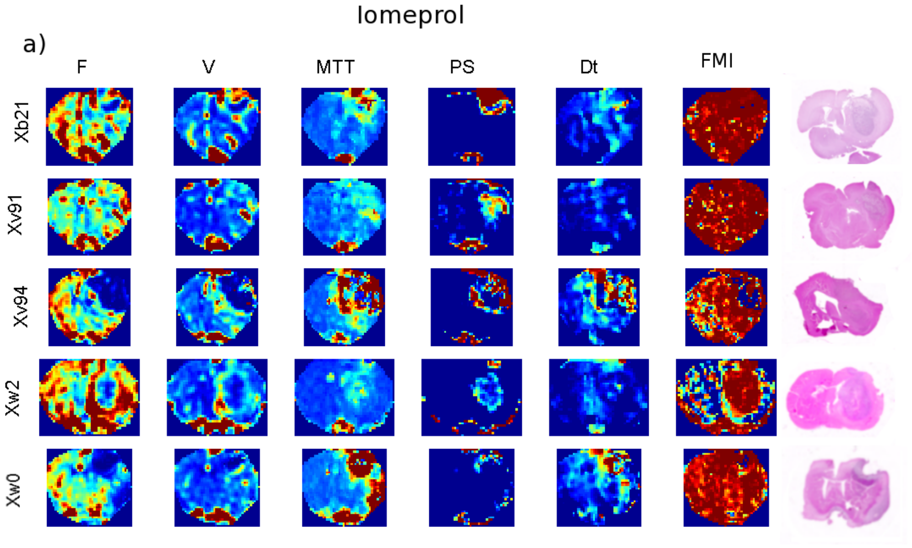

Figure 3 : Microvascularization parametric maps, reliability maps (FMI maps) and H&E staining anatomic sections obtained in 5 rats brain bearing gliomas after iomeprol injection. The color scale for each parameter the red corresponds to high values and the blue to low values. In the FMI maps, a red pixel has a value of 1, attesting an excellent reliability of the model adjustment.
Left: physiological maps (blood flow F_T, blood volume fraction V_T, mean transit time MTT, permeability surface product PS, and time delay D). *Middle*: reliability criteria FMI. *Right*: H&E staining (the labels on the right are the names of the rats).

To date, the KEDSI technique is the only one permitting the *in vivo* access of any drug concentration (if labeled with a high Z element such as Gd, I , Xe, Lu…) with such a spatial and temporal resolution.. This technique is of great interest for all laboratories (chemistry, pharmacy) who intend to characterize drugs and to study their bio-distribution.
Alternatively, the phase contrast imaging technique based on the recording of the phase variations occurring when X-rays pass through matter, has been demonstrated as an extremely powerful method since it permits contrast resolution of soft tissues (even if the elemental composition is almost uniform and the density variations are small) with far lower absorbed

dose levels than with conventional system as shown. This is in particular the case of breast, lung and articular cartilage tissues. Among the technique used on synchrotron beamlines, phase shifts are revealed by (i) using a crystal analyzer in order to depict the diffraction component (Analyser Based Imaging ie ABI)[15], (i) using the grating interferometry principle [16] (fig. 4) , as well as propagation phenomenon.

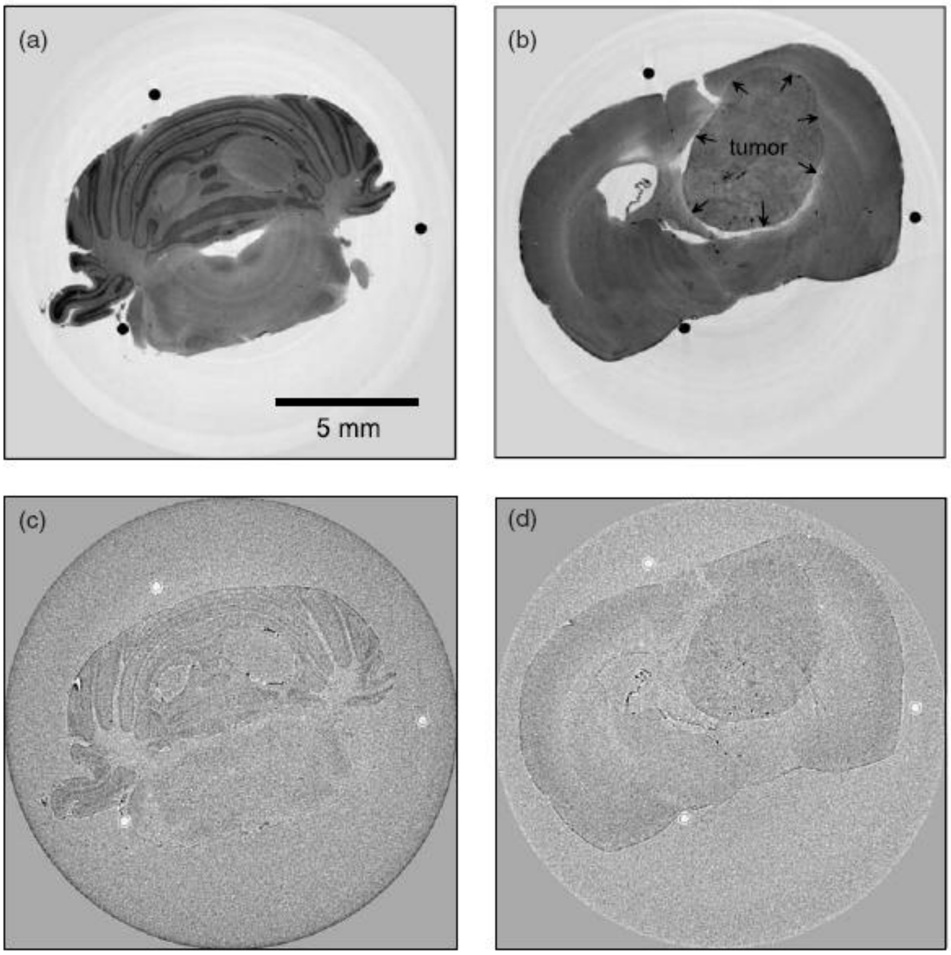

Figure 4 : Phase and attenuation-based tomography results. (a) Phase tomography slice through the rat's cerebellum showing a clear contrast between the white and gray brain matter. (b) Slice through a region of the brain containing a tumor (arrows indicate the tumor's 'pushing front', the border between the tumor-invaded and healthy brain tissue). (c) and (d) Corresponding slices through the absorption-based reconstruction of the specimen. All images are displayed on a linear gray scale corresponding to ±2σ, where σ is the standard deviation of the pixel gray values in the image.

In the ABI technique, the X-rays transmitted through a sample are analyzed by a perfect crystal. The small angular acceptance of the analyzer permits the observation of the very small refraction angles (typically less than one microradian), to suppress scattered radiation and thereby increases the signal to noise ratio. The edge enhancement, which is characteristic of this method, occurs at the interfaces of regions with different refractive indices. The effects of refraction are converted to intensity variations by slightly detuning the analyzer away from the maximum of the reflectivity curve. The correlation of the radiographic findings with the morphologic changes in specimens analyzed in histo-pathological sections has been unequivocally confirmed. These advances in image quality make ABI a very promising candidate for clinical mammography at table top sources. In the case of osteoarthritis diagnosis, a poorly understood disease that can affect the cartilage and other tissues in the joints of aging people, conventional radiography (including CT and MRI) is sensitive only in cases of advanced disease in which there has been a loss of cartilage. Measurements have been performed on human articular specimens. Cartilage defects, even at early stages of development, have been studied at 18 and 30 keV and compared with the absorption technique and show a clear, early visualization of the damage [17]. In addition, experiments were performed in rabbits and sheep samples with model implants to evaluate ABI as a tool in bone-implant research. AB images allow the identification of the quality of ingrowth of bone into the hydroxyapatite layer of the implant through the visualization of a highly refractive edge at the implant/bone border. Implants with bone fully grown onto the surface did not display a refractive signal.

1.2.3] Conclusion for medical applications

The SSRT technique seems to be fully compatible with ICS, since it can provide a flux and a brightness high enough together with a tunable quasi-monochromatic X-rays. The same prototype could serve both therapy and imaging since SSRT is derived from KEDSI method. These applications appeared to be the easiest ones to be developed in a first step. There techniques are also techniques where the synchrotron community has already a lot of knowledge and experience.

Regarding the MRT technique, although the flux is not sufficient enough for the realisation of clinical trials, an ICS source could be used anyway for preclinical studies.

Finally, the Inverse Compton Scattering process permits to provide high phase contrast and DEI imaging of soft tissues (adequate with its few percent bandwidth) on moving organs (because of its high available flux). The clinical interest of these techniques has to be however confirmed by in vivo measurement and several protocols are currently going on in other synchrotrons or with other synchrotron compact sources.

1.3] X-ray crystallography

The knowledge of the atomic structure of macromolecules such as proteins leads to a better understanding of the chemical reactions which take place in living organisms, how proteins are produced and how genetic information is forwarded.

1.3.1] Protein structure determination

Structure determination of proteins allowing a resolution at the level of distinguishing individual atoms is accomplished by two techniques: X-ray diffraction and Nuclear Magnetic Resonance (NMR) [18]. The NMR technique measures distances between atoms within a molecule in solution. Its principal advantage is to work on molecules in solution allowing a dynamic study to be performed. The complexity of the spectra for large molecules makes the analysis very difficult and protein size is the main limitation of the NMR technique. X-ray crystallography makes use of the diffraction pattern of X-rays that are shot through an object. The pattern is determined by the electron density within the crystal and this technique has no protein size limitation. It can solve structure of large and complex molecules but however requires proteins to be in an ordered crystal. Protein crystallization is inherently difficult due to the fragile nature of protein crystals and it is difficult to obtain a crystal with a suitable size (few hundred microns) for diffraction experiments [19]. For some proteins crystallisation, experiments will only ever produce extremely tiny crystals of the order of a few microns.

Since the average intensity of a diffraction peak for a crystal volume V and unit cell volume Vc in a beam of intensity I is approximately proportional to I(V/Vc), a thousand-fold increase in beam intensity is required to obtain the same strength diffraction from a 10 micron crystal compared to a 100 micron crystal. So, especially in case of complex structure determination, focused brightness X-ray beams are necessary to obtain sufficient resolutions [20]. The current intense synchrotron sources can provide the three-dimensional structure of small as well as large proteins with a precision of the order of the angstrom [21].

In a diffraction experiment, only intensities and diffraction angles of the diffracted beam are measured. To recover information about the phase of the diffracted beam which is essential for the solution of crystal structures, protein crystallography requires also a tuneable frequency X-ray source for the multi-wavelength anomalous dispersion (MAD) phasing technique [22]. High intensity polychromatic X-ray beams of the third generation synchrotron radiation sources are currently the most suited for protein structure determination.

1.3.2] System dynamic studies

A precise knowledge of a protein functioning requires the knowledge of its tree-dimensional structure but also its structural changes and its dynamic when the molecule is in activity. X-ray experiments make it possible to have access the timescale of molecular processes with a resolution in the picosecond range. Radiations from synchrotron sources have made it possible to conduct pump and probe experiments on chemical and biochemical systems down to a time-resolution of 50-200 ps. Pump and probe experiments consist to photolize a protein crystal sample with a femtosecond laser flash after which a probe time-delayed X-ray pulse provides diffraction data from excited molecules. The pump and probe sequence has to be repeated many time to build up sufficient signal to noise ratio for each diffraction pattern, to obtain patterns at different crystal orientations and at different pump-probe delays to access the time dimension of the process. The brightness and the pulse length of synchrotron source beams make possible the study of these time-dependant phenomena and allow to progress in the understanding of how proteins function [23, 24].

1.3.3] Compact Compton based source for protein study

A compact Compton based X-ray source would offer the possibility to perform protein studies mentioned above directly in a laboratory. With the envisaged performances (10^{12}-10^{13} photons/s with an angular divergence of a few mrad and a bandwidth $\Delta E/E \sim 1$-10%), a compact machine could carry out researches to progress in the understanding of protein structural properties and could also provided an X-ray beam having the proper pulse length required for system dynamic studies in the picosecond range.

References

[1] Rapport parlementaire sur « Les techniques de restauration des œuvres d'art et la protection du patrimoine face aux attaques du vieillissement et des pollutions », par M. Christian KERT, Office parlementaire d'évaluation des choix scientifiques et technologiques, 15 juin 2006, rapport n°405.

[2] J. Salomon, J.C. Dran, T. Guillou, B. Moignard, L. Pichon, P. Walter, F. Mathis, "Present and future role of ion beam analysis in the study of cultural heritage materials: The example of the AGLAE facility", *Nuclear Instruments & Methods in Physics Research Section B-Beam Interactions with Materials and Atoms*, 266 (10), 2273-2278 (2008).

[3] M. Cotte, J. Susini, V. A. Solé, Y. Taniguchi, J. Chillida, E. Checroun, P. Walter, “Applications of synchrotron-based micro-imaging techniques to the chemical analysis of ancient paintings”, *Journal of Analytical Atomic Spectrometry*, 23, 820-828 (2008).

[4] J. Dik, K. Janssens, G. Van Der Snickt, L. van der Loeff, K. Rickers, and M. Cotte, ”Visualization of a Lost Painting by Vincent van Gogh Using Synchrotron Radiation Based X-ray Fluorescence Elemental Mapping”, *Analytical Chemistry* 80, 6436-6442 (2008).

[5] P. Tafforeau et al., “Applications of X-ray synchrotron microtomography for non-destructive 3D studies of paleontological specimens”, *Applied Physics* A 83, 195–202 (2006).

[6] Deorah S., Lynch, CF, Sibenaller ZA and Ryken, T. Trends in brain cancer incidence and survival in the United States: Surveillance, Epidemiology, and End Results Program, 1973 to 2001. C. *Neurosurg Focus 2006; 20 (4), E1.*

[7] Gérard JP. The Future of Hadrontherapy, ECPM-Nice 2 November 2006

[8] Biston M.C., Joubert A, Adam J.F., Elleaume H, Bohic S, Charvet AM, Estève F, Foray N, Balosso J. Cure of fisher rats bearing radioresistant F98 glioma treated with cis-Platinum and irradiated with monochromatic synchrotron X-Rays. *Cancer Research2004; 64, 2317–2323.*

[9] Rousseau J, Boudou C, Barth RC, Jacques Balosso J, Estève F and Elleaume H. Enhanced survival and cure of F98 glioma bearing rats following intracerebral delivery of carboplatin in combination with photon irradiation. *Clin Cancer Res 2007; 5195 13(17) September 1, 2007*

[10] Laissue J.A, Geiser G, Spanne PO, Dilmanian FA, Gebbers JO, Geiser M, Wu XY, Makar MS, Micca PL, Nawrocky MM, Joel DD and Slatkin DN. Neuropathology of ablation of rat gliosarcoma and contiguous brain tissues using a microplanar beam of synchrotron –wiggler generated X rays. *Int J Cancer 1998 78, 654–660.*

[11] Synergy of gene-mediated immunoprophylaxis and microbeam radiation therapy for advanced intracerebral rat 9L gliosarcomas. Smilowitz HM, Blattmann HE, Brauer-Krisch E, Bravin A, Di Michiel M, Gebbers JO, Hanson AL, Lyubimova N, Slatkin DN, Stepanek J and Laissue JA. *J. Neuro-Oncol. (2006) 78: 135–143*

[12] H.Elleaume & als: Performance of computed tomography for contrast agent concentration measurement with monochromatic x-ray beans: comparison of K-edge versus temporal subtractions. *Phys Med Biol 2002; 47: 3369-3385.*

[13] Alric C, Taleb J, Le Duc G, Mandon C, Billotey C, Le Meur-Herland A, Brochard T, Vocanson F, Janier M, Perriat P, Roux S, Tillement O. Gadolinium chelate coated gold nanoparticles as contrast agents for both X-ray computed tomography and magnetic resonance imaging. *J Am Chem Soc 2008 May 7;130(18):5908-15.*

[14] Balvay D, Troprès I, Billet R, Joubert A, Péoc’h M, Cuenod CA, Le Duc G. Mapping of tumor vascularisation and permeability in a rat glioma model by DCE Synchrotron radiation computed tomography. *Radiology 2009 Mar. 250(3):692-702*

[15] Keyriläinen J, Fernández M, Karjalainen-Lindsberg ML, Virkkunen P, Leidenius M, von Smitten K, Sipilä P, Fiedler S, Suhonen H, Suortti P, Bravin A. Towards high-contrast breast CT at low radiation dose. *Radiology 2008: 249 (1) 321-327*

[16] Pfeiffer F, David C, Bunk O, Donath T, Bech M, Le Duc G, Bravin A, Cloetens P. Region-of interest tomography for grating-based X-ray differential phase-contrast imaging. *Phys Rev Lett. 2008; 101 (16): 168101.*

[17] Risser L, Plouraboué F, Steyer A, Cloetens P, Le Duc G, Fonta C. From homogeneous to fractal normal and tumorous micro-vascular networks in the brain. *J Cereb Blood Flow Metab 2007 Feb;27(2):293-303.*

[18] A.A. Yee, NMR and X-ray Crystallography, Complementarity Tools in Structural Proteomics of Small Proteins, *J. Am. Chem. Soc.* 2005, 127, 16512-16517.

[19] P. Walian, Structural genomics of membrane proteins, *Genome Biology* 5, 215 (2004).

[20] S. Cusack et al., Small is beautiful: protein micro-crystallography, *Nature Structural Biology, Synchrotron supplement*, august 1998.

[21] D. Garriga et al., The 2.6-Angstrom Structure of Infectious Bursal Disease Virus-Derived T=1 Particle Reveals New Stabilizing Elements of the Virus Capsid, J. Virol. 80, 6895-6905 (2006).

[22] J.C. Phillips et al., Applications of Synchrotron Radiation to Protein Crystallography. II. Anomalous Scattering Absolute Intensity and Polarization, *Acta Cryst.* A33, 445-455 (1977).

[23] M. Wulff et al., The realization of sub-nanosecond pump and probe experiments at the ESRF, *Faraday Discussions* 122, 13-26 (2003).

[24] F. Schotte et al., Watching a Protein as it Functions with 150-ps Time-Resolved X-ray Crystallography, *Science* 300 1944-1947 (2003).

CHAPTER 2. Thomson and Compton scattering

2.1] Photon scattering

The diffusion of an electromagnetic plane wave by an electron at rest, with mass m_e and charge q, is a process known as 'Thomson scattering'. From a classical point of view, the process can be visualised as a plane wave of frequency ω_γ impinging on a charge. The scattered wave is not plane but, in the approximation where the recoil effect can be neglected (therefore taking into account $m_e >> \omega_\gamma$[1]), the electromagnetic wave frequency is conserved. On the other hand, in quantum electrodynamics, the scattering process is analyzed as the succession of the absorption and the emission of the photon by the electron.
The differential scattering cross section is [1]:

$$2.1) \qquad \frac{d\sigma}{d\Omega} = \frac{1}{2} r_0^2 (1 + \cos^2\theta) \; ;$$

where $r_0 \sim 2.818\ 10^{-15}$ [m] is the classical electron radius and θ is the photon scattering angle with respect to its initial momentum (see fig.1). By integrating over the angular variable, the classical Thomson cross section σ_{Th} is obtained:

$$2.2) \qquad \sigma_{Th} = \frac{8\pi}{3} r_0^2 = 0.665 \quad 10^{-28}\ [\mathrm{m}^2] \; ;$$

The absolute value of the Thomson cross section can be interpreted as follows: one photon travelling one meter within a target whose density is one electron per one cubic meter has a probability σ_{Th} of being scattered. Depending on the physics application, the scattering probability can be seen as large when compared to typical QED processes, or extremely low as it is the case, for example, in applications which aim at producing very high flux light sources.
The generalisation of equation (2.1), when the recoil of the charged particle cannot be neglected, was given by Klein and Nishina [2]. In this case the kinematics of the process is best described as a collision between the photon and the electron (see fig.1) since energy and momentum are conserved. Therefore the scattered photon undergoes a frequency shift. In the reference frame where the electron is initially at rest, the differential Compton cross section is (assuming unpolarised electrons and photons):

$$2.3) \qquad \frac{d\sigma}{d\Omega} = \frac{r_0^2}{2} \left(\frac{\omega_f}{\omega_i} \right)^2 \left(\frac{\omega_i}{\omega_f} + \frac{\omega_f}{\omega_i} - \sin^2\theta \right) \; ;$$

where ω_i (i=initial state) and ω_f (f=final state) indicate respectively the photon energy before and after the scattering process. It can be immediately pointed out that, in the limit $\omega_f / \omega_i \rightarrow 1$, i.e. in the case where the scattered photon frequency remains unchanged, (2.3) takes again the form of (2.1).

---

[1] In this chapter we will work in "God-given" units, where ∇ and c =1

2.2] High energy behaviour. Unpolarised and polarised Compton backscattering cross section

When considering the collision between a high energy free electron of momentum p_e and a low energy photon, where $p_e >> \omega_\gamma$, a substantial fraction of the electron energy is transferred to the photon. As a result, in the observer frame, the photon is backscattered with a significant energy boost. This process is known as Compton backscattering [3].

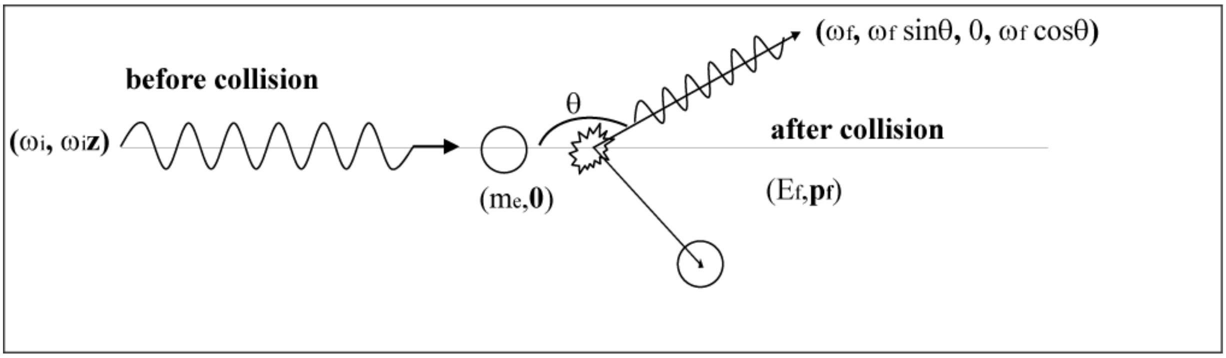

Figure 1: Two dimensional representation of the scattering kinematics, in the reference frame where the electron is initially at rest.

A simple expression of the total Compton scattering cross section in the centre-of-mass frame can be obtained by using the relativistic invariant Mandelstam variables [4]:

$$2.4) \qquad \sigma_{tot} = \frac{2\pi\, m_e^2\, r_0^2}{E_{cm}^2}\, Log\left[\frac{E_{cm}^2}{m_e^2}\right];$$

Where E_{cm} is the electron energy in the center-of-mass frame ($E_{cm} = m_e^2 + 2\, p_f\, \omega_f\, (1-\cos\theta)$).
Nevertheless, from an experimental point of view, the most important results are the differential and the total cross section in the laboratory frame. Neglecting for the moment the polarisation dependence, the total and differential scattering cross section are [5]:

$$a) \quad \sigma_{TOT} = \frac{2\pi\, r_0^2}{x_1}\left\{\left(1 - \frac{4}{x_1} - \frac{8}{x_1^2}\right)\ln\left(1 + x_1\right) + \frac{1}{2} + \frac{8}{x_1} - \frac{1}{2\left(1 + x_1\right)^2}\right\};$$

$$2.5) \; b) \quad \frac{d\sigma}{d\Omega} = 2 r_0^2 \left(\frac{\omega_f}{m_e\, x_1}\right)^2 \left(4y\left(1 + y\right) - \frac{x_1}{x_2} - \frac{x_2}{x_1}\right)$$

$$where \quad x_1 = 2\gamma \frac{\omega_i}{m_e}\left(1 - \beta\cos\varphi_1\right); \quad x_2 = -2\gamma\frac{\omega_f}{m_e}\left(1 - \beta\cos\varphi_2\right); \quad \mathrm{y} = \frac{1}{x_1} + \frac{1}{x_2}$$

Where β is the relativistic beta factor and φ_1 and φ_2 indicate respectively the incidence angle and the scattering angle in respect to the electron direction, as illustrated in fig.3. If $x_1 << 1$ ($\gamma\, \omega_i << m_e$) the second term of the formula (2.5 a) can be replaced with an excellent

approximation by σ_{Th} (1-x_1) ~ σ_{Th}. Then the total scattering cross section is very close to the Thomson one. Therefore, in this approximation, it is possible to evaluate the emitted rate as the product of the Thomson cross section with the Luminosity (see § 2.4).
The spectral density in the ultrarelativistic case is simply obtained starting from (2.5 b) and taking into account the relationship

2.6) $$\frac{d\sigma}{d\omega_f} = \frac{\pi\, m_e\, x_1}{\gamma\, \omega_f^2} \frac{d\sigma}{d\Omega}.$$

The photon and the electron polarisations can be neglected when the electron energy is relatively low (up to a few GeV), but this is not true anymore for ultrarelativistic electron beams. In fact the most general form of the differential cross section that takes into account the initial polarisation states[2] is [6]:

2.7)

$$\frac{d\sigma}{d\Omega} = \frac{r_0^2}{2}\left(\frac{k_f}{k_i}\right)^2 \left(\Sigma_0 + S_1(0)\Sigma_1 + S_3(P_y\Sigma_{2y} + \Sigma_{2z}P_{2z})\right)$$

where

$$\left\{\begin{array}{l}
1)\ \text{(a)}\ k_i = \dfrac{2\gamma\,\omega_i}{m_e};\ \text{(b)}\ k_f = \dfrac{1}{\left(1 - \cos\theta + k_i^{-1}\right)};\ \text{(c)}\ \cos\theta = \dfrac{E_e - \omega_f(1 - k_i^{-1})}{E_e - \omega_f}; \\[2ex]
2)\ S_1(0) = \text{second component of the Stokes vector at } \phi = 0;\ S_3 = \text{fourth component of the Stokes vector;} \\[2ex]
3)\ P_z; P_y = \text{respectively the longitudinal and transverse components of the electron polarisation;} \\[2ex]
4)\ \Sigma_0 = \left[(1 + \cos^2\theta) + (k_i - k_f)(1 - \cos\theta)\right];\ \Sigma_1 = \cos 2\phi \sin^2\theta; \\[2ex]
\quad \Sigma_{2y} = k_f \sin\phi \sin\theta(1 - \cos\theta);\ \Sigma_{2z} = (1 - \cos\theta)(k_i + k_f\cos\theta);
\end{array}\right.$$

Since in the scattering process the electric field vectors are taking as reference the scattering plane (defined by the k_i and k_f vectors) the Stokes vector components S_1 and S_2 are functions of the azimuthal angle ϕ. It is easy to check that the Klein-Nishina formula is obtained when P and S = 0 in (2.7). From (2.7, 1c) the differential spectrum $d\Omega/d\omega_f$ can be expressed as a function of the scattered photon frequency and the polarisation vectors; **P** = (P_x,P_y,P_z) for the electron and the four dimensional Stokes vector [7] **S**=(S_0,S_1,S_2,S_3) for the photon. In this case it is possible to highlight the differential cross section dependence on the electron beam energy, its longitudinal polarisation and the photon circular polarisation (given by the component S_3) since, after integration over the azimuthal angle between 0 and 2π, the contribution of plane polarizations (S_1 or S_2 components) is cancelled out.

---

[2] Polarisation effects should be important in some applications of phase contrast medical imaging.

A circular polarization of the light wave has a strong impact on the backscattered photon energy spectrum when increasing the electron energy, as shown in fig.2 (a,b,c,d). In these plots the normalised differential cross section is illustrated for three different cases (P_zS_3 = 1,0,-1) and for four different electron energies, starting from 50 MeV and going up to 60 GeV. Since the cross section at the energy cut-off depends on the polarization, the normalisation has been done for $\omega_f = 0$.

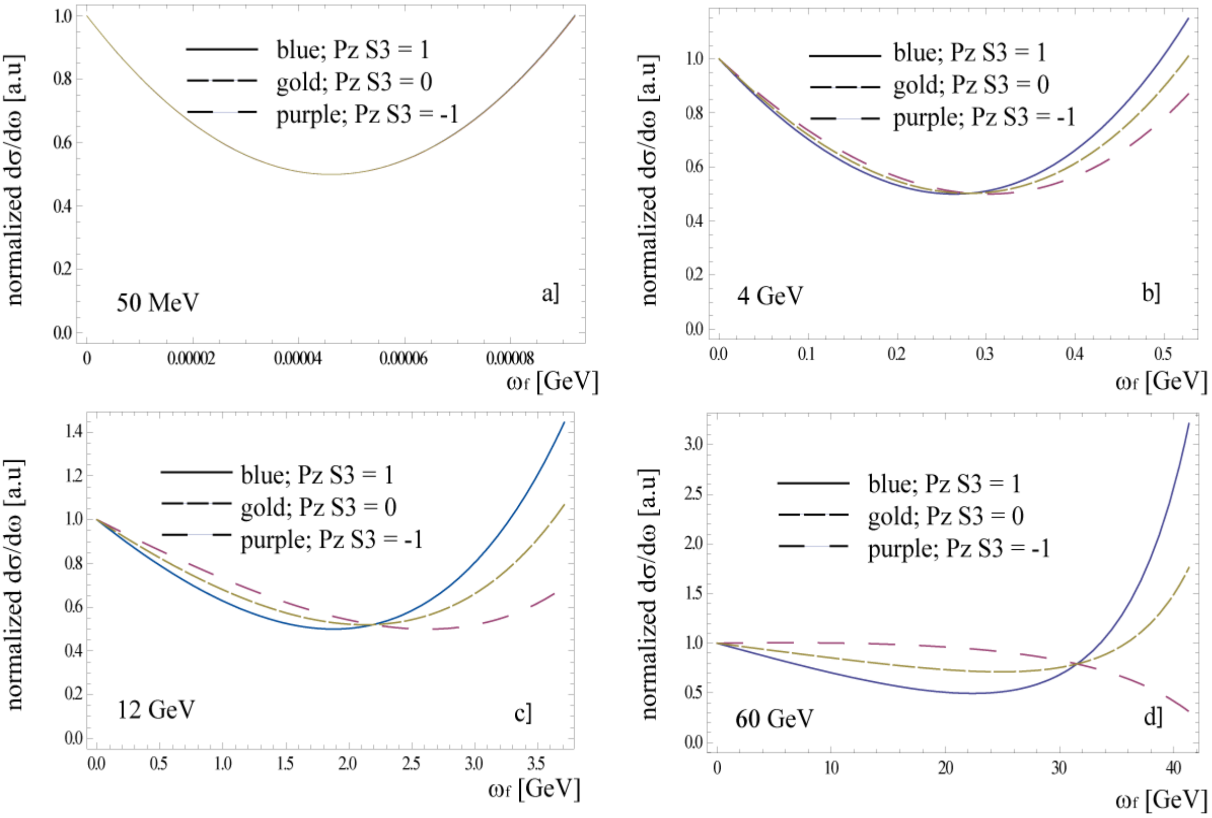

Figure 2 : Differential cross section $d\sigma/d\omega_f$ for different electron energies, respectively 0.05, 4, 12, 60 GeV. The assumed initial photon energy is 2.4 eV. Calculations worked out with MATHEMATICA®.

The differences in the spectrum of the back-scattered photons are negligible in the 50 MeV case. At 4 GeV, circular polarization introduces a ~10% variation in the differential cross section at the energy cut off. At very high energy (see for example the 60 GeV case) the asymmetry for the +1 and the -1 case becomes very large. This strong asymmetry can be used for the polarization measurement of ultrarelativistic particles. Fig.2 also shows that the emitted spectrum has a sharp cut-off as far as the backscattered photon energy is concerned. This energy cut off is proportional to the energy of the impinging photon and varies quadratically with the electron energy. The frequency boost due to the Compton backscattering and the relationship between the scattered photon emission angles and its energy will be discussed in the next paragraph.

2.3] The frequency shift and the emission angular distribution

As previously stated, when the recoil cannot be neglected, the scattered photon undergoes a frequency shift. The scattered photon frequency shift $\Delta\omega = \omega_f - \omega_i$ is given by [5]:

2.8) $$\omega_f = \frac{\omega_i}{1 + \frac{\omega_i}{m_e}(1 - \cos\theta)} \; ;$$

where one notices that for $m_e >> \omega_i$ the frequency is conserved after the collision as was previously mentioned.
The specific case of a Compton collision between a free relativistic electron ($p >> m_e$) and a photon shows very interesting characteristics in the laboratory frame. They originate in the joint effect of the relativistic boost and the Doppler effect. Actually the observer will notice a significant energy boost of the scattered photon and a drastic shrinking of the angular cone of emission. These can also be calculated by using the Mandelstam variables, taking into account the most general collision geometry case of a photon with incidence angle φ_1 (see fig.3) [5]. In the laboratory frame the "boosted" frequency shift is:

2.9) $$\omega_f = \frac{\omega_i(1 - \cos\varphi_1)}{1 - \beta\cos\varphi_2 + \frac{\omega_i}{m_e\gamma}(1 - \cos\theta)} \quad \text{that for} \quad \gamma >> 1 \quad \approx > \frac{2\gamma^2\omega_i(1 - \cos\varphi_1)}{1 + (\gamma\varphi_2)^2 + 2\gamma\frac{\omega_i}{m_e}(1 - \cos\varphi_1)}$$

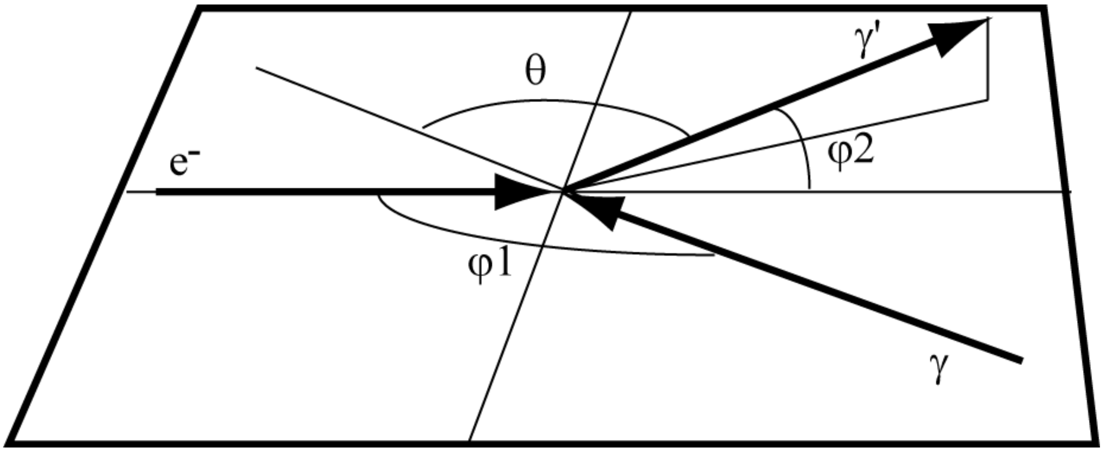

Figure 3 : Scheme of the most general case of a photon-electron collision. The electron incidence angle is φ_1, the photon scattering angle is θ (with respect its initial momentum).

From (2.9) it is possible to highlight the dependence of the main properties of the scattered photon on the collision parameters: the photon incidence energy and angle, the electron energy and the photon scattering angle. The Compton back-scattering characteristics are particularly attractive in the relativistic case where they can be summarised as follows:

a) There is a univocal dependence between the scattered photon energy and its angle. This is very effective for selecting the frequencies, and consequently to obtain a monochromatic beam, by setting up a simple diaphragm.
b) The emission cone is shrunk by the relativistic boost. To a good approximation one can assume that the flux is emitted in a solid angle with total aperture $4/\gamma$ (see fig. 4 and 6).
c) The maximum energy boost of the scattered photon occurs in the so-called "head-on" collision ($\varphi_1 = \pi$). In this case the energy spectrum cut off ω_c, corresponding to the

backscattered photon ($\varphi_2=0$), varies as $\omega_c=4\omega_i\gamma^2$. For different collision angles the maximum energy is reduced. If $\varphi_1=\pi/2$ the scattered photon maximum energy is half the one in the head-on collision case (see fig.5), while the mean direction of the backscattered photons remains close to the electron beam direction.

d) The high value of the scattered photon maximum energy (the energy cut-off) with its quadratic dependence on the electron energy allows the production of high energy X rays and gammas by using moderate energy electron beam, in the MeV-GeV range.

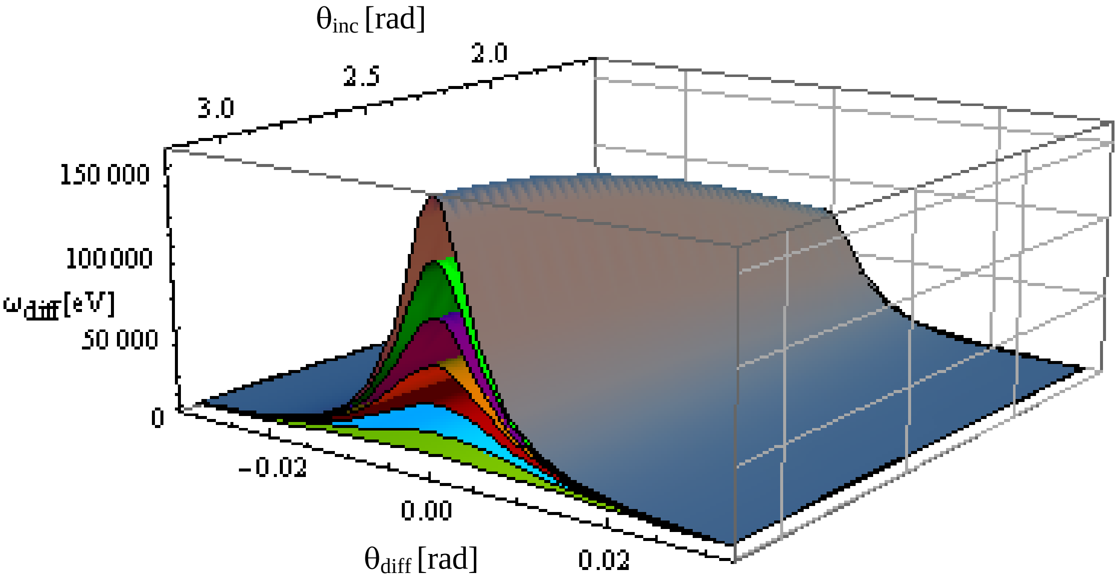

Figure 4 : Scattered photon angle-energy dependence (ω_{diff} vs θ_{diff}) for different collision angles θ_{inc}. This is varied from the head-on collision ($\theta_{inc} = \pi$) to the normal incidence ($\theta_{inc} = \pi/2$). The colour curves represents different electron energies; respectively 100 (brown), 70 (light green), 60 (violet), 50 (orange), 40 (red), 30 (light blue) and 20 MeV (green). The initial photon energy is 1 eV. Calculations worked out with MATHEMATICA®.

In fig.4 the three dimensional plot summarises the dependence of the scattered photon energy on the incidence and scattered angles for different impinging electron energies. One notices that orthogonal collision halves the scattered frequency and that the emitted photon cone shrinks as the energy increases. The different colour curves correspond to different electron energies. To better appreciate the different parametric dependences, fig.5 (a,b) shows the energy angular dependence for an impinging electron of 50 MeV and three different photon wavelengths corresponding to three typical lasers (CO_2, fibre and YAG with a frequency doubler cavity).

The factor two in the emitted photon energy is visible by comparing fig.5a and 5b where the head-on and the orthogonal incidences are respectively illustrated. For the same typical wavelength fig.5c and 5d illustrate the spectrum energy cut-off for different values of the γ relativistic factor of the incident electron. The two figures always take into account the two extreme cases for the collision angles $\varphi_1= \pi$ and $\varphi_1 = \pi/2$.

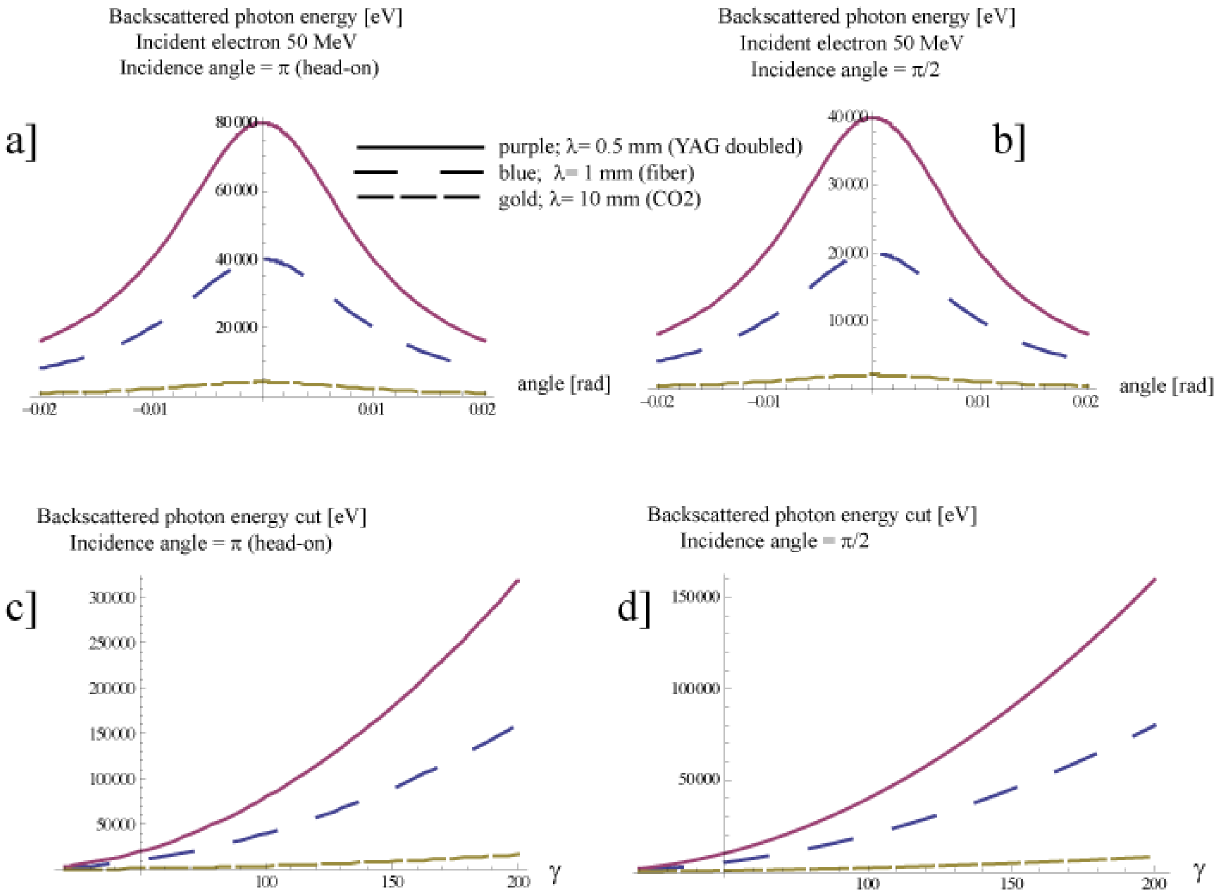

Figure 5 : a] and b] panels: scattering energy dependence for head-on and orthogonal collision. c] and d] panels: energy cut-off dependence on the electron initial energy. Calculations worked out with MATHEMATICA®.

To better appreciate the angular shrink given by the relativistic boost, fig.6 illustrates the normalised results of fig.5a, in the case of head-on incidence and a fibre laser, for three different values of γ. It shows how, at relativistic energies, the emission cone is extremely narrow, thus allowing a photon beam brilliance increase.

The limit of the angular shrinking is given, in a real experiment, by the fact that the Compton flux is not generated by a single particle but rather by an electron beam with a natural divergence at the interaction point. The resulting angular aperture of the emitted photons will then be given by the convolution between the Compton $1/\gamma$ cone and the electron beam divergence. This is extremely important since, taking into account the angle-energy dependence for the scattered photons, a too strongly divergent electron beam will affect not only the brilliance, but also the possibility to select a monochromatic beam by using diaphragms.

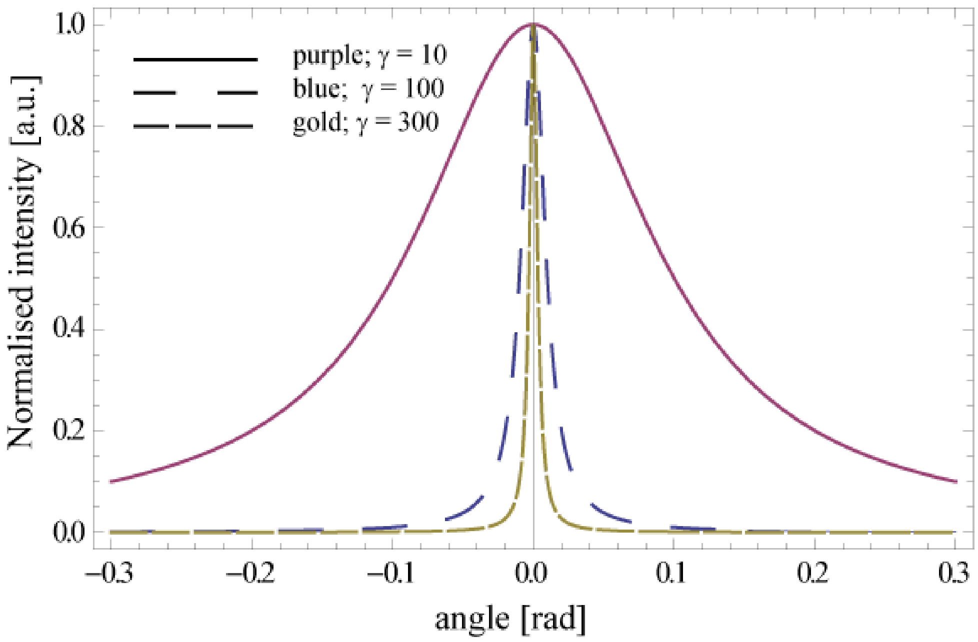

Figure 6 : Angular distribution of the backscattered photons for three different electron energies. Calculations worked out with MATHEMATICA®.

2.4] Parameterization of RadioThomX source.

After the introduction on the Compton scattering physical properties, it is possible to better characterize its application to the X-ray production by the collision of relatively low energy electron bunches with laser pulses. For this purpose, some standard parameters distinguishing the performances of the ThomX machine design are taken into account and the parametric dependence of the produced X-ray flux is studied.

All the calculations presented in this chapter have been worked out assuming the following nominal parameters for the laser and the electron beam (if not specifically mentioned):

Laser pulse length = 1 ps r.m.s.
Laser wavelength = 1030 nm
Laser beam focus size = 43 µm r.m.s.
Laser pulse energy = 30 mJ
Electron bunch length = 20 ps r.m.s.
Electron energy = 50 MeV
Electron energy spread = 0.6 % r.m.s.
Electron beam waist sizes = 70 µm r.m.s.
Electron bunch charge = 1 nC
Non normalized electron beam emittance = $5\ 10^{-8}\ \pi$ m rad

These assumptions are made to set some typical values for our general parametric analysis. They are representative of a single Compton collision hence they do not take into account the beam dynamics. An in-house Monte Carlo code has been used to include the different collision configurations. The main results have been validated by the comparison with the general analytical formula for the Compton collision luminosity of two Gaussian bunches crossing [8], where Gaussian distributions are assumed and the hourglass effect is neglected (assuming constant beams sizes during the collision, so without taking into account the cross effect of the laser Rayleigh length, the IP beta function and their correlation with the bunches lengths):

2.10) $$L = N_e N_\gamma \, f \, \frac{\cos\phi}{2\pi} \frac{1}{\sqrt{\sigma_{ye}^2 + \sigma_{y\gamma}^2}\sqrt{\left(\sigma_{x\gamma}^2 + \sigma_{xe}^2\right)\cos^2\phi + \left(\sigma_{ze}^2 + \sigma_{z\gamma}^2\right)\sin^2\phi}}$$

where N_e, N_γ, f, ϕ, $\sigma_{x,y,z,e}$, $\sigma_{,x,y,z,\gamma}$ indicate respectively the number of electron and photons per bunch, the repetition frequency, the half of the angle of collision and the three dimensional bunches r.m.s. sizes for the electron (index e) and photon (index γ) bunches. Once the Luminosity (L) is given the produced photon rate (R) is defined as:

2.11) $R=\sigma_{\text{Compton}}$ L.

In the Monte Carlo simulations the repetition frequency was assumed unitary since it correspond to a single interaction between one electron bunch and one laser pulse. In the dynamical regime the scattered flux, after many passages, will be reduced as a consequence of the electron beam quality deterioration, given by the recoil during the collisions. This aspect will be treated in § 4.5.9.

With respect to the previous paragraphs where an electron-photon collision was considered, the flux emitted in a real laser pulse - electron bunch collision has some important consequences. It is important to remember that in a single electron-photon scattering event the emission properties are mainly dominated by the electron kinematics. So, well defined relationship between the scattered photons angles and their energies is established. Now, dealing with real bunches the results will be a convolution between the emission probability curves and the electron beam divergence in the interaction point. This will imply that:

1) The number of scattered photons per unit angle depends on the emittance of the electron beam and on the storage ring beta function in the Interaction Point (IP)

2) The brightness and the energy angular dependence, so the possibility to obtain a monochromatic beam with a simple diaphragm system (that hereafter will be called as "angular monochromaticity"), are submitted to the same convolution dependence.

3) Strong laser and electron beam focusing in the interaction point does not correspond to a quadratic increase of the flux due to the Hourglass effect given by the laser beam Rayleigh length, the storage ring beta function, the electron bunch and the laser pulse r.m.s. lengths in the interaction region.

This will be illustrated in the following paragraphs.

2.4.1] Flux dependence on the beams waists sizes.

One of the main parameter that determines the efficiency of the X-ray production is the beams interaction point (IP) sizes i.e., the interacting beams waist sizes in the interaction region. Formula 2.10 shows that a decrease in IP sizes leads to an increase in scattered flux. The dependence is inversely proportional to the square of the interacting beams sizes. Nevertheless one can notice that, while the laser beam waist has an influence only on the scattered flux, for constant emittance the electron beam sizes affect at the same time the flux, the directionality and the monochromaticity of the scattered radiation.

Fig.7 illustrates the dependence of the flux of the scattered radiation (total and per unit angle) on the electron and laser beams waist sizes.

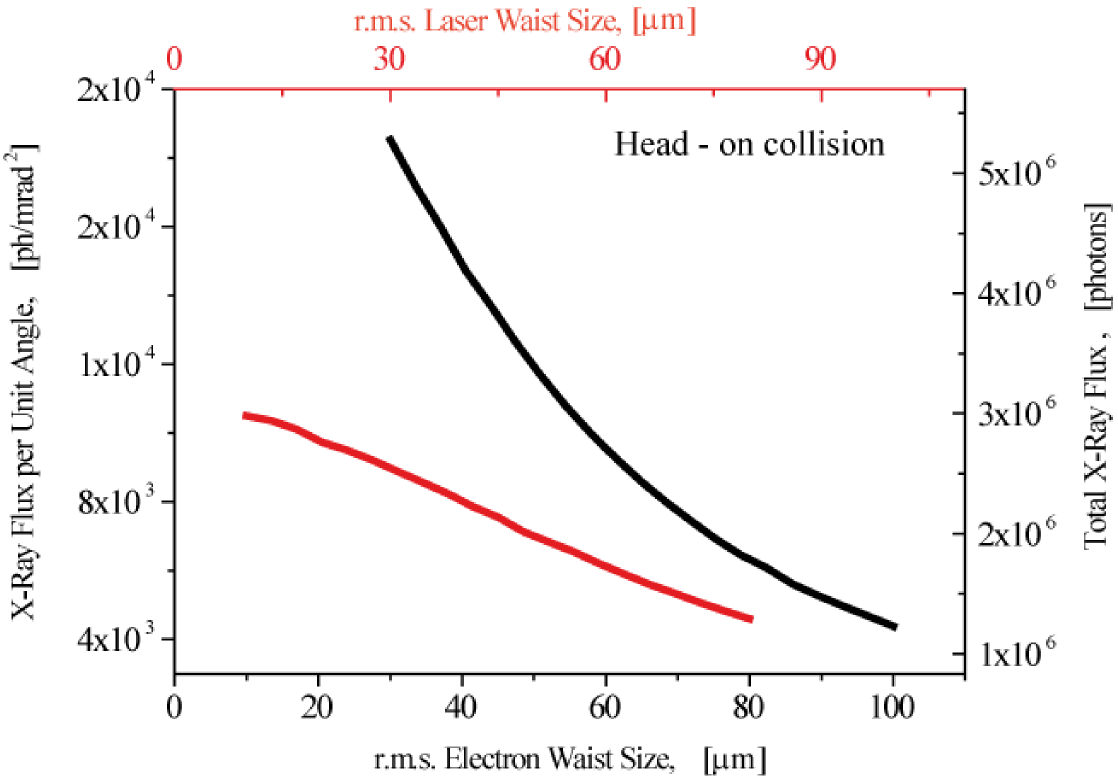

Figure 7 : X-Ray flux versus the r.m.s. beams waists sizes. Both the flux per unit angle per collision (left vertical axis) and the total emitted flux per collision (right vertical axis) are displayed. The red curve panels the variation of the laser beam waist size while the electron one remains constant (70μm). The black curve corresponds to a variation of the electron beam waist size while the laser remains constant and equal to 43μm. The head-on collision case is assumed

The weak, almost linear dependence of the flux with the laser beam waist size is explained by the Hourglass effect as a function of the Rayleigh length. The variation of the laser beam focus size from 70 to 10 μm increases the scattered flux just by two times. From this it follows that the nominal designed value of 43 μm should be considered within optimal limits. Variation of the electron beam waist sizes does not bring the expected behaviour of the scattering efficiency. It is also far from the expected quadratic one (a size reduction of a factor two corresponds to a doubling of the emitted flux) and the curve second derivative decreasing in the region of smaller electron beam sizes is noticeable. Taking into account a fixed beta function at the interaction point of 0.1 m, the electron beam size range form 30 to 100 μm corresponds to a geometrical emittance variation from 8.8 10^{-7} to 9.8 10^{-6} π mm mrad.

2.4.2] Flux dependence from the collision angle.

As illustrated in formula 2.10 another important parameter is the angle of collision assumed as the angle between the laser and the electron beams propagation axis. A luminosity reduction is expected when the lengths of interacting pulses are much longer than their transverse sizes. Moreover, the presence of a non-zero collision angle imposes rigid limits on possible time jitter between laser pulse and electron bunch. Namely, when the time jitter is of the order of the laser pulse and/or the electron bunch duration, they cross without spatial intersection.
The flux collision angle dependence versus different parameters is hereafter presented. The dependence of the number of scattered photons on the collision angle is illustrated in fig.8.

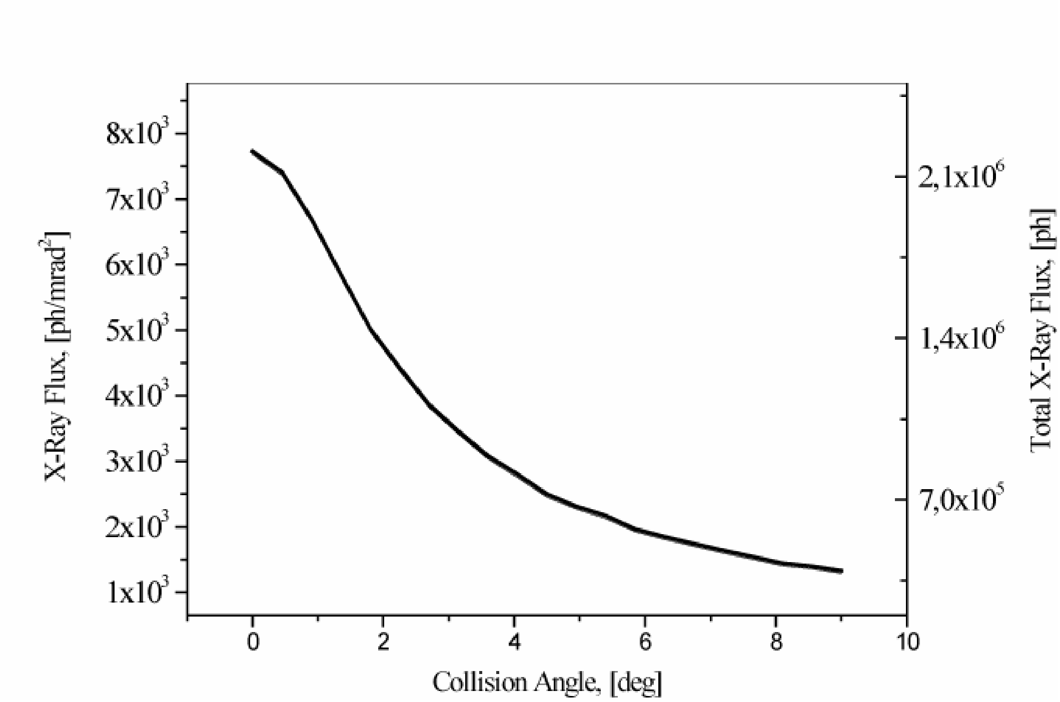

Figure 8 : X-Ray flux per unit angle per collision dependence on the angle of interaction between the laser and the electron beams.

In crossed collision, as illustrated in formula 2.10, the luminosity is determined not only by the collision angle but it is also correlated with the beam length. Since in the Compton sources the longitudinal beam dynamics is dominated by the recoil during scattering process, a consequent bunch lengthening is expected. Therefore in fig.9a a comparison of the head-on and the 2 degrees collision configurations is shown. The scattered X-Ray flux per unit angle dependence versus the electron bunch length is illustrated. The 3D surface plot (fig.9b) summarizes this dependence for different collision angles.

For the nominal parameters of the laser and of the electron pulses this dependence is rather weak. For example, the beams interacting in head-on collision configuration scatter just 1.5 times higher X-ray flux than the beams interacting with a collision angle of 2 degrees. Taking into account a nominal bunch length of 20 ps, its compression to 10 ps increases the scattered flux by less than a factor two, while stretching the bunch up to 50 ps leads to two-fold reduction in flux. Basically the scattering efficiency is rather sensitive to the electron bunch lengthening only for larger angles of collision. In fact, for the same beam parameters, a flux reduction factor of about six times is expected for eight degrees crossing angle.

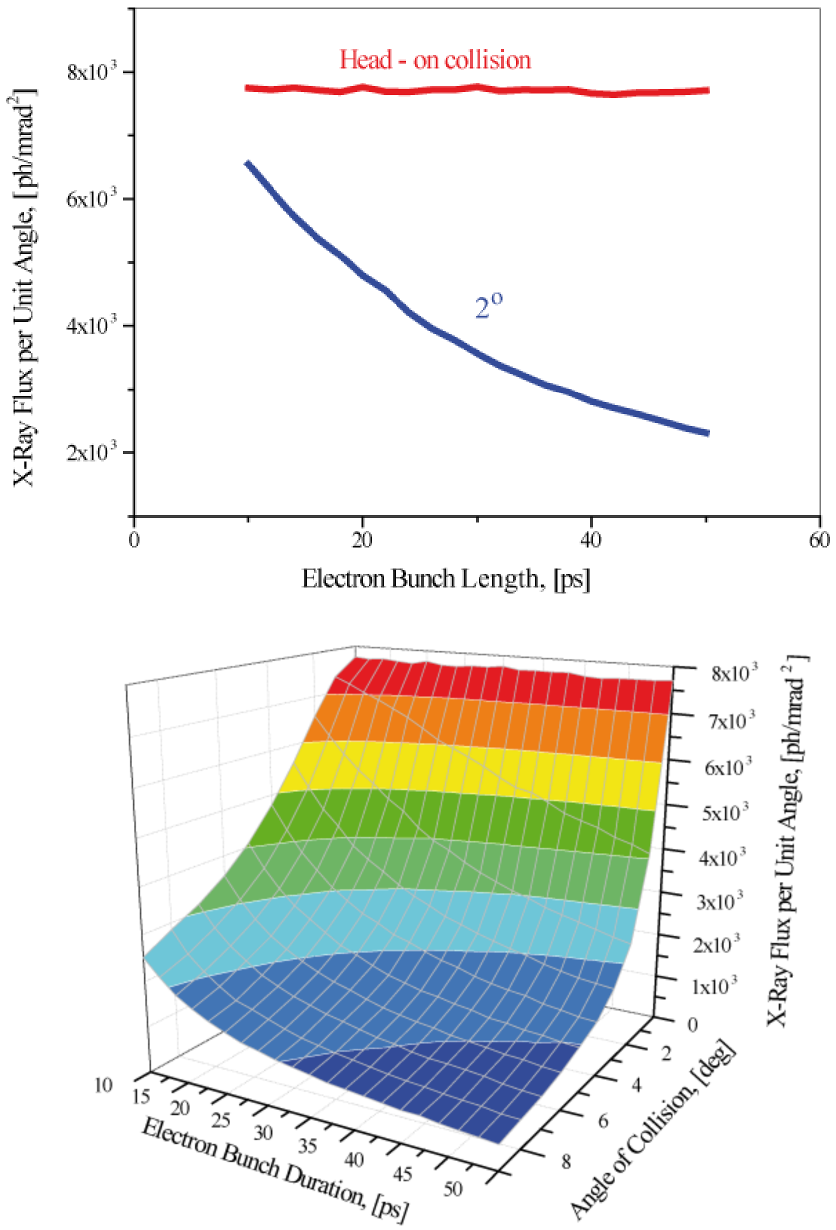

Figure 9 a,b : (a) X-Ray flux per unit angle per collision dependence on r.m.s. electron bunch length. This is calculated for 2 degrees angle of collision (blue line) and for the head-on (red line) configurations. (b): X-Ray flux of the ThomX source versus angle of collision and electron bunch length.

When crossed collisions are taken into account, the possible time mismatching plays a crucial role in scattering efficiency. Fig.10a displays the X-Ray flux per unit angle dependence on the cumulative time delay between the electron bunch and the laser pulse, for different collision angles. A zoom on the head-on (red curve) and 2 degrees (blue curve) cases is illustrated in fig.10b.

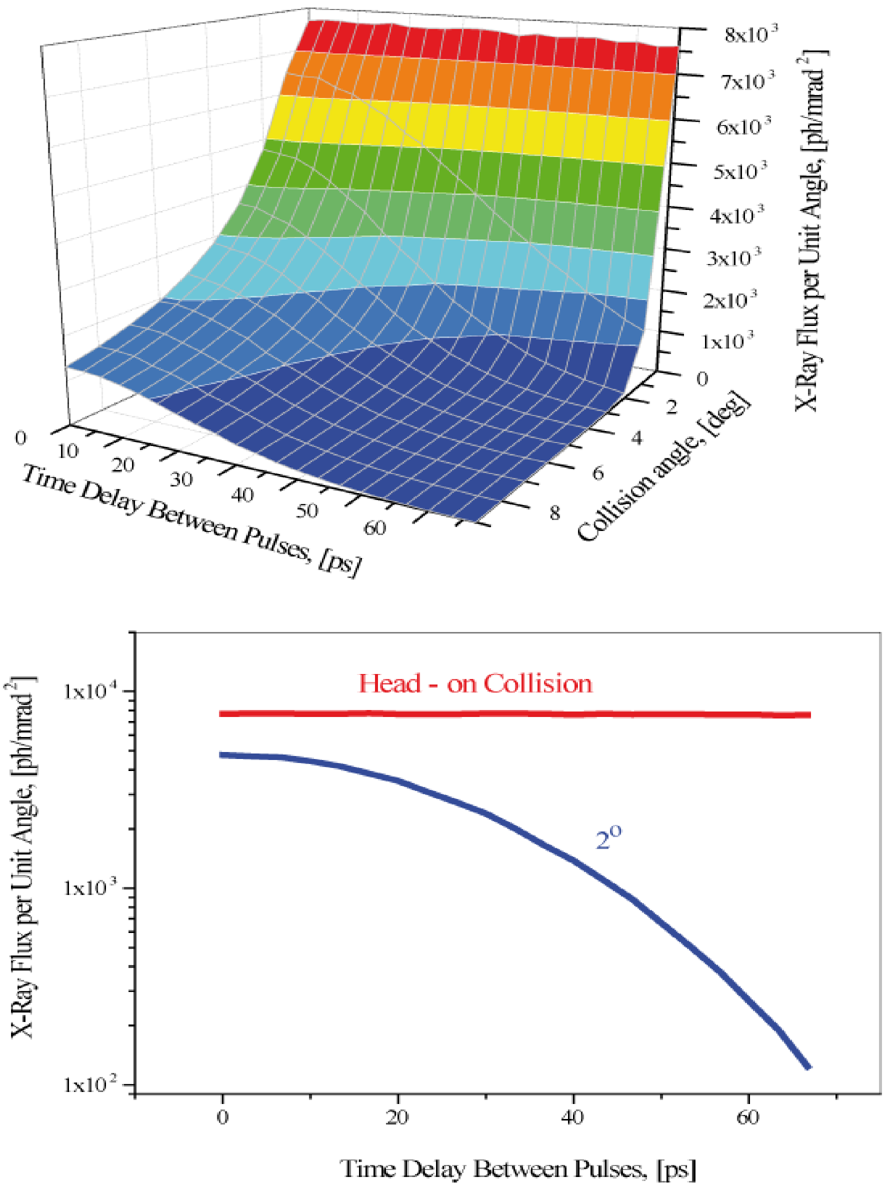

Figure 10 a,b : The surface plot presents the X-Ray flux per collision calculated for various values of time jitter between pulses and collision angle. Fig 10 b shows the X-Ray flux dependence on the electron bunch time jitter with respect to laser pulse calculated for 2 degree collision angle (blue curve) and the head-on collision (red curve).

The scattered flux per unit angle drops drastically with the increase in collision angle when the electron bunch and the laser pulse interact with non-zero time delay.

2.4.3] Brightness and monochromaticity.

As previously mentioned, when dealing with a collision between laser pulses and electron bunches that occupy a well defined phase space, the scattered photon beam directivity and spectrum are dominated by the electron bunch characteristics in the IP.
This convolution effect is highlighted in fig.11 where the flux per unit angle and the brightness of the scattered photon beam as functions of the IP electron beam waist size are illustrated. Here the electron beam emittance is assumed to be constant and equal to its nominal value. Without considering the spectral angular distribution the flux increases for smaller beam sizes, but when the brightness (and so also the emission bandwidth) is taken

into account it is possible to notice that a maximum is reached near ~ 50 µm. The following decreasing of the brightness is the results of the prevalence of the effect of the scattered photons directionality deterioration due to the high divergence of the electron beam in the collision point.

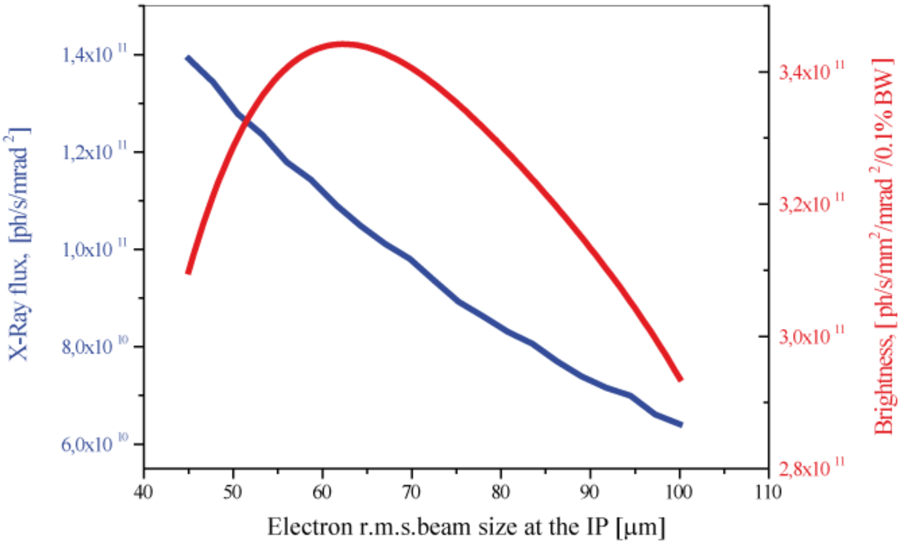

Figure 11 : Dependence of on-axis X-Ray flux (blue curve) and brightness (red curve) on the r.m.s. electron beam waist size. The assumed collision angle is 2 degrees and the collision repetition frequency is 20MHz.

The same effect can be visualized considering the on axis spectrum for an emission cone of one mrad^2, calculated for various electron waists (see fig.12).

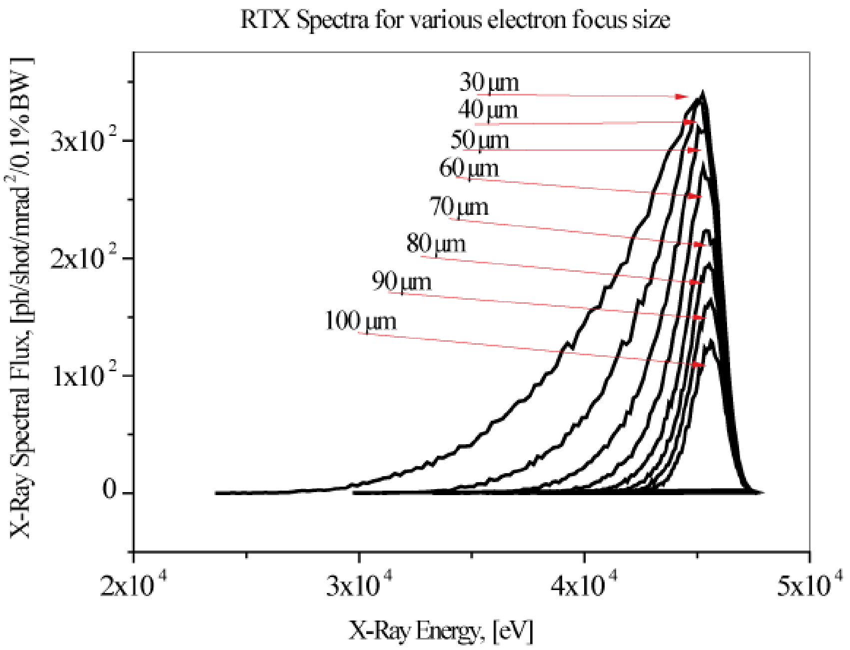

Figure 12 : On-axis spectra calculated for various electron waists sizes and head-on collision. Electron energy is equal to 50 MeV.

2.4.4] Flux dependence from the electron beam energy.

Because of the quasi-absence of synchrotron cooling in the Compton ring due to the low energy, reduction of the non-normalized emittance is possible by adiabatic damping in the Linac. Moreover the scattered photons show the characteristic 1/γ cone angular dependence. So increasing the machine energy is profitable also for the photon flux characteristics.

On the other side the cross section of Thomson scattering depends very weakly on the energy of scattering electrons. The flux and the brightness dependence on the energy and the beams waist sizes are illustrated in fig 13 a,b.

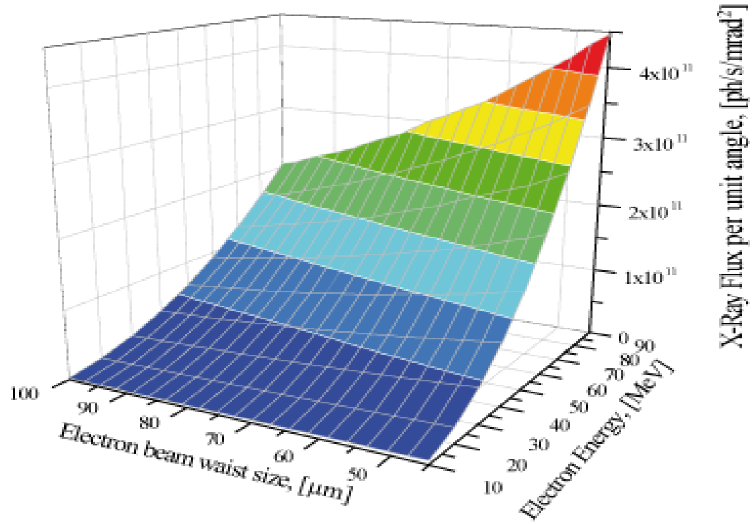

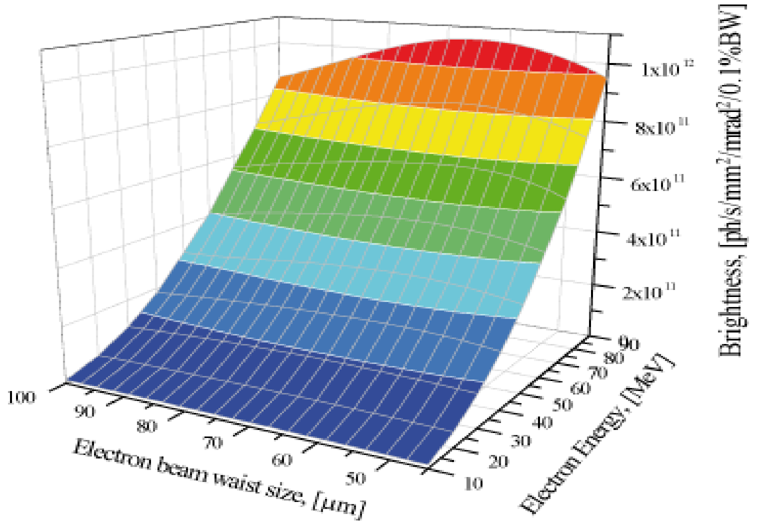

Figure 13 : X-Ray flux (a) and brightness (b) of RTX source versus electron focus size for various electron energies. The assumed collision angle is 2 degrees and the repetition frequency is 20 MHz.

The brightness of the source is optimized when the electron beam waist size is near 60 μm, very close to the designed value of 70 μm. The difference is only about 15 %.

The X-ray spectra in a cone of 1 mrad^2, calculated for series of electron energies from 10 up to 90 MeV are shown in fig.14.

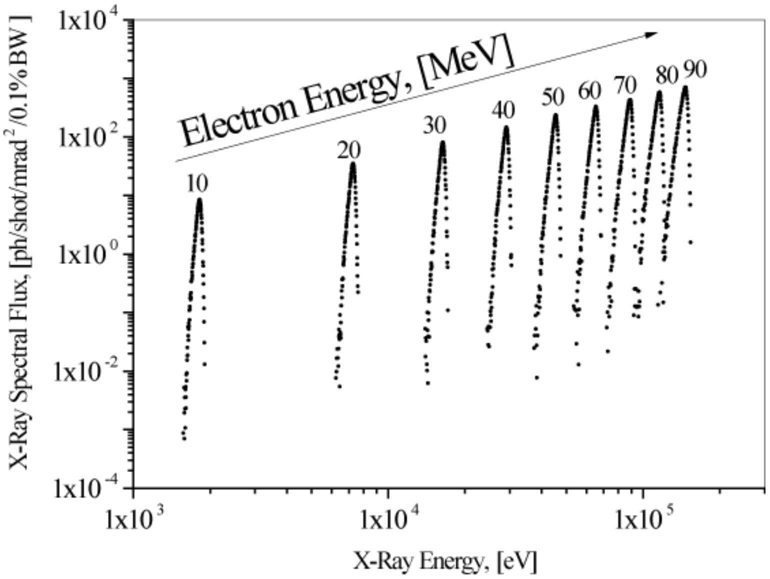

Figure 14 : Left: On-axis RTX spectra calculated into 1 mrad^2 for various electron energies.

The spectrum shape of the scattered radiation does not depend on the electron energy. The flux per unit angle increases linearly with the electron energy.

References

[1] A.H Compton, Phys.Rev 21 (1923) 715
[2] J.D.Jackson; Classical Electrodynamics, *Third Edition, 1999. John Wiley and Sons*
[3] O.Klein; Y.Nishina *Z. f. Phys. 52: 853 and 869; (1929).*
[4] M.E.Peskin; D.V.Schroeder; An Introduction to Quantum Field theory, *1995. The Advanced Book Program*
[5] P. Rullhusen; X.Artru; P.Dhez; Novel Radiation Sources Using Relativistic Electrons; *Series on Synchrotron Radiation Techniques and applications – Vol.4; World Scientific.*
[6] D.P.Barber et al ; *Nuclear Instruments and Methods in Physics Research A329 (1993) 79-111*
[7] M.Born and E.Wolf, Principle of optics (Pergamon Press, 1959)
[8] T.Suzuki, “General formulae of luminosity for various types of colliding beam machines” KEK 76-3 July 1976

CHAPTER 3: Optical Systems

3.1] Laser and Fabry Perot resonator

3.1.2] Introduction

The optical part of this project is in itself a very ambitious and far-reaching project. Indeed, in order to achieve the X-ray photon fluencies required for the applications described in the introduction, the weak Thomson cross section makes it necessary to use very high photon fluxes. With current day technologies, it is in fact possible to produce picoseconds pulses with tens of Joules of pulse energy. However, the thermal load in the amplification media limits severely the average output power to few tens of Watts. As a consequence, in such a system, repetition rates are limited to few Hz and clearly incompatible with the repetition rates of electron storage rings. In order to significantly improve the repetition rate of the laser, while keeping important pulse energies, we propose to develop an optical system based on a high finesse Fabry-Perot (FP) cavity injected by a high average power laser system. The pulses coming from the laser are stacked in the Fabry-Perot cavity achieving a passive gain in the cavity ranging from 1000 to 10000. Such an approach is very attractive since it requires a laser system delivering a limited (although important) average power of the order 100 W. The signal is then boosted to the MW level within the passive cavity. The technical price to pay is the high level of sophistication of all stages of the system. The optical system therefore consists in a high stability laser oscillator, a high average power amplifier, an optional frequency converter, a high finesse FP cavity and finally the feedback loop locking both cavities. Fig.1 presents a general layout of the global optical system.

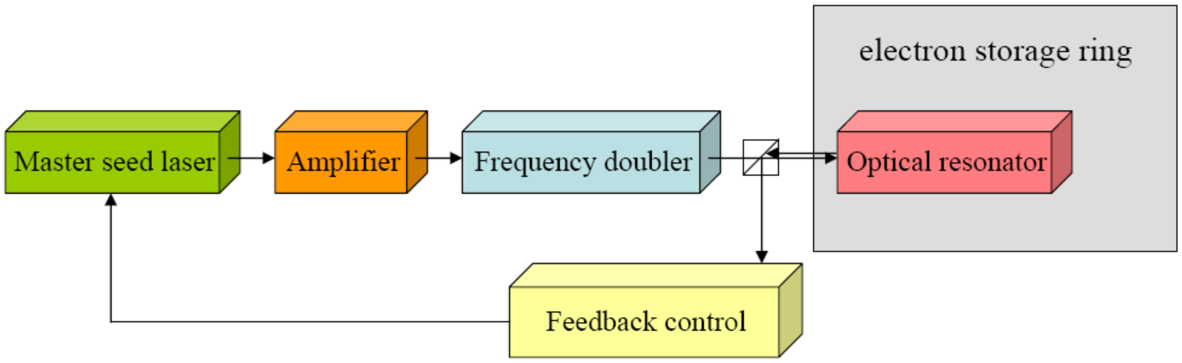

Figure 1: Block diagram of the general optical setup.

We now describe all elements of this optical system: the high power optical seed laser, a frequency conversion unit, the Fabry-Perot cavity, the locking procedure and the mechanical implementation within the electron storage ring.

3.1.2] Laser

In this project, the initial laser system must meet severe requirements. The demands of the final applications in terms of high X ray fluxes set indeed a minimum output power around 100 W. In order to significantly enhance the field power, the beam should then be injected into a very high finesse cavity. This later constraint imposes a vary high degree of quality to a number of laser beam parameters;

- beam spatial profile, single mode as close as possible to TEM_{00}
- degree of polarization, close to 100%
- Pointing stability
- Pulse to pulse stability. More precisely, the noise spectrum and in particular the phase noise of the laser should be extremely low, to allow for efficient mode-locking in the Fabry-Perot cavity.

In addition, the laser system together with the cavity must to be installed in the electron beam pipe, and thus require as much as possible compactness, stability and heat control.

The following table recapitulates the main target parameters for the pulsed seed laser system, to be injected in the Fabry-Perot resonator:

Wavelength	Pulse duration	Repetition rate	Average power
1 μm	few ps	41.4 MHz	100 W

Table 1: Target parameters for the pulsed laser system.

At first sight, reaching such parameters with conventional laser technology is not a major challenge in itself, starting from a low power oscillator, followed by successive bulk amplification stages. However, it is extremely unlikely that the output beam would then display the qualities demanded by the application. In fact, extracting few tens of Watts of short pulses in bulk material already requires a high capacity cryogenic cooling to limit spatial beam distortion by efficient heat removal. Although developing a system of few hundreds of Watts based on this latter technology may look feasible, it would provide a very complex setup and the beam quality and stability may not be guaranteed. New laser techniques are therefore stringently required.

Two main paths are currently being investigated at CELIA and at LAL to reach the required performances.

- The first possible approach is based on a high power laser oscillator, followed by a low gain amplifying stage. Recent results have indeed demonstrated laser powers of several tens of W, with pulses in the few picoseconds range, very close to the target specifications [1]. The average power of such oscillators is so high that a limited amplification in bulk would be sufficient to reach the 100 W objectives, while keeping the high spatial quality of the beam, and keeping depolarization to a low level. A possible major advantage of this scheme is the almost direct coupling between the oscillator and the passive optical resonator, to which the oscillator is locked.

The CELIA group has launched a design study along these lines, funded by the Région Aquitaine: the ELSYFO project. Table 2 summarizes the target specifications for the high average power oscillator:

Wavelength	Pulse duration	Repetition rate	Average power
1.06 μm	15 ps	80 MHz	50 W

Table 2: Target parameters for a high power oscillator.

In a first optical implementation of a high power oscillator, the CELIA group has demonstrated an output power of 21 W, with a pulse duration of 18 ps at 82 MHz, in a Continuous Mode Locking configuration, as illustrated in fig.2.

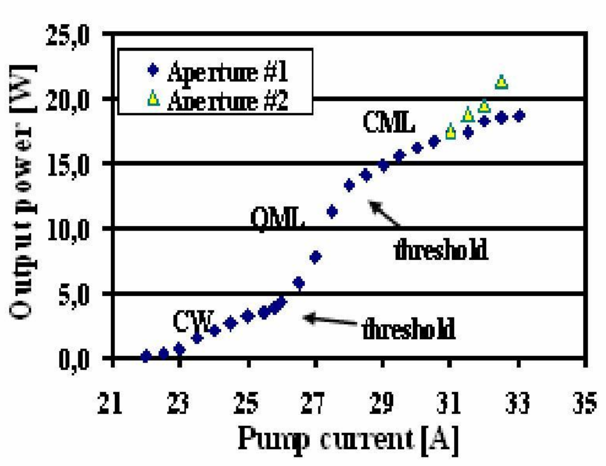

Figure 2 : Output power obtained in a first high power oscillator prototype at CELIA.

The ELSYFO program is ongoing, now aiming to develop a 50 W oscillator, based on a Nd:Vanadate crystal technology, with total characterization and minimization of the noise spectrum, especially at the injection frequency into the Fabry-Perot resonator. In order to minimize the intrinsic noise of the oscillator, the Vanadate crystal will be pumped at 888 nm in a longitudinal configuration, thus minimizing the pumping power required.

- A second very promising setup for the optical system consists of a commercial low power low noise oscillator locked on the cavity, and the brand new technology of fibre power amplifiers.

This architecture (low power oscillator / high power amplifier) has been chosen to minimise the phase and amplitude noise originating from the laser and achieve a maximal coupling into the cavity. The fibre technology has been selected for its exceptional properties of delivering excellent beam quality, its ability to handle powers in excess of 100 W without active cooling, its stability and compactness. Indeed, laser technology is nowadays experiencing a significant breakthrough in the design and realization of active optical waveguides. This technology has been initially heavily developed during the telecom market boom, some years ago. At this time, several concepts were introduced that aimed at improving fibre amplifiers performances, For instance, double clad fibres have been developed to ease the optical pumping of the active inner core material by high power diodes. Then, fibre engineering has lead to continuously increasing the inner core diameter while keeping the single mode propagation.

Using fibres as laser amplifiers has many advantages and in particular in the present context. First of all, as mentioned earlier, the amplified signal is guided during propagation in the gain medium. Assuming a real single mode fibre, the output beam should have an excellent spatial quality ($M^2 \sim 1$) which is mandatory in the case where the beam is further coupled in the Fabry-Perot cavity. Any deviation from the cavity eigenmode will be reflected and therefore not coupled. Then the active double clad fibres have a geometry that is optimal for heat removal compared to conventional bulk material. Heat is spread over long distances in fibres while it is confined in a small volume in bulk material. Most important, for a given volume of heated material, the exchange surface is way larger in a fibre than in a parallepipedic or rod crystal allowing simple air cooling up to the 100 W levels [2].

Large Mode Area (LMA) fibres have experienced an important evolution in the recent years. Commercially available double clad LMA fibres have nowadays cores as big as 40 µm. The guiding is made possible by clad index engineering such as photonic bandgaps or micro-structuration. However, these fibres suffer two main problems. First of all they are not intrinsically single mode but can be operated in the single mode regime by proper coiling inducing losses in higher transverse modes. Second, the guiding of the pump is ensured by an external outer cladding made out of polymer. When operated at very high average power, a small absorption of the pump power is sufficient to burn the polymer. To circumvent these problems, an innovative fibre referred to as rod-type photonic crystal fibre has been designed. These Photonic Crystal Fibres (PCF), or holey fibres, are special optical fibres, consisting of a Silica core surrounded by a number of air holes. An example of such a structure is presented in fig.3.

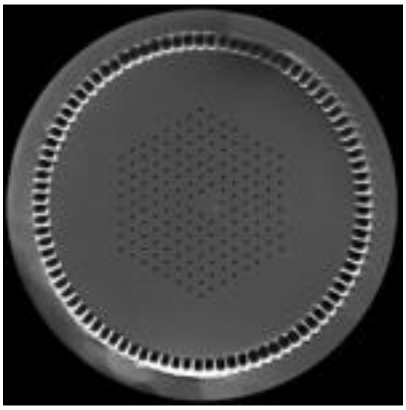

Figure 3 : rod-type photonic crystal fibre.

A first structure of holes assures the guiding of the amplified beam inside the fibre core. The second structure guides the pump beam into the fibre; finally, the fibre is surrounded by a pure silica cladding instead of a polymer coating. Such a fibre combines TEM_{00} beam quality over a large mode area (diameter varying from 40 to 70 µm) as well as excellent thermal acceptance, because of the absence of a polymer cladding. For the same reason however, the fibre is rigid and similar to a narrow rod (diameter ~1.5 mm, length ~ from 0.5 to 1.2m).

The CELIA group will develop an amplifier system based on the fibre technology. The amplifying setup will consist in a single or double stage (depending on the output power) amplifier involving double clad micro-structured Yb-doped rod-type fibres. In the present project, the rod-type fibres will have the exceptional core diameter of 80 µm while propagating single mode beams without losses. The very high gain of these fibres allows amplification in a single pass. This unique fibre has been developed during a previous project. The present project will therefore benefit from this state of the art fibre design which technology is only shared between two academic laboratories and two companies in Bordeaux.

This fibre has been implemented in several architectures that have all lead to the production of record breaking performances [3,4,5,6]. This is why we are quite confident with the outstanding performances expected at the end of the project only achievable today with such a fibre.

In the framework of the ANR project “MightyLaser”, a development roadmap has been launched, divided in two parts. A first setup will be constructed to deliver 100 W average power at CELIA by the end of year 2009. This setup will be installed at LAL and injected in the FP cavity to test the locking at high power as well as to investigate heating problems and its consequences on stability and noise in 2010. The rather simple and compact architecture (see fig.4) will implement a technique called Chirp Pulse Amplification (CPA) scheme [7]. In order to limit the non linearities in the fibre; the signal is initially stretched in time, thus reducing the intensity, amplified in the fibre and finally recompressed to its minimal time duration. In this program we will use a new technology for stretching and compression based on Volume Bragg Gratings (VBG). The advantage of this new technology is that it requires no adjustment and is definitely stable since it consists in a monolithic crystal in which a diffraction pattern is recorded. Then, the setup will be upgraded by CELIA to provide powers in excess of 200 W during 2010. Particular attention will be paid to thermal problems, stability and compactness for an easy installation and operation on the electron beam.

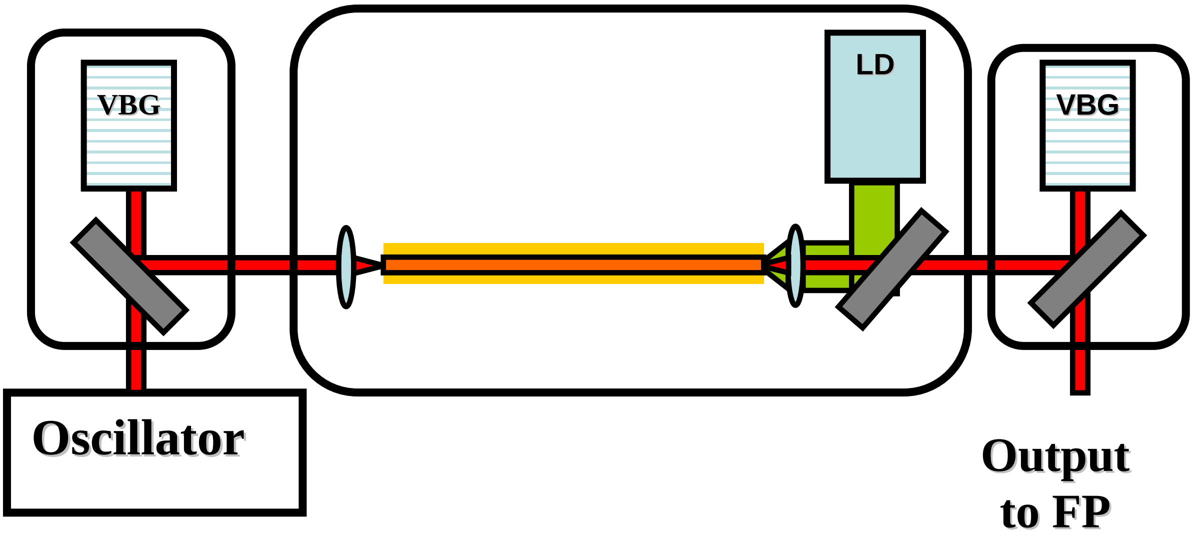

Figure 4 : Architecture of the fibre chirped pulse amplifier

There is however a difference between the target repetition rates of the MightyLaser (178,5 MHz), and ThomX (41.7 MHz) projects imposed by the repetition rate of the accelerators. The architectures of the laser amplifier need therefore to be adapted. In fact, for an identical average power, a decrease of the repetition by a factor of 4 implies an increase of the pulse energy by the same factor. The peak power thus achieved in the actual setup will lead to strong distortion of the pulse temporal quality due to severe non-linearities. This problem will be simply solved by designing new VBG inducing a stretching factor increased by a factor of 4. However, careful attention will be paid to ensure that non-linearities are totally absent and therefore no additional phase noise is generated. In a general way, the duration of the output pulses can be adjusted from 1ps to 20 ps or more.

In a preliminary experiment, we have been able to amplify pulses up to 80 W of average power and duration of 3 ps. The project will use more powerful pump diodes to reach output powers in excess of 150 W with excellent beam quality and stability.

Each configuration will give rise to accurate characterizations of the beam parameters. We will measure and reconstruct the complex electric field (phase and amplitude) in both the spatial and temporal domain. The polarization will be investigated and in particular its sensitivity to thermal load and fluctuations. As a stringent test, a fraction of the amplified beam will be injected in a FP cavity to evaluate the maximum coupling efficiency thus giving a overall quality factor of the laser system.

All the results of the current R&D projects “ELSYFO” and “MIGHTYLASER” will serve directly as inputs to the ThomX project. The dual approach will be maintained up to the final tests of injection and locking into the ultra-high finesse Fabry Perot cavity, as described below. This ensures a minimal risk for the optical part of ThomX. In spite of technical challenges that should not be underestimated, this risk management leads us to be quite confident on our ability to reach the outstanding performances expected at the end of the project.

3.1.3] Frequency doubling

In § 2.3, it has been shown that using shorter wavelengths an increase in the Compton energy cut off is obtained without changing the electron beam energy.

The production of frequency doubled pulses is an interesting option that can be studied and even implemented if successful. As far as the laser and amplifier are concerned, frequency doubling can be achieved by simply adding a non-linear stage at the output of the main amplifier. By using a BBO crystal of the proper length, we can expect efficiencies in excess of 50 %. Optimization of the efficiency will be investigated with particular non-linear media like periodically poled crystals or new crystals. Also, phase noise will be systematically recorded as we expect the noise to be doubled during the process. The risk associated with this option is minimal since it does not impact any modifications of the laser and amplifier setup.

3.1.4] Laser cavity locking

A schematic view of the optical scheme is shown in Figure 5 . The pulsed laser beam is locked to an external Fabry-Perot cavity using a feedback based on the Pound-Drever-Hall technique adapted to the pulsed regime [8]. The locking of the 1 ps pulses frequency comb to the cavity is guaranteed by a fast digital feedback using three error signals corresponding to three different parts of the frequency spectrum. It consists in eight 14-bits ADC channels, working at 100 MHz, directly connected to a FPGA with 60 ns latency time (electronic board from Lyrtech Company). Digital filters are programmed and correction signals are sent to the actuators via some of the eight 14-bits DAC channels, working at 100 MHz, directly connected to the FPGA. The choice of a digital feedback system is dictated by the complexity of the correction strategy. The various actuators that will be used to correct the laser frequency are shown in fig.5.

The locking of a 1ps pulsed laser beam was the subject of the EUROTEV/FP6 R&D at LAL (2005-2008). Using the numerical feedback described above, the LAL group has already succeeded to lock a 30000 finesse cavity to a 75MHz Ti:sa oscillator of 500mW average. Thanks to this European contract, the LAL group now possesses the requested infrastructure and expertise to provide the laser/cavity feedback system for the ThomX project.

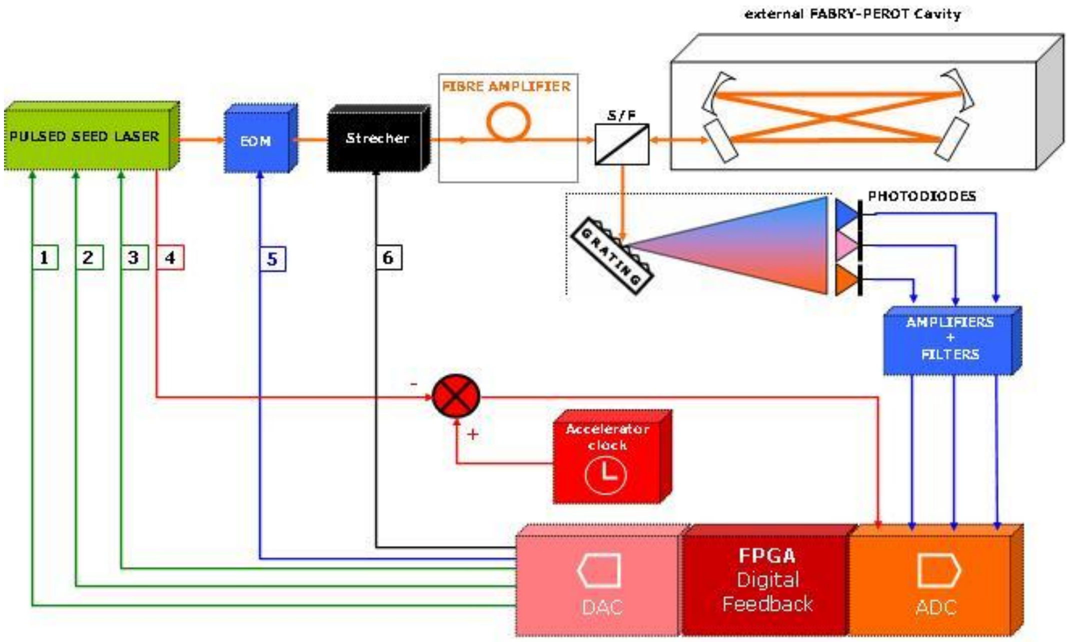

Figure 5 : Schematic view of the cavity feedback setup. Actuators list: 1=piezo–electric transducer, 2=translation stage, 3=pump diode current, 4=photodiode inside the laser head to synchronize the laser pulses to the accelerator electron bunches, 5=frequency modulation by changing the distance between the gratings of a stretcher. The laser beam is frequency modulated by an electro-optic modulator (EOM) using a modulation signal created in the FPGA (6).

The adaptation of the locking system to the new Yb doped 200 W average power laser is one of the tasks of the ANR project MIGHTYLASER. This project has started early 2009 and consists in a collaboration between the French Laboratories CELIA, LMA, LAL and the Japanese KEK Laboratory. R&D tasks of this ANR project cover in particular the following subjects, all of them essential for the ThomX project:

- Locking of a high average power pulsed laser beam to a high finesse Fabry-Perot cavity.
- Design and construction of a four-mirror cavity to be operated in an accelerator environment.
- Development of a mechanical system to match in space and time the pulse laser beam and the electron bunches
- Study of the thermal effects induced by the high average power laser beam inside the cavity mirrors.
- Installation of the whole system in the ATF electron ring at KEK (Japan) and measurement of the gamma ray flux produced by laser-electron Compton scattering.

The laser amplification and feedback systems developed for the MIGHTYLASER project will be adapted to the ThomX project with only small modifications. From the laser system point of view, the main difference between the two projects is the laser repetition rate: 178.5MHz for MIGHTYLASER and ~40MHz for ThomX. Another difference between the two projects will be the Fabry-Perot cavity geometry. The ATF electron ring circumference is a few hundreds meters long while the ThomX ring circumference will be of the order of 15m. As will be shown in the next section, this difference leads to different cavity geometry optimizations.

3.1.5] Cavity design

Three kinds of cavity geometry have been envisaged for ThomX: a two-mirror cavity **(**fig.6a), a 2D bow-tie (fig.6b) or the MIGHTYLASER 3D tetrahedron (see fig.7) four-mirror cavities. The two-mirror geometry is simpler but it is known to be mechanically unstable when small laser waists are foreseen (i.e. 'concentric' geometry). The four-mirror resonators are mechanically stable and widely used in femtosecond laser oscillator technology but the round trip power loss is higher than in the two-mirror case. In fig 6b, *L* is the distance between the two spherical mirrors, *h* the transverse distance between flat and spherical mirrors and d_2 is the longitudinal distance between flat and spherical mirrors.

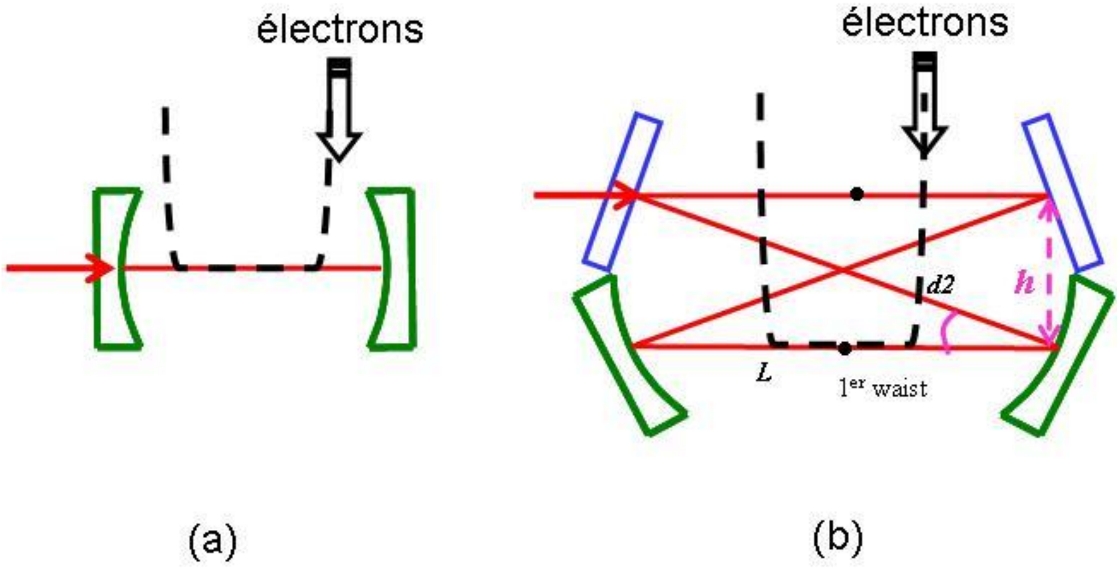

Figure 6 : (a) two-mirror cavity, the mirrors are spherical. (b) 2D bow-tie four-mirror cavity, the two upper mirrors are flat and the two lower ones are spherical.

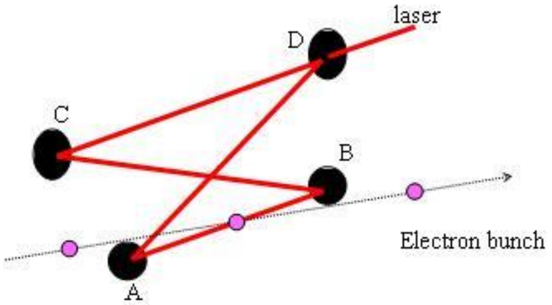

Figure 7 : Schematic drawing of the MIGHTYLASER non-planar (tetrahedron) four-mirror cavity made of two flat mirrors (C and D) and two spherical mirrors (A and B).

We have studied numerically the mechanical stability of the various optical resonator geometries. We used the Fermat principle to compute the optical axis for a given set of mirror misalignments and we defined the mechanical tolerance as the maximum displacement Δ_{max} of the optical axis on the mirror surfaces induced by all the possible angular tilts $\Delta\theta$ and/or position shifts Δr of the cavity mirrors (i.e. five degree of freedom per mirror). We fix the laser wavelength to λ=1030 nm, the cavity round trip length to 8 m, that is the second harmonic of a 16m circumference electron ring. We also fix the geometries of the cavities in order to produce a laser waist of ~80 µm (i.e. a laser intensity spot size or r.m.s. of ~40 µm) and the radius of curvature R=2 m for the spherical mirrors. We obtain: $\Delta_{max} / \Delta\theta$ ~38000 for the two-mirror cavity and $\Delta_{max} / \Delta\theta$ ~10 for 2D or 3D four-mirror cavities. The two-mirror cavity is thus ruled out whereas the four-mirror cavity exhibits a mechanical tolerance that can be handled thanks to a careful design of the mirror mounting system.

We also studied numerically the stability of the polarization of the cavity eigenmodes with regards to mirror motions and misalignments. Unlike the cavity foreseen for the MIGHTYLASER ANR project, the smallness of the ThomX electron ring allows us to consider the case h/L<<1 (see fig.6b for the definition of h and L). In this limit, we have shown numerically that the polarization of the eigen modes of a 2D cavity are as stable as those of a 3D cavity. Fixing L=2 m and h=60 mm, we obtained negligible polarization instabilities.

In addition to higher mechanical stabilities, the four-mirror cavities also provide better flexibilities for the adjustments of the cavity round trip frequency (which must be matched to the second harmonic of the electron ring frequency) and of the laser beam waist (which must be kept close to 80 µm). Indeed, it turns out that a length variation between the two flat mirrors changes the cavity round trip length without changing noticeably the laser beam waist. The laser beam waist can thus be set by tuning the distance between the two spherical mirrors independently of the cavity round-trip length.

In summary, 2D or 3D four-mirror cavities with R=2m, a round trip length of ~8 m, h=60 mm and L=2 m exhibit a sufficient degree of mechanical stability for the ThomX project. We shall show now that the 2D cavity geometry is the optimum choice for the ThomX project.

3.1.6] Mechanical Solution

The constraints for the optical cavity mechanical design are:

- a high level of stability, *i.e* suppression of the vibrations
- a good accessibility to the cavity mirrors
- a weak impact on the electron beam dynamics
- mirror positioning system to align the optical axis on the electron trajectory

We consider a four-mirror cavity with a 16 m round trip length. As described in § 3.3.4, the laser beam and electron beam collision point is located between two dipoles so that the two geometries illustrated in fig.6b and fig.7 can be envisaged. Fig.8 shows an implementation of these two geometries in the electron ring.

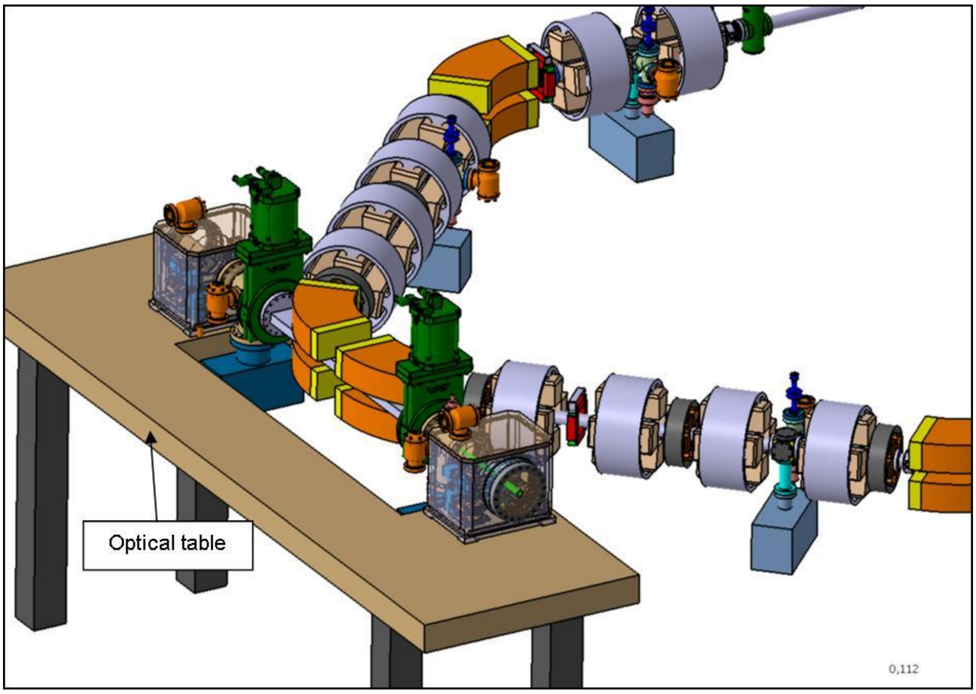

Figure 8 : Implementation of a four-mirror cavity in the electron ring. The mirrors of the Fabry-Perot cavity are mounted in the two cubic vessels located on the optical table.

However, in order to minimize the beam pipe aperture, a planar cavity as the one of fig.6b must be chosen. Moreover, as shown in fig.9, to further reduce the beam pipe aperture we introduce the 2D crossed geometry which presents the same optical properties as the 2D bow-tie geometry.

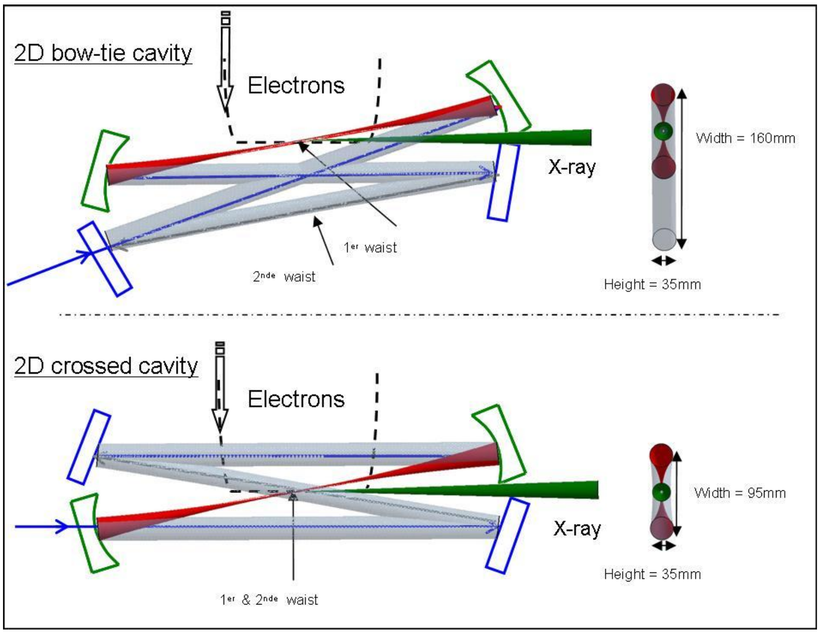

Figure 9 : Implementation of the bow-tie (top) and crossed (bottom) 2D four-mirror cavities in the electron ring. A face view of the beam pipe aperture is shown on the right part of the figure.

The cavity mirrors are mounted on a high quality optical table isolated from the electron ring thanks to two bellows. This optical table can further be moved thanks to micrometric actuators similar to the home made system used at ATF to align the cavity optical axis of the cavity to the electron beam. The two bellows also offer the possibility to move the optical table independently from the electron ring (see fig.10).

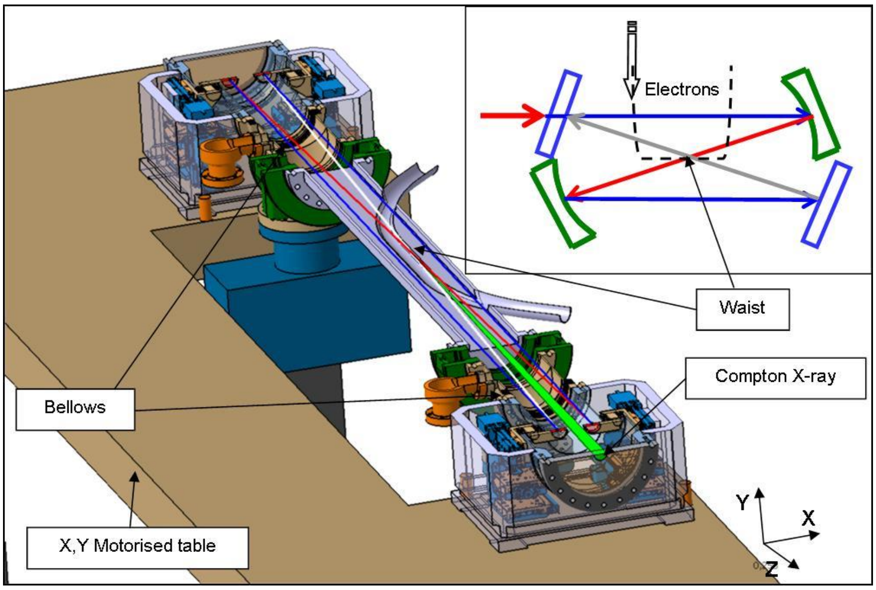

Figure 10 : Implementation of a four-mirror cavity in the electron ring.

Moreover, to isolate the optical system from acoustic vibration, we use a double vacuum chamber as shown in fig.11 and fig.12. The cavity mirrors are mounted inside a cylindrical Ultra High Vacuum (UHV) chamber. The actuation system used to align very precisely the mirrors is located outside the cylinder inside a primary vacuum vessel. This primary vacuum reduces the effect of acoustic perturbations on the actuation system and therefore on the cavity mirrors themselves. The motion is transmitted from the primary to the UHV thanks to a small bellow.

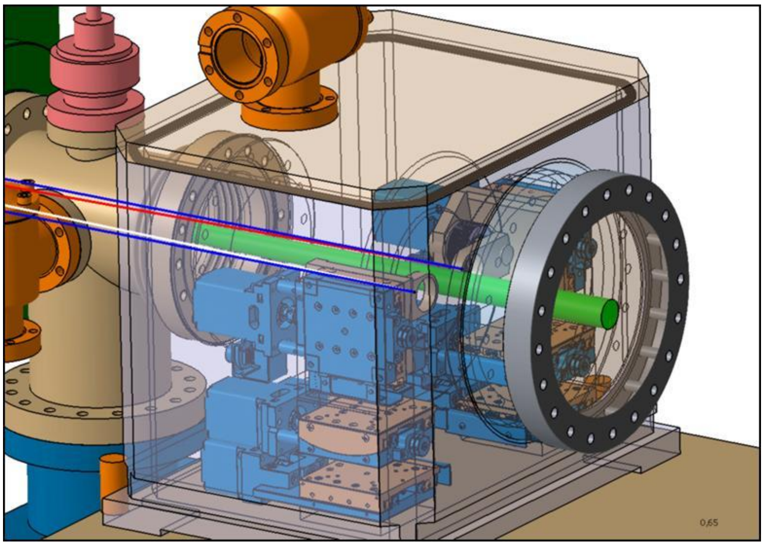

Figure 11 : Schematic view of the motorised system of two mirrors of the cavity.

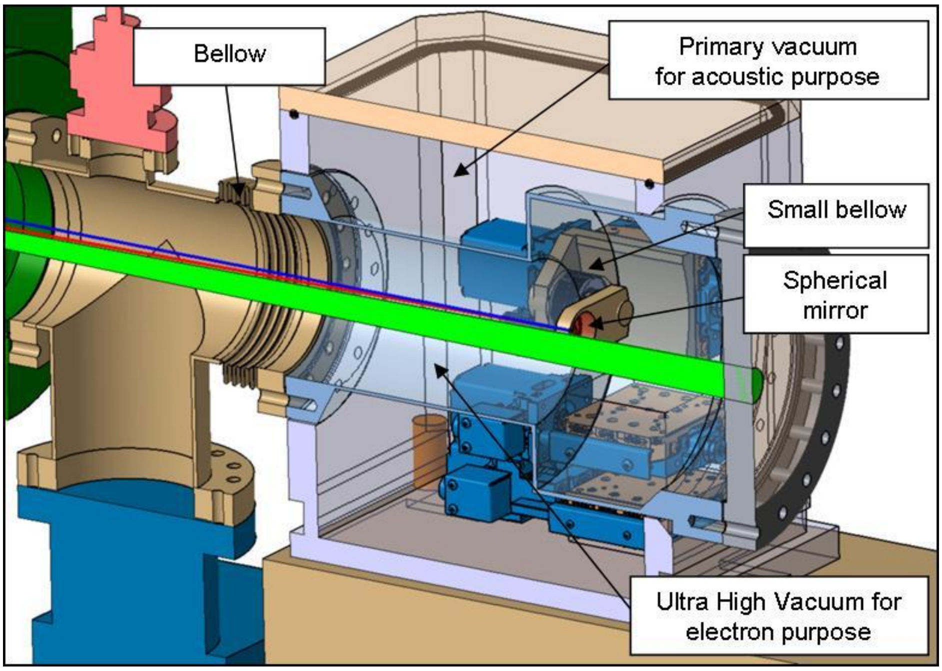

Figure 12 : Schematic view of the motorised system of two mirrors of the cavity (cut view). The mirrors are mounted inside an UHV cylindrical vessel and the actuator systems used to align the mirrors are located inside a primary vacuum cubic vessel.

The cavity mirrors are oriented very precisely using two tilting actuators per mirror (see fig.13). One of the two flat mirrors and one of the two spherical mirrors must be translated longitudinally independently. By carefully designing each mechanical element, a gimbal mirror mounting system can be constructed. It can be also shown that transverse alignment actuators are not required since the transverse shifts can be handled by the tilting actuators.

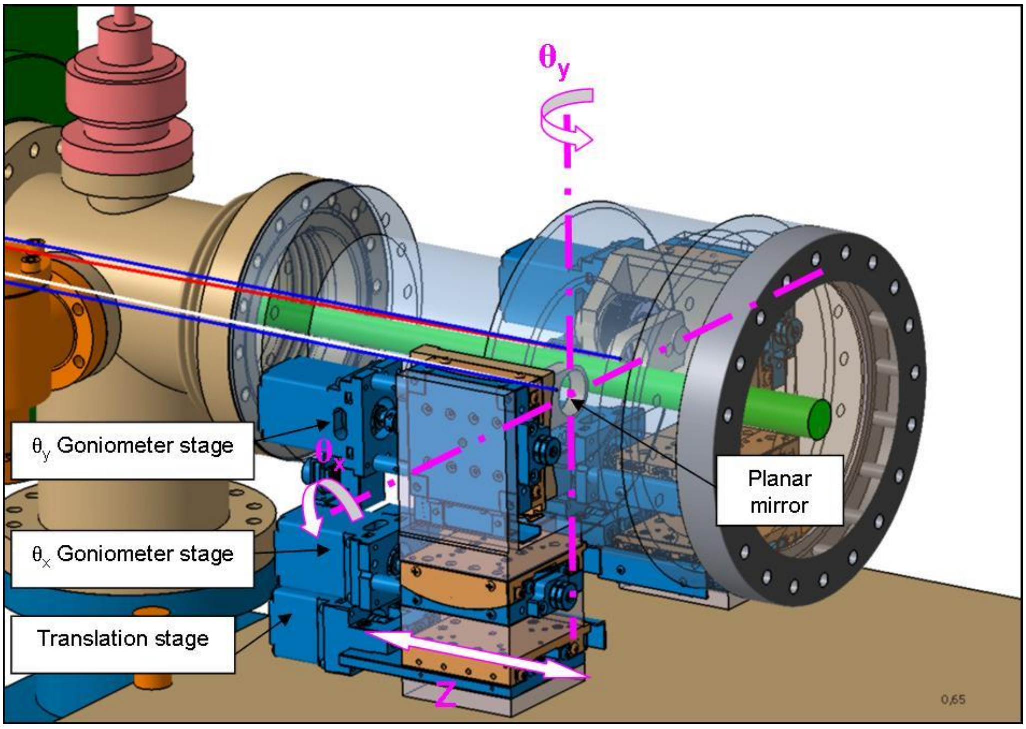

Figure 13 : Schematic view of the mirror actuators.

3.1.7] Cavity mirror coating

Multilayer dielectric coatings will be used for the high reflectance cavity mirrors. From a numerical study, it comes out that when laser pulses of time width above 1ps are circulating in a high gain Fabry-Perot resonator located in vacuum, the dispersion effects induced by the dielectric multilayer are negligible. This is indeed the time pulse width that is needed for the applications of ThomX.

The high reflectance cavity mirror will be coated at the LMA (Laboratoire des Matériaux Avancés, CNRS) of Lyon. One interesting physical aspect which has been weakly covered so far is the thermal effect in the multilayer coating of the cavity mirror. We have already started a numerical study of thermal effects in the mirror substrates induced by power absorption in the coatings. More in-depth analysis and complete simulation, including thermal lensing and mirror deformation, will be carried out within the ANR MIGHTYLASER project. Thermal measurements of the mirrors temperature chart will be performed for validation of numerical codes. Alternatively, if the necessity arises, other mirror substrates, e.g. Sapphire (for its high thermal conductivity) will be considered.

References

1] “111 W, 110 MHz repetition-rate, passively mode-locked TEM_00 Nd:YVO_4 master oscillator power amplifier pumped at 888 nm’’, McDonagh, L., Wallenstein, R., and Nebel A., Opt. Lett. 32 (2007) 1259-1261
2] “94 W 980 nm high brightness Yb-doped fibre laser”Fabian Roeser, Cesar Jauregui, Jens Limpert, and Andreas TünnermannOptics Express, Vol. 16, Issue 22, pp. 17310-17318
3] “Transform-limited 100 µJ, 340 MW pulses from a nonlinear-fibre chirped-pulse amplifier using a mismatched grating stretcher–compressor” Y. Zaouter1, J. Boullet, E. Mottay and E. Cormier Optics letters 33, 1527 (2008)
4] “High power Ytterbium-doped rod type three level photonic crystal fibre laser”, J. Boullet, Y. Zaouter, R. Desmarchelier, M. Cazaux, F. Salin and E. Cormier Optics express 16, 17891 (2008)
5] “Generation of 63 fs 4.1 MW peak power pulses from a parabolic fibre amplifier operated beyond the gain bandwidth limit”, D. N. Papadopoulos, Y. Zaouter, M. Hanna, F. Druon, E. Mottay, E.Cormier, and P. Georges Optics letters 32, 2520 (2007)
6] “Stretcher-free high energy nonlinear amplification of femtosecond pulses in rod-type fibres”, Y. Zaouter, D. N. Papadopoulos, M. Hanna, J. Boullet, L. Huang, C. Aguergaray, F. Druon, E.Mottay,P. Georges, E. Cormier Optics letters 33, 107 (2008)
7] D. Strickland and G. Mourou, Compression of amplified chirped optical pulses ,Opt. Commun. , 219 (1985) 56
8] J. Jones et al., Stabilization of the frequency, phase, and repetition rate of an ultra-short pulse train to a Fabry-Perot reference cavity, Opt. Comm. 175 (2000)409.

CHAPTER 4 : Accelerator

4.1] Injector

To fulfill the specifications of the ThomX accelerator, the linac must be carefully designed because most of the performances of the electron beam at the interaction point rely on the beam quality at the source, and mainly on the photo-injector. We choose a photo-injector as electron gun, rather than the more classical thermoionic electron gun, for two main reasons. First, the photo-injector routinely demonstrated its capacity to produce a very low emittance electron beam. Second, the use of a thermionic gun would lead to a more complex and longer accelerator because it needs a prebunching cavity and a buncher. So our insight is that the photo-injector stands for the best technical choice. For this project reliability and cost are criteria as important as the performances of the electron beam. Hence, we suggest no advanced design of the RadioFrequency (RF) gun or for the accelerating section. We used a RF gun very similar to those built by LAL [1] for the CLIC Test Facility 3 (CTF3) at CERN [2]. For the accelerating section we used the LIL [3] type traveling wave structure. The specifications for the linac are listed in table 1.

Energy	50 MeV
Charge	1 nC
Number of bunches	1-4
Emittance (rms, normalised)	< 5 π mm.mrad
Energy spread, rms	< 1 %
Bunch length, rms	< 5 ps
Repetition frequency	50-100 Hz

Table 1: specifications of the linac.

One must be aware that these parameters are determined for one operating point but the linac should be quite versatile. For instance it could be operated at higher energies as 70 MeV which will allow the users to reach X rays energies close to the double with respect to the 50 MeV case, and without noticeable increase of the cost. Nevertheless, to increase the repetition rate and the number of bunches, the cost will be higher. At present, increasing the charge up to more than 1 nC will not be interesting because the emittance and the energy spread will be degraded due to the space charge forces.

4.2]. RF simulations

In 2004 LAL acquired its expertise in the construction of 3 GHz 2.5 cells RF guns for several applications. In order to save time and reduce the costs while guarantying a reliable design it is convenient to choose one of the two models [1] which have demonstrated their good performances in the past. However a small improvement is proposed to reduce the RF power consumption as illustrated in fig.1.

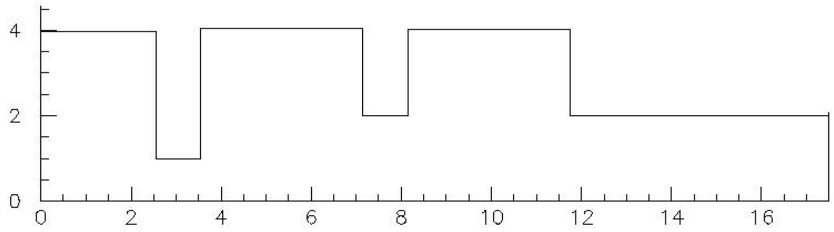

Figure 1: SUPERFISH 2D (cylindrical symmetry) model of the RF gun, vertical axis stands for the radius in cm and horizontal axis is the longitudinal symmetrical axis in cm.

The main difference of this model with respect to existing RF guns is given by the first iris between the half-cell and the middle cell, which is closer to the axis than the second iris. As a consequence, the shunt impedance is higher. A quick comparison with a model with equidistant irises with respect to the axis (2 cm) showed that emittance is also slightly better. Of course in the real model sharp angles must be avoided and the shape of the irises will be conical in order to reduce the surface electrical field. However these changes, although having an important influence on the RF performances, will not dramatically affect the results of the beam dynamics. Hence we will use the electrical field of this simplified model to study the dynamics in the linac. RF parameters are summarized in table 2.

Frequency (MHz)	2968
Q_0	15244
R_s (MΩ/m)	54
P (MW)	4
τ (µs)	0.81

Table 2: RF parameters of the gun model shown in figure 1. Q_0, quality factor; R_s, shunt impedance, P is the peak RF power and τ is the rise time of the electrical field in the gun.

The usual working frequency is 2998.55 MHz, the 30 MHz of difference in the simplified model having no influence on the results. The RF power in the table 2 is given for an accelerating peak electrical field of 80 MV/m.

Normally, after the 2D simulations, one usually uses a 3D simulation code, as Ansoft HFSS, to determine the dimensions of the cells and of the coupling apertures for the RF power. But from the beam dynamics simulations point of view, the 3D RF simulations should not influence the results. The opening of the coupling apertures has a negligible impact on the longitudinal accelerating field when the cells of the gun are also adjusted to keep a good equilibrium of the field in the different cavities of the gun. Besides the guns built at LAL have two coupling apertures symmetrically opposed with respect to the longitudinal axis. A fully cylindrical coupling allows one to improve the emittance only when one strives to reach the extreme limit around 1 π mm.mrad. This should be an option for a future upgrade.

4.3]. Beam dynamics simulations

For the beam dynamics simulations we used a version of PARMELA from Los Alamos National Laboratory modified by B. Mouton. Actually the linac is very simple since it is composed of the RF gun with its solenoids for the compensation of the space charge forces, a space of drift and an accelerating section.

a) The RF gun

The performances of the RF gun heavily rely on the choice of the laser parameters. For example the shape of the laser transverse profile can have a strong impact on the emittance of the electron beam [4]. In the simulations we assumed that the laser which produces the electrons from the photo-cathode has the following characteristics:

-square distribution as a function of the radial coordinate with a maximum radius of 1 mm.

-Gaussian distribution as a function of the longitudinal coordinate with a $\sigma_\tau = 5$ ps. Actually it would be better to also have a square profile but it is much more complicated (and therefore costly) to obtain this than in the transverse plane [5].

The peak accelerating gradient was fixed at 80 MV/m and the phase was optimized to get the minimum emittance at the output of the gun. Of course the value of the electrical field has a huge influence on the performances of the electron beam. A higher value than 80 MV/m would be better but hazards of breakdowns will be enhanced. So the chosen value is conservative since the guns built for CTF3 reached this value with a good reliability.

In the simulations the uncertainty depends strongly on the statistics; higher is the number of macro-particles better is the precision of the results. However, space charge forces are calculated point to point and it is very time consuming. Hence we used 3000 macro-particles to contain the 1 nC of charge. The longitudinal characteristics of the electron beam are not that much affected (few %). At the opposite, the beam sizes and emittances are artificially degraded by at least 20 % due to the relatively poor statistics. Results of the simulations are shown in fig.2.

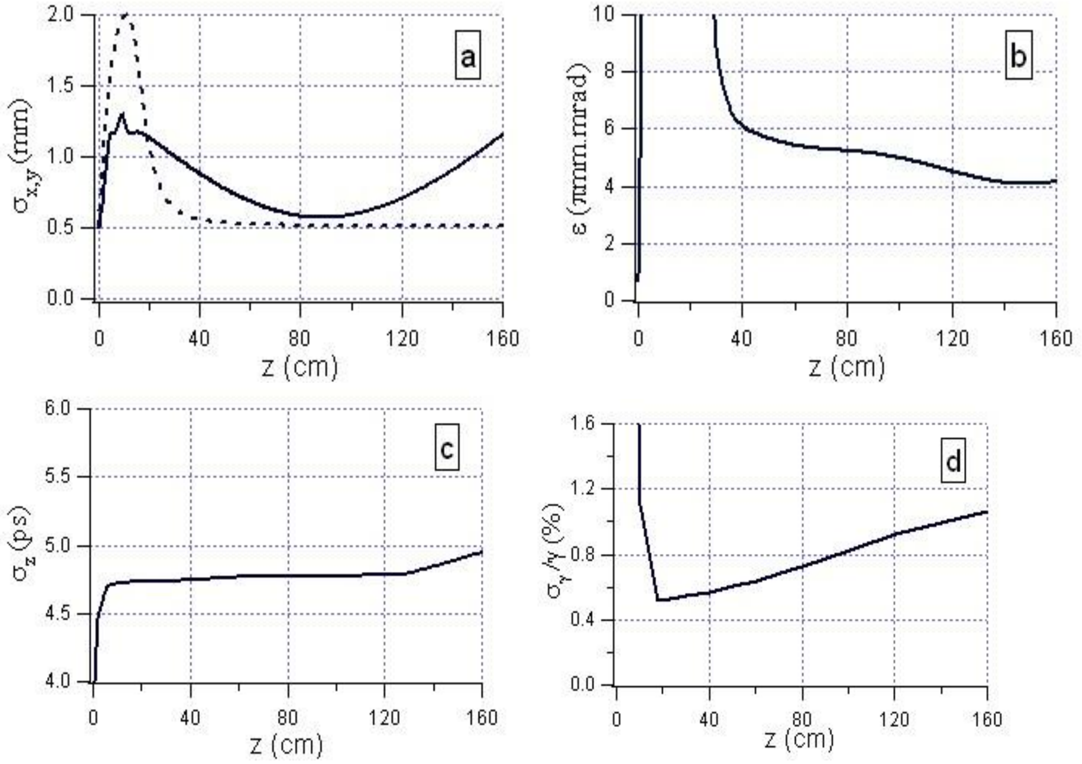

Figure 2 : PARMELA simulations, the length of the RF gun is 20 cm, the downstream distance is a drift space. All plots are r.m.s. values as a function of the distance z along the accelerator. a), beam sizes (it is the same curve either in x or in y), the dashed line stands for a schematic of the magnetic field; b), normalized emittance; c), bunch length; d), energy spread.

In the transverse plane, the electron beam is focused down to 0.5 mm, 90 cm away from the photo-cathode of the RF gun while the minimum emittance is reached only after 140 cm. The role of the solenoid, which the field is localized on the gun (see dashed line in fig. 1a) is mandatory to compensate the emittance growth induced by the space charge forces. Otherwise the emittance would be 14 π mm.mrad instead of 4 π mm.mrad at $z = 140$ cm. The optimum value of the magnetic field is 0.27 T.

In the longitudinal motion, the bunch length is quite stable while there is a linear increase of the energy spread as a function of the distance. Hence, to keep up the specifications, it implies to position the entrance of the accelerating section below $z = 140$ cm.

The choice of the position of the accelerating section must be a compromise between the compactness of the accelerator that one requires and the emittance and energy spread performances. Several simulations performed as a function of the position of the accelerating section showed that the optimum point is at 70 cm from the photo-cathode.

b) RF gun and accelerating section

As previously said we chose the LIL accelerating section which is a constant gradient type, the overall length is 4.6 m. The required peak electrical field, to bring the electron beam energy up to 50 MeV, is 12.6 MV/m. It was demonstrated during the commissioning of the LIL accelerator that this value is well inside the range of operability of the section. The RF power that one must provide for this gradient is 14 MW.

The results of the PARMELA simulations are illustrated in fig.3.

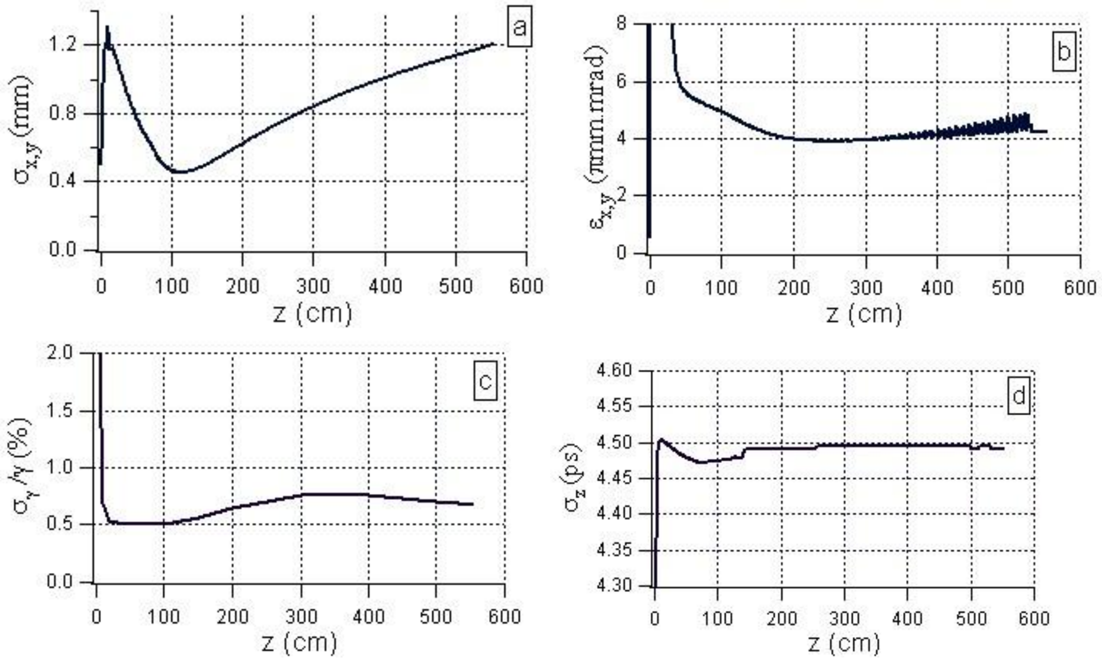

Figure 3 : results (r.m.s. values) of the PARMELA simulations for Q = 1 nC, 3000 macro-particles. Laser has a truncated Gaussian distribution: $\sigma_\tau = 5$ ps, $T_{max} = 20$ ps, $\sigma_r = 6$ mm, $R_{max} = 1$mm. In a), transverse beam size; b), normalized emittance; c), energy spread; d), bunch length.

The plots in fig.3 well illustrate the role of the accelerating section which damps the space charge force and leads to a stabilization of the beam characteristics as a function of the distance. However there is a small degradation of the emittance toward the end of the section. It comes from the RF transverse fields which influence the electron beam more strongly in the end of the section than in the beginning because, in that position, the transverse size is bigger (see fig. 3a). We tried to insert a solenoid in the end of the section to focus the beam and reduce the emittance but the opposite effect occurred. Anyway this degradation is very small with respect to our requirements. The characteristics of the electron beam at the end of the linac are summarized in table 3.

Energy (MeV)	50.4
Normalized emittance (π□ mm.mrad)	4.2
Transverse size (mm)	1.2
Bunch length (ps)	4.5
Energy spread (%)	0.68

Table 3: electron beam parameters (rms) at the end of the linac.

One must be aware that values given in table 3 are true for the over mentioned specific initial conditions. For example, if the laser transverse profile is Gaussian instead of flat top the emittance could be two times higher. At the opposite, the emittance would be smaller for smaller laser spot size on the photo-cathode. Changing the laser radius from 1 mm to 0.7 mm would lead to a reduction of 10 % of the emittance but at the expense of the energy spread and bunch length which would be enhanced by also 10 %. The only way to get a net gain would be to operate the gun at higher gradient. In SASE Free Electron Laser facilities [6], the photo-injector is routinely operated around 100 MV/m which, together with a smaller laser spot size, allows one to reach emittance as low as 1,5 πmm.mrad.

c) Operation at 70 MeV

An electron beam at 50 MeV requires 18 MW from the klystron. Taking into account the power for the RF gun and having enough margin of available power, the best suited klystron delivers around 37 MW (Thales, TH2100). It means that RF power would be available to bring the electron beam at a higher energy for a negligible additional cost. There are two advantages to increase the beam energy.

First, the geometrical emittance would be reduced thanks to the longitudinal acceleration. Indeed the relationship between the normalized emittance, ε_N, and the geometrical emittance is: $\varepsilon_N = \gamma.\varepsilon$ where γ represents the Lorenz relativistic factor. To increase the beam energy from 50 MeV up to 70 MeV leads to a 40 % higher γ and therefore a 40 % lower emittance. This would finally result in an increase of the total X-ray flux or a reduction of the X-ray beam divergence (chapter 2).

The second advantage is to get access to higher X-ray energies without changes of the laser and of the Fabry-Perot cavity used for the Compton collision. Due to the quadratic relationship between the X-ray emission and the electron beam energy, the 40 % increase of γ at 70 MeV with respect to 50 MeV leads to a doubling of the energy of the X-ray photons. To reach 70 MeV, the accelerating gradient in the section is 18.26 MV/m and the required RF power is 29 MW. Results of PARMELA simulations are given in table 4.

Energy (MeV)	70.4
Normalized emittance (π mm.mrad)	4.5
Transverse size (mm)	0.9
Bunch length (ps)	4.5
Energy spread (%)	0.57

Table 4: electron beam parameters (rms) at the end of the linac for Q = 1 nC, 3000 macro-particles. Laser: $\sigma_\tau = 5$ ps, $T_{max} = 20$ ps, $\sigma_r = 6$ mm, $R_{max} = 1$mm.

Comparing the values in table 3 and 4 shows that performances of the electron beam at 70 MeV are not so different from those at 50 MeV. The beam size is lower due to the reduction of the geometrical emittance as explained above. One can notice also the slight reduction of energy spread at 70 MeV.

4.3.1] Summary

A first simple design of the linac is proposed. It is based on proven technologies and the results of the simulations showed that it easily fulfills the specifications. With a small R&D effort on the photo-injector it could be possible to reach a very low emittance leading to an enhancement of the X-ray source beyond the initial scope.

4.4] Transfer line

Once the linac has been designed, the electron beam is transported through a so called transfer line to the storage ring. At the end of the transfer line, the performances (mainly the emittance) of the electron beam must be equal to those at the end of the linac. In other words, the line must be achromatic in order to preserve the emittance. In addition to this main task, the transfer line must fulfill a second function which consists in an adjustment of the bunch length for the injection. At the output of the linac, the bunch length is 4.5 ps. Added to a charge of 1 nC, tremendous instabilities raising from wake fields would appear after the injection in the ring, and they would jeopardize the Compton interaction with the laser beam (see § 3.4). To avoid emittance growth the bunch must be lengthen up to 20 ps at least. The transfer line is used as a magnetic chicane in which an adequate correlation between the longitudinal position of the electrons and its energy leads to a lengthening of the bunch thanks to the energy dependant trajectories of the electrons in the dipoles. This effect is well known although usually it is used for the opposite goal, e.g. the bunch compression in magnetic chicane as in SASE Free Electron Laser [7].

As far as the design of the transfer line is concerned, it has been chosen not to lengthen further the accelerator. So the storage ring is positioned below the end of the linac and the electron beam is transferred to a straight section of the ring via a loop at 180°. The design is illustrated in fig.4.

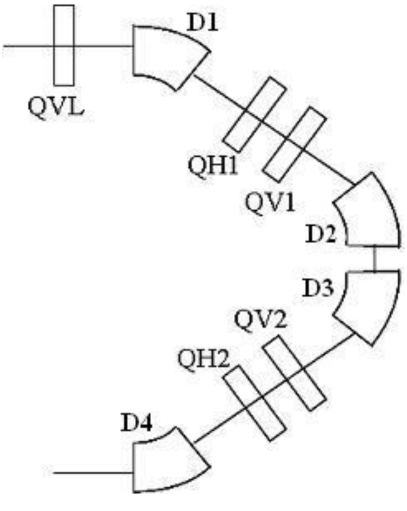

Figure 4 : schematic of the transfer line between the linac and the storage ring; D stands for a dipole, QV means a quadrupole focusing in the vertical plane, QH means a quadrupole focusing in the horizontal plane.

Since we strive to introduce a standardization of the components (to reduce the costs) the magnetic elements are the same as used in the storage ring. The distance between each element is 20 cm except in between the two dipoles in the middle of the line where it is 10 cm.
To find the values of the quadrupole gradients, we have used a well known code, TRANSPORT [8] which is well adapted in this case. This program does essentially a multiplication of the transfer matrix of each element. Moreover there is the possibility to set conditions, achromatic transport for instance, and the code performs iterative loops to find the gradients of the quadrupoles which fulfill the conditions.
In the input file for TRANSPORT, the elements of the beam matrix are derived from the characteristics of the electron beam at the end of the linac (see chapter 3). The values found by TRANSPORT for the quadrupoles are collected in table 4.

QVL	-2.277
QH1	1.476
QV1	-1.585
QV2	-1.295
QH2	1.302

Table 4 : values of the quadrupoles gradient in T/m found by TRANSPORT.

First one can notice that no value of quadrupole gradient exceeds 5 T/m which is the maximum sustainable according to the magnetic design of the quadrupoles (see § 4.6.1). The results of the beam dynamics with this magnetic configuration is illustrated in fig. 5.
So, with the settings of the quadrupoles found with TRANSPORT, we succeeded to preserve the emittance value at the output of the transfer line. Moreover the bunch length reaches 25 ps at the output, fulfilling the requirement for this transfer line. This simulation allows seeing that the horizontal beam size becomes very large in the middle of the line, almost 6 mm. Therefore it will be necessary to use an elliptical vacuum chamber whose the aperture (diameter) would be roughly 100x40 mm^2 in the interval defined by [QV1,QV2]. Besides, the quadrupole focusing scheme could be also improved to reduce the horizontal dimensions of the beam along the transfer line.
After the half turn, the electron beam will be injected into the ring thanks to a dipole at -8°, a septum magnet which cancels most of the deviation and finally a kicker integrated in the ring to compensate the residual angle (≤ 1°). The design of the dipole and the septum should not present special difficulties except that the dipole must be compact because it will be very close to the storage ring. On the opposite, the kicker magnet can present some difficulties because of the response time that one requires. Indeed, for obvious reasons, the time while the kicker is active must be smaller than the revolution time of electrons in the ring, namely 48.5 ns. This is the basic requirement but an important upgrade should be to operate in a two bunches mode in order to enhance the X-ray flux. Therefore the time response of the kicker magnet must be faster than 24 ns, and it represents quite a challenge.

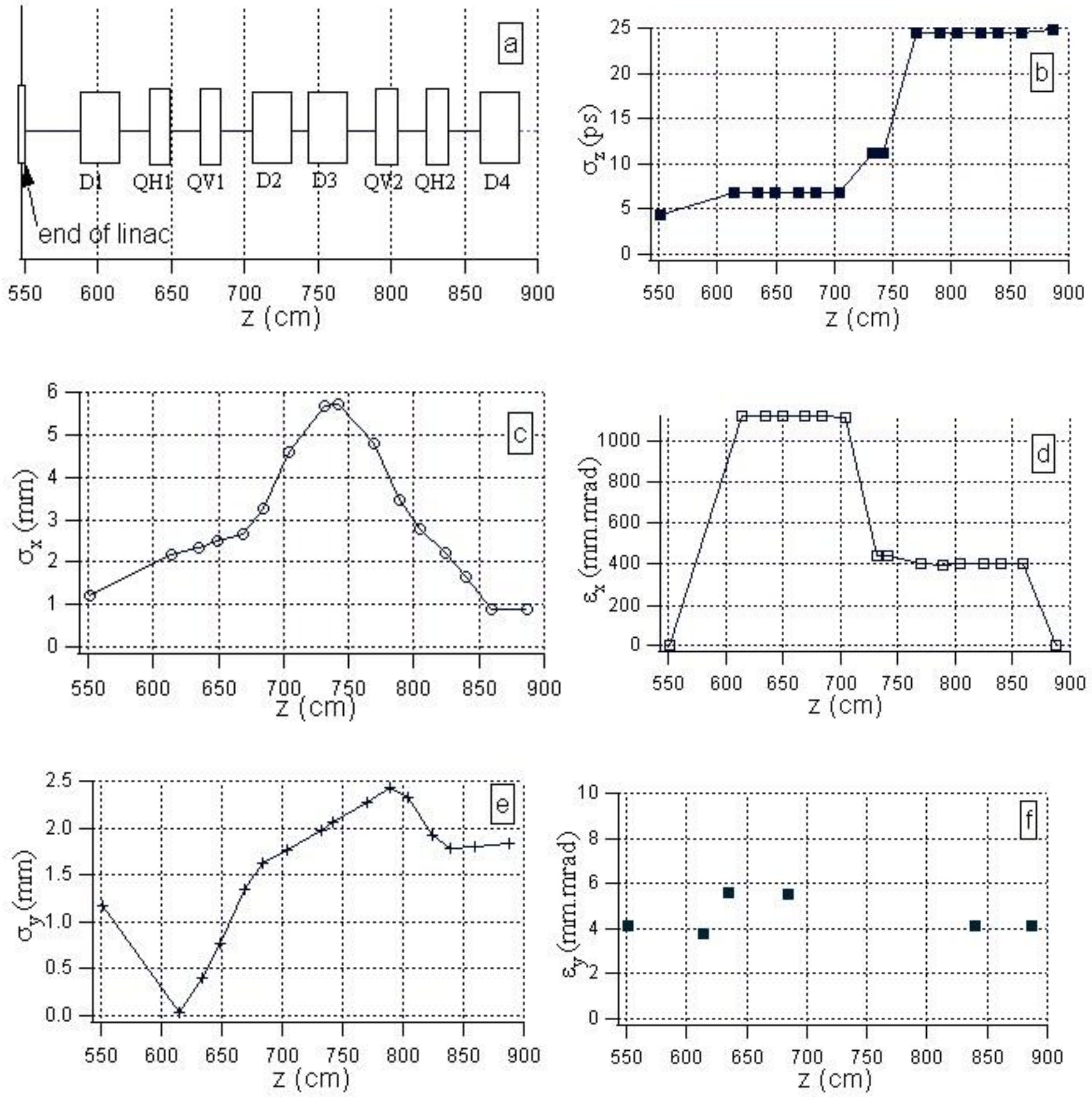

Figure 5 : results (r.m.s.) of beam dynamics simulations with TRANSPORT as a function of the distance along the beamline; a), schematic of the transfer line; b), bunch length; c), horizontal beam size; d), normalized horizontal emittance; e), vertical beam size; f), normalized vertical emittance.

Finally, the results found with TRANSPORT must be taken with caution because it deals with ideal beams with a Gaussian distribution. In one hand this assumption is true in the transverse plane, in the other hand the longitudinal distributions in time and energy strongly differ from a Gaussian as shown in fig.6 according to the PARMELA simulations of the linac. It is due to the on crest acceleration which introduces a non linearity of the electron energy as a function of its longitudinal position with respect to the RF phase.

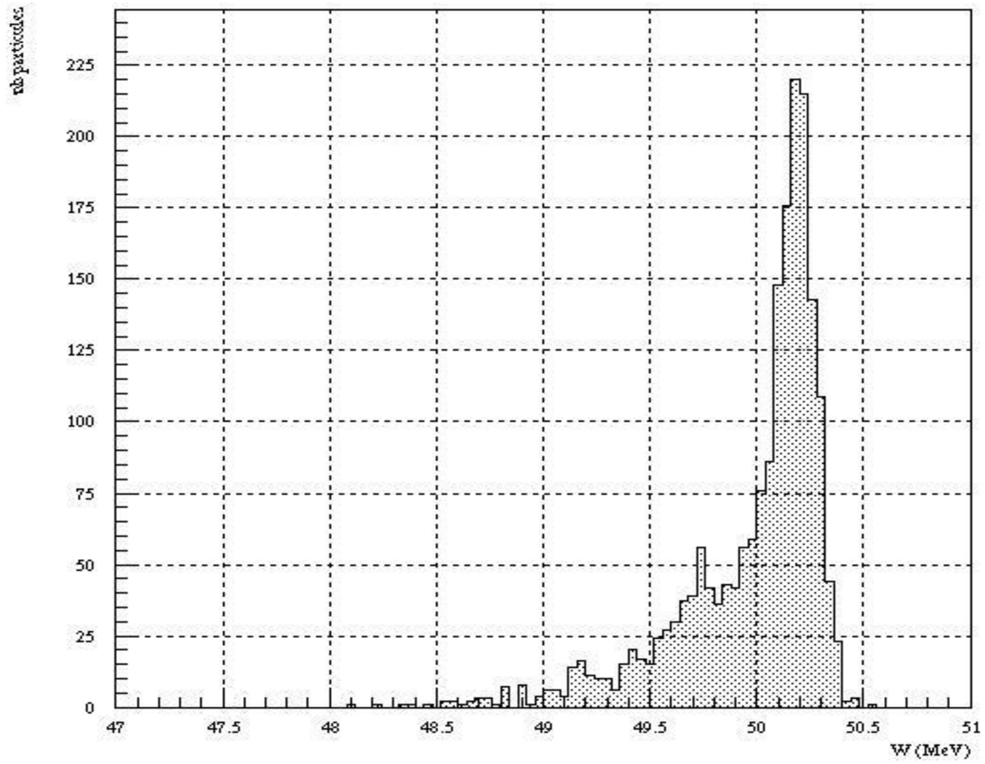

Figure 6 : energy spectrum of the electrons at the output of the linac.

With the optics found with TRANSPORT, the dispersion is normally corrected but only for the electrons which are inside the Gaussian distribution. The electrons outside this limit are not corrected and can lead to a blow-up of the horizontal emittance when the latter is statistically calculated in r.m.s. value as in PARMELA. To overcome this drawback there are two possibilities: either transport the beam like it is and accept that roughly 10 % of the charge will not participate to the Compton interaction either accelerate the beam off crest in the linac to get a Gaussian distribution. In the first option, it could be judicious to install a collimator, between D3 and QV2 for example, to clean properly the beam instead of propagating useless particles. In the last option, one can expect degraded performances since the beam with the best quality is obtained with the on crest acceleration.

4.5] Ring optics and beam dynamics

4.5.1] Main requirements

The high X-ray (<50 keV) flux has to be of the order of 10^{13} ph/s and relatively constant over time. The flux depends on the characteristics of the electron bunch and of the laser pulse (see § 3.4.12). In the standard operation, the ring is filled with only one bunch. With 1 nC electron bunch charge, 50 MeV and about 20 to 30 mJ in the laser pulse (@ 1.06 μm), the constraints at the Interaction Point (IP) are:

1. Transverse r.m.s. size of the electron beam less or equal to 70 μm (see § 4.5.9) in transverse planes leading to low beta function of 0.1 m with an r.m.s. geometric emittance of 50 π nm.rad injected from the linac.
2. Zero dispersion function at the interaction point to avoid beam size widening while the bunch energy spread is increasing as well as potential synchro-betatron coupling resonances.

3. Bunch length of about 20-30 ps : short enough to achieve an efficient X-rays production with a laser crossing angle of 2°, and long enough in order to reduce the collective effects (beam pipe impedance, Coherent Synchrotron Radiation, particles inner scattering ...)

Beside these specific IP constraints, general layout constraints are:

4. Ring circumference as short as possible with enough straight sections space to accommodate the IP, the RF cavity, the injection and possible other equipments such as kickers for longitudinal and transverse feedback systems (see § 4.5.7).

5. Some flexibility for the optics and the working point

The first difficulty with the low energy ring is that there is no short term damping. At 50 MeV, it takes about few second to damp one e-folding by synchrotron radiation. Consequently, the injected bunch has to be on axis (no accumulation) and is very sensitive to every kind of mismatch in terms of positions and sizes. Mismatch will lead to oscillation and emittance growth inducing X-ray flux reduction. The second difficulty that is met at low energy is the high sensitivity to the wakefields. A careful design of the vacuum chamber has to be worked out and the impact of wakefields including Coherent Synchrotron radiation (CSR) and Longitudinal Space Charge (LSC) has to be investigated as well as a careful HOM care (see § 4.5.7). In addition, the Compton interaction has an effect on the electron bunch turn after turn and tends to deteriorate its characteristics by cumulative recoil effects. Accordingly, the bunch has to be stored in a sufficiently short time before a too large deterioration. The bunch is then ejected and replaced by a new, fresh one from the linac.

4.5.2] Linear optics

Several optical structures are possible for this type of compact ring. The most popular for low energy Compton machines is a Chasman Green or a Double Bend Achromat (DBA) where the ring has only four dipoles. For this type of structure two main sections are required to accommodate the injection and RF cavity, and for the IP. It requires relatively strong sextupoles to correct the chromaticities, resulting in additional harmonic sextupoles in the non dispersive sections to reach a comfortable dynamic aperture.

To favour flexibility, the first choice turned into a ring with four fold symmetry Double Bend Achromat (DBA): eight dipoles and four long straight sections. To improve the compactness, the next step was to reduce two opposite long straight sections by removing quadrupoles and reducing the free space between the two adjacent dipoles (see fig.7). With this optical structure, there are two possibilities for the optical cavity integration:

a) In the long straight section (see fig.8a)

b) In short straight sections between adjacent dipoles (see fig.8b).

Case a) allows the standard 3D cavity designed for implementation on ATF to be used. However, including specific strong focusing, there are difficulties to integrate the other equipments (RF cavity and injection) in the remaining opposite long straight section. In case b), this constraint is lifted and the two long straight are fully dedicated for injection and RF cavity. A planar optical cavity (2D) located in between the adjacent dipoles naturally fits the dipole bore gap. In addition, the optical cavity mirrors can be accessed more easily being located out of the ring and Compton extraction cone is close to IP (thanks to the dipole curvature). In the following, the configuration b) will be assumed as a baseline while the configuration a) will be considered only as an option.

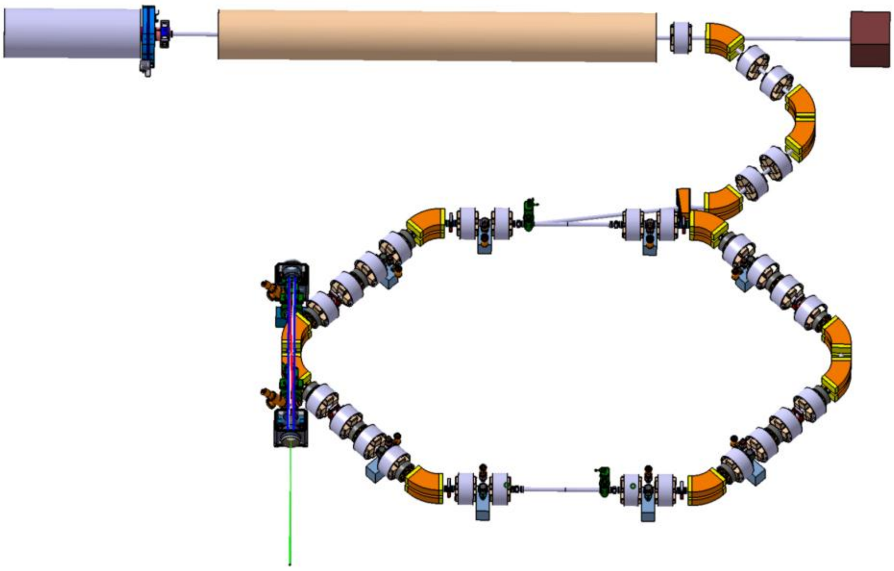

Figure 7 : Ring sketch: Red dipoles, blue: quadrupoles, black sextupoles, green: correctors

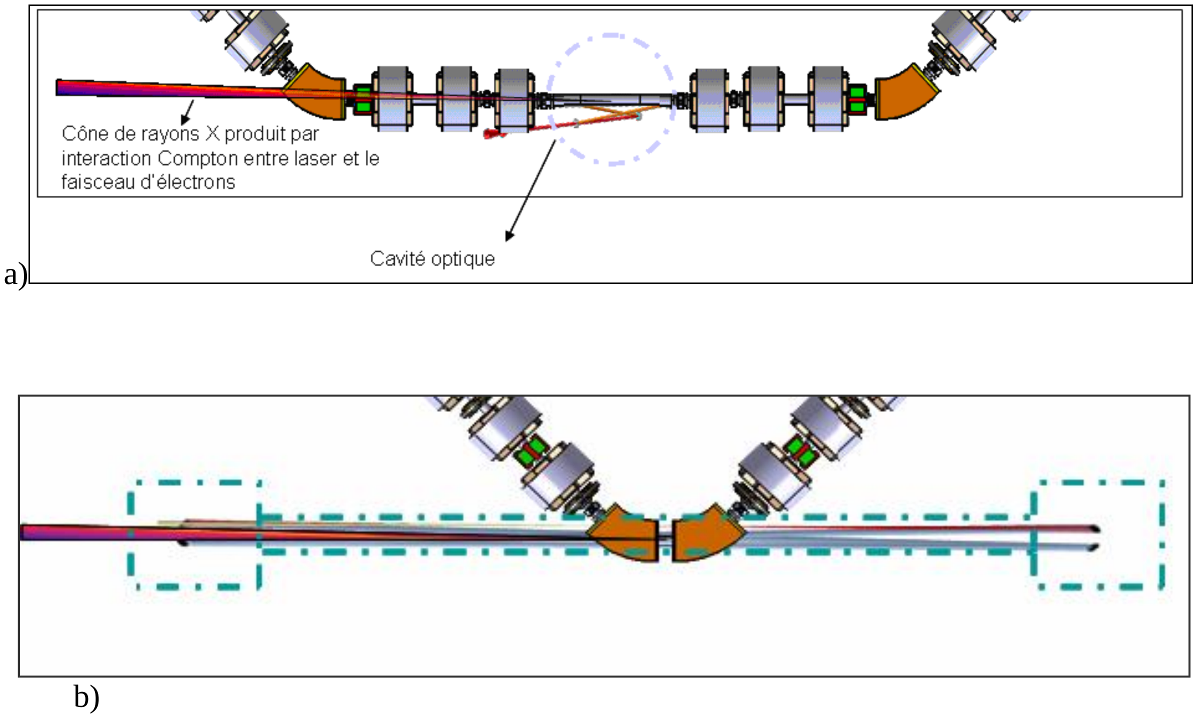

Figure 8 : a) Standard IP configuration, b) IP inserted in adjacent dipoles

4.5.3] Optics optimisation

The optics has been optimized with the code BETA [9]. With two long (1.2 m) and two short (0.2 m) straight sections the optics presents a two fold symmetry. The focusing of the four arcs is provided by quadruplets having the advantage to allocate free space in between for sextupoles, correctors etc… . Four sets of doublets complete the focusing in the long straight. The ring is composed of 8 dipoles, 24 quadrupoles and 12 sextupoles. The circumference of the ring is 14.57 m providing a revolution frequency of 20.7 MHz. With a 500 MHz RF frequency, the harmonic is 24.

Circumference (m)	14.47
Nominal energy (MeV)	50
Filling mode	1 bunch
Betatron tunes ν_x, ν_z	3.4 / 1.4
β_{max} x,z (m)	11 / 11
Dispersion max (m)	0.9
$\beta_{x,z}$ and dispersion @ IP (m)	0.1 / 0.1 / 0
Momentum Compaction Factor	0.0148
RF frequency (MHz)	500
RF harmonic	24
RF voltage (kV)	300
Period (ns) / Revolution frequency (MHz)	48.5 / 20.7
Natural chromaticities	-3.2 / -8.2
Dipole number, family & field (T)	8 / 1 / 0.5
Quadrupole number, families & gradient (T/m)	24 / 6 / <3
Sextupole number, families & gradient (T/m^2)	12 / 2 / <30

Table 5 : Main parameters of the lattice

The general parameters of the ring are shown in Table 5. The optical functions along the ring are illustrated in fig.9b. The dispersion is cancelled for both long and short straight sections (RF, injection and IP). The beta functions down to 0.1 m at IP provide a waist of 70 μm with an injected emittance ε of 50 π nm.rad (γε = 5 π mm.mrad) in both vertical and horizontal planes. Taking into account the constraints associated with optical functions, chromaticity and dynamic aperture, the operating point was chosen with tunes: ν_x=3.4 and ν_z=1.4 (see fig 9a). This corresponds to a difference resonance (ν_x-ν_z=n) which is generally convenient for round beam (i.e.: same emittance in Horizontal and Vertical planes). There is still enough flexibility to vary the tunes over +- 0.2 without spoiling the main characteristics (see fig.9b).

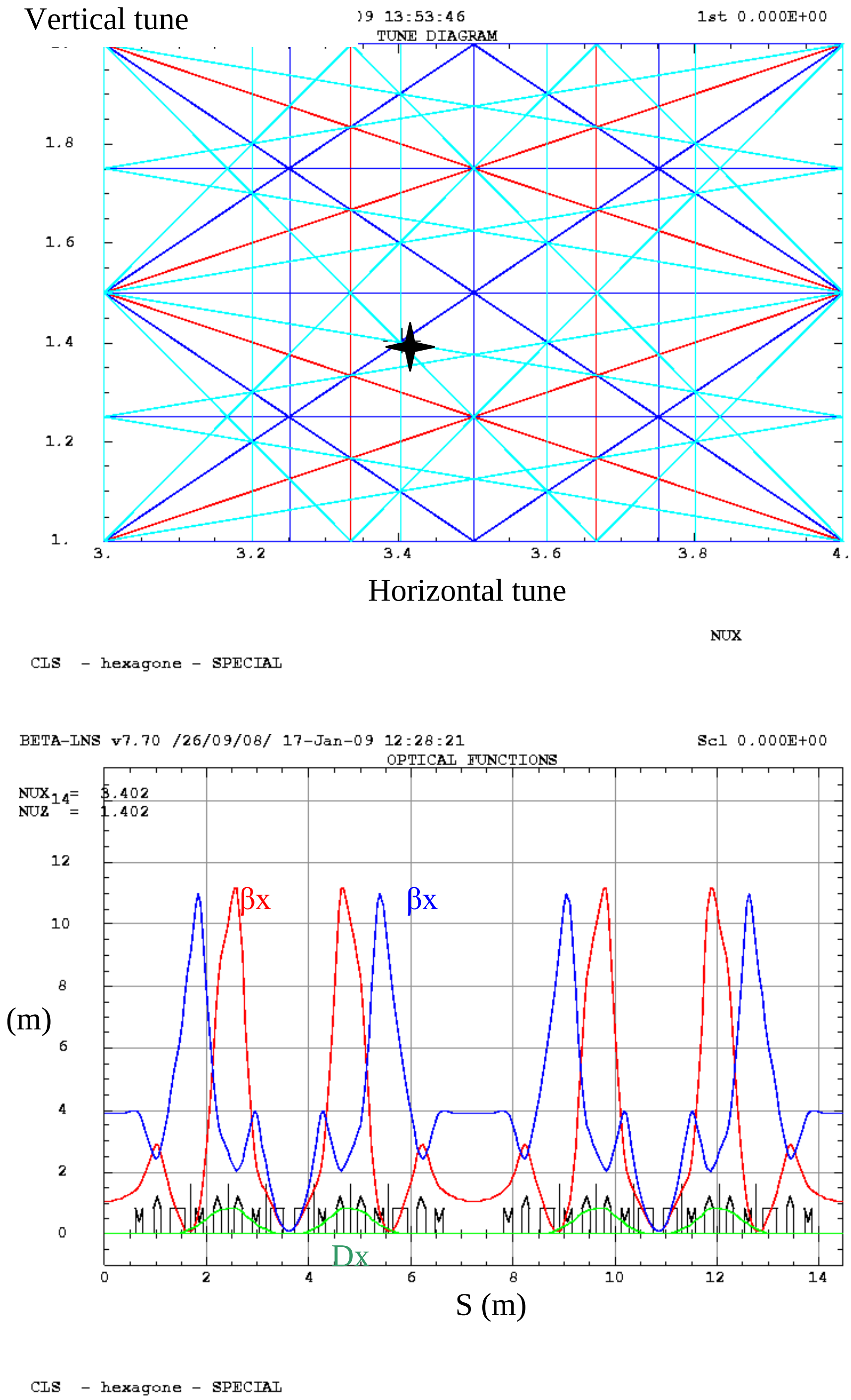

Figure 9 a,b : a: Tune diagram. Resonances of order 2 (black), 3 (red), 4 (dark blue) and 5 (light blue) are represented. The cross corresponds to the working point. b: Optical functions along the ring. The horizontal betatron functions are represented in red, vertical blue and green the dispersion is shown.

Natural horizontal and vertical chromaticities are respectively -3.2 and -8.3. Chromatic corrections are achieved by means of 12 sextupoles (2 families) in the dispersive sections arranged symmetrically in the achromat, one in the center of the quadruplet and two others adjacent to the dipole. Without specific optimization, the dynamic aperture is large enough about 50 times the r.m.s. size of the transverse injected beam (fig.10a). In addition, it remains the same order of magnitude for off momentum particles compared to the nominal energy of

±3% (fig.10a). These simulations only include the sextupole in thin lens model as non-linear components. Fringe fields and geometrical higher order multipoles are not included. A special attention will have to be paid concerning the fringe field with respect to the short magnets as well as their close neighbour.

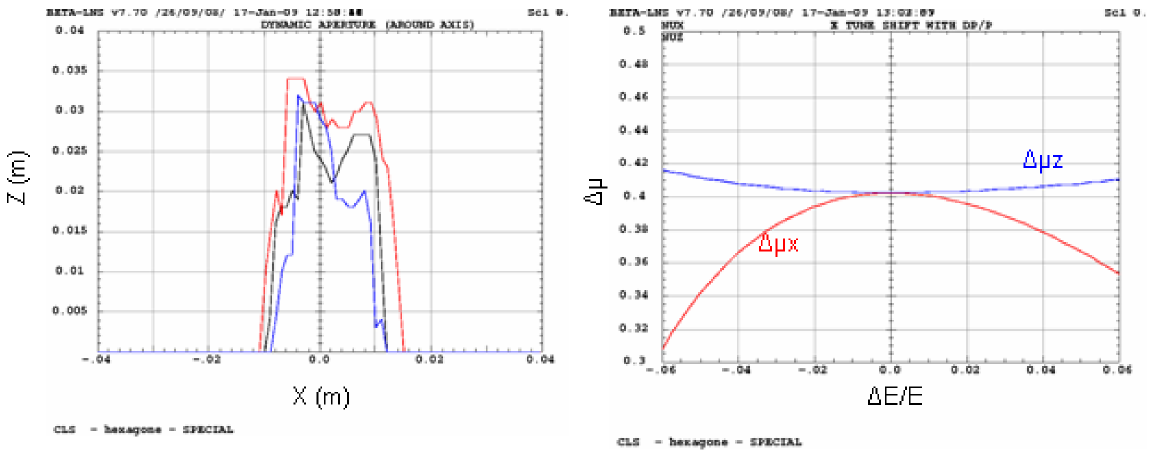

Figure 10 a,b : a : Dynamic aperture at injection for different values of dE/E, dE/E=0: black, dE/E=- 3%: blue, dE/E=3%: red, b: Tunes variation (red : ν_x and blue : ν_z) versus dE/E.

4.5.4] Second order momentum compaction

The strong focusing and the short bend radius of the lattice induced significant second order momentum compaction α_2. This non-linear term produces an asymmetric longitudinal phase space distortion that may severely limit the energy acceptance. It is derived from the slope of the dispersion function D'_1 and the second order dispersion component D_2 :

$$\alpha_2 = \frac{1}{L}\oint\left(\frac{D_1'^2}{2}+\frac{D_2}{\rho}\right)ds$$

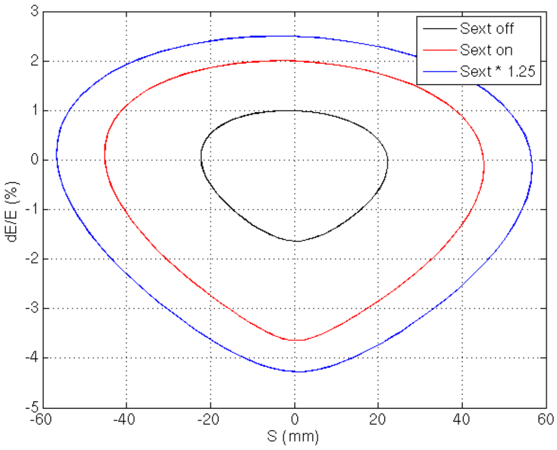

Cases	*E_accept*	*Chrom*
Sext off	+1 / -1.8%	-3.2 / -8.3
Sext on	+2 / -3.6%	0 / 0
Sext * 1.25	+2.5 / -4.3%	2.4 / 2.8

Figure 11 : Energy acceptance versus sextupoles: Without sextupoles, with chromaticities corrected to zero and sextupole strength increased by 25 %.

Without sextupoles, the α_2 term is very strong and reaches 0.72 (as compared to α_1=0.015). The RF energy acceptance is then reduced to +1% and -1.8% (fig.11). Setting the chromaticities to zero, α_2 is then reduced to 0.38 and the RF energy acceptance is doubled to +2% and -3.6%. The vacuum pipe energy acceptance is about +3.9% and –3.5% at second order. The real energy acceptance is then about 2% which is reasonable to keep the particles during the 20 ms cycle with an rms energy spread varying from 0.3 to 0.6% (see. § 4.5.9). α_2 can be further reduced to 0.3 by increasing the sextupole strength by 25%. The RF energy acceptance is then +2.5% and -4.3% and the chromaticities are 2.4 and 2.8 in both planes. The real energy acceptance is then also increased to about 2.3%. In this later case, the dynamical aperture is slightly reduced by 15%.

In summary the real energy acceptance including the vacuum pipe limit (±30 mm in horizontal) and the RF limit versus the sextupoles strength are:

Cases :	***Sext off***	***Sext on***	***Sext*1.25***	
E acceptance	~1	~2	~2.3	%

4.5.5] Integration of the optical cavity

In this ring configuration, the 2D optical cavity described in previous chapters fits naturally in the short section (see fig.12). The laser frequency is the harmonic 2 of the revolution frequency of the bunch in the ring, i.e. 41.4 MHz. This leaves a possibility of storing two bunches in the ring to increase the Compton flux. On the other hand, the mirrors of the optical cavity are located outside the path of electrons, thus acting on the mirrors changes without affecting the ring integrity. In addition, extraction of the Compton cone can be made closer to point source than in the case of option a (cavity on a large section) (see fig.12).

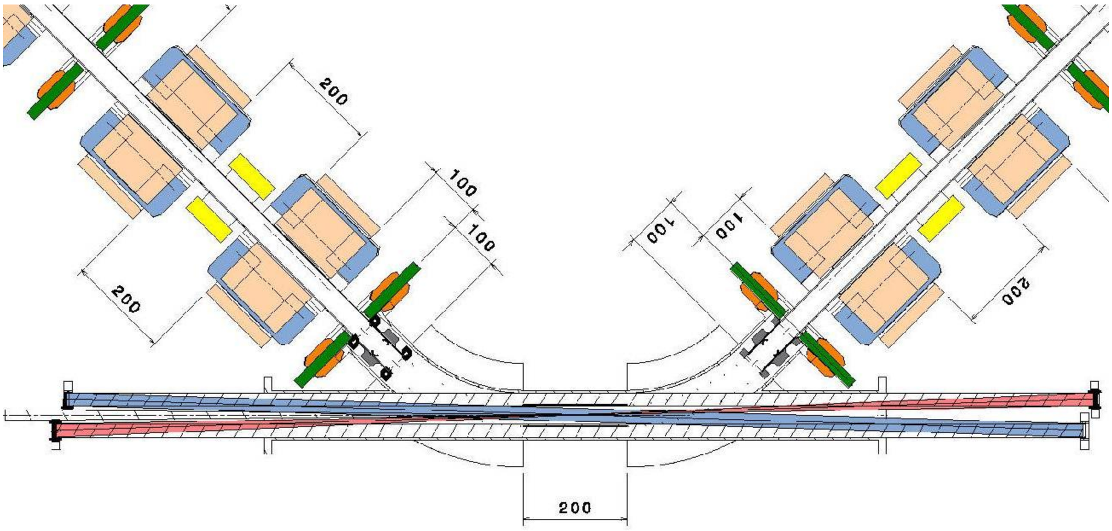

Figure 12 : Schematic location of the 2D laser cavity.

4.5.6] Orbits

Closed orbits induced by misalignment are plotted in fig.13. The main contributions are quadrupole transverse displacements as well as dipole tilt around the s axis. With respectively 200 µm and 0.5 mrad r.m.s., the peak closed orbits reaches about 4 mm r.m.s. in both planes. A set of 8 correctors and 12 Beam Position Monitors (BPM) located along the machine enable to reduce closed orbit amplitudes down to 0.2 mm r.m.s. in both planes. The corrector strengths are moderate with maximum r.m.s. deviation of 0.3 mrad.

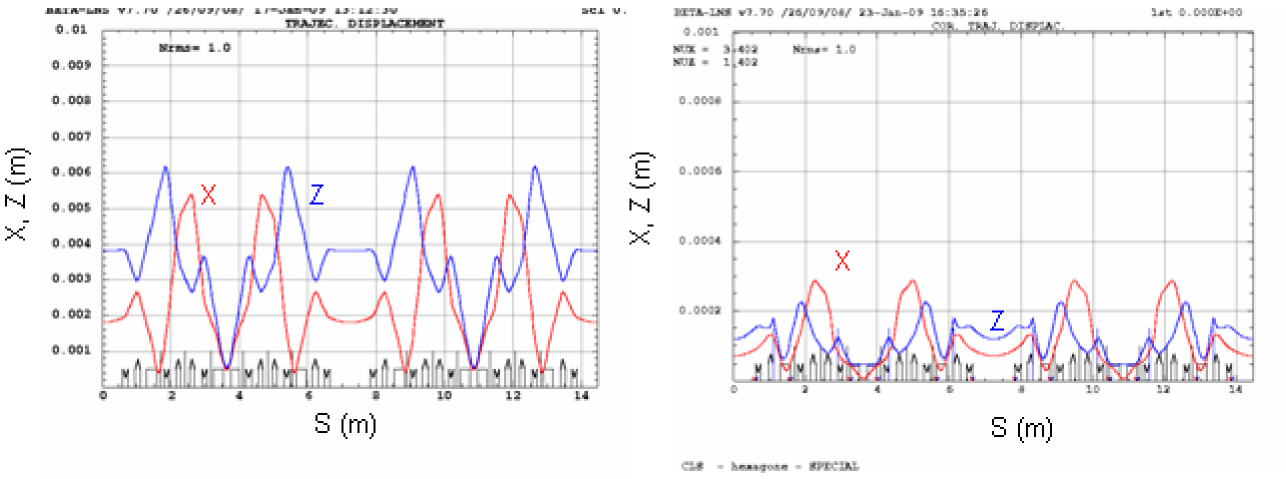

Figure 13 : Closed orbits (left) and corrected closed orbits (right)

4.5.7] Collective effects

At low energy, the electron bunches are sensitive to various kind of self electromagnetic perturbations that act turn after turn in the ring. They are of different types:

1. Geometrical, from the surrounding vacuum vessel as Resistive Wall (RW), RF cavity and various discontinuities : bellows, BPM, flanges, etc ...
2. Space charge forces
3. Coherent Synchrotron Radiation (CSR)

The interaction is described by wake fields in the time domain or impedances in the frequencies domain. In the longitudinal space, this interaction affects the bunch energy and time profiles leading to distortions, emittance growth or even instabilities and beam loss above a given threshold. With a large spectral covering, they are known as broadband instabilities. The two relevant parameters for the instabilities threshold are the bunch charge and length. The interaction is proportional to the charge (or current) and with different order, inversely to the length of the bunch.

The two following plots in fig.14 represent the different order of magnitude of the longitudinal wakefields over one turn at 50 MeV along the 1 nC Gaussian bunch with a r.m.s. length respectively of 4 and 20 ps (1.2 and 6 mm). The different longitudinal wakes are:

- Shielded CSR [10] with a full beam pipe height of 40 mm, dipole field of 0.5 T and a curvature of 0.352 m.
- Longitudinal Space Charge (LSC).

- ➢ Resistive Wall (RW) [11] with a full beam pipe height of 40 mm and an electric conductivity of 1.4 10^6.
- ➢ The vacuum vessel broadband component including 8 BPM, 12 Flanges and 12 bellows based on the synchrotron SOLEIL type [12] (see appendix 2).
- ➢ The 500 MHz ELETTRA [13] type cavity broadband component (see appendix 2).

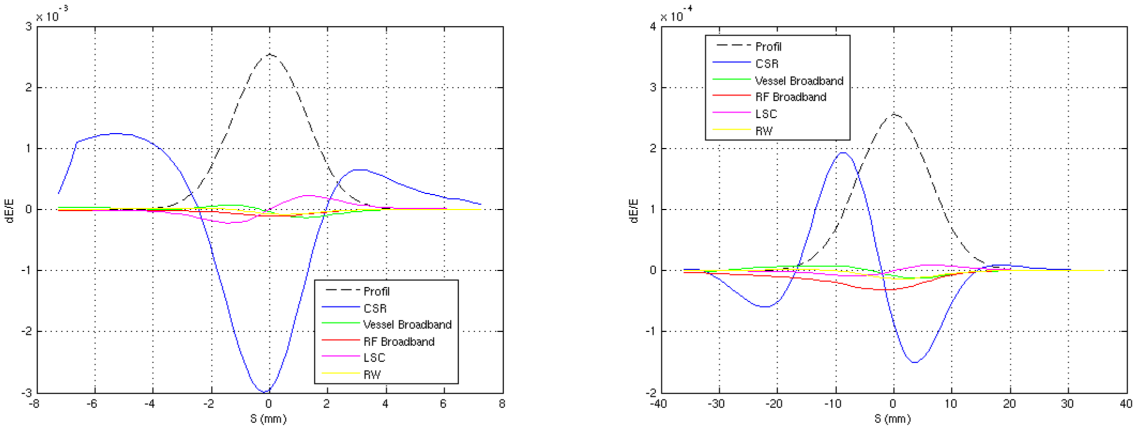

Figure 14 : Wake field distortions along a 1 nC Gaussian bunch at 50 MeV for a bunch length of 4 ps (left) and 20 ps (right).

In the hierarchy of strength, the dominant wake is clearly the CSR effect. The shielding has no effect at 4 ps and only partial at 20 ps r.m.s. bunch length. The CSR shielding configuration is not favourable with a short radius (0.352 m) and a quite large vertical aperture in the dipoles (40 mm). At 4 ps r.m.s. length, the relative wakes distortion is very strong and reaches few 10^{-3}. They are reduced to 10^{-4} at 20 ps. The RW, LSC and vessel impedances are small thanks to a large beam pipe. Moreover only very few components as bpm, flanges etc ..., (and no tapers) are known to bring large wakes. In counter part, the RF cavity impedance may have a role. Based on this set of longitudinal wakes field, a simulation has been carried out in order to evaluate some threshold instabilities in the short range domain. The 2D longitudinal simulations are done as follow:

1. Track over turns a collection of macro particles with a starting distribution (i.e. : Gaussian) including sine wave RF pass and linear ring pass. Apply at each turn the previous set of wakefields (energy kick) over the bunch density histogram.
2. Start with a quite long bunch length and progressively (adiabatically) apply an artificial damping to shorten it. Observe the bunch behaviour.

The results are plotted in fig.15. The ring settings present a momentum compaction of 0.015 and a RF voltage of 300 kV at 500 MHz. With 1 nC charge at 50 MeV, the bunch behaviour exhibits three different cases depending on the r.m.s. bunch length:

1. For r.m.s. lengths longer than 40 ps, the collective effect does not affect noticeably the longitudinal behaviour. The r.m.s. sizes are still equivalent to the zero current line.
2. For r.m.s. lengths between 20 to 40 ps, the length tends to lengthen under the collective effect but the emittance is kept stable without noticeable enlargement. The 1 nC bunch is stable and profiles slightly differ from the initial low charge density.

3. For r.m.s. lengths shorter than 20 ps, the behaviour becomes clearly unstable. It exhibits oscillations in the Length-Energy spread chart in parallel with large emittance increase.

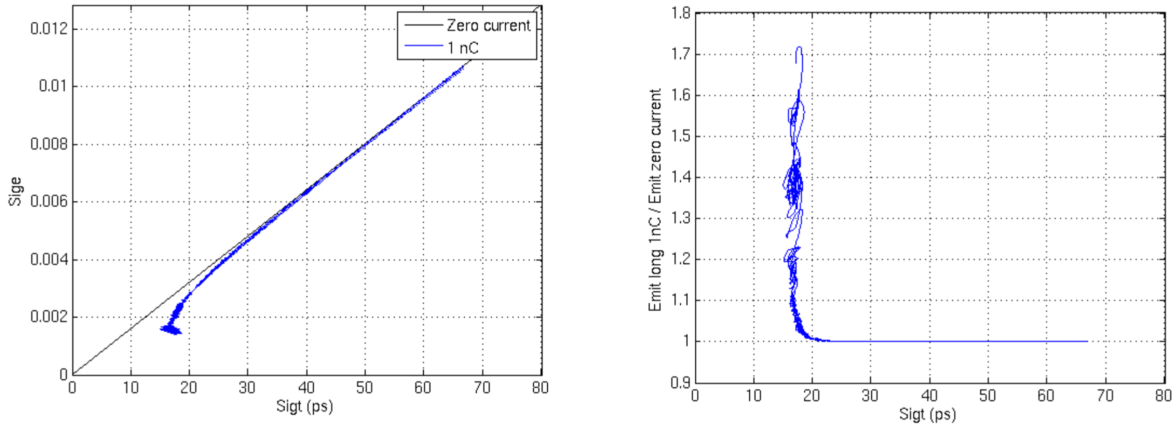

Figure 15 : Left: Bunch relative energy spread versus bunch length. Right: Relative longitudinal emittance versus bunch length.

Summarizing, to prevent from short range longitudinal instabilities with 1 nC at 50 MeV, it is advised to have a bunch length longer than 20 ps rms. Long range or multibunch instabilities are not addressed here.

4.5.8] Injection matching

The difficulty with direct on axes injection operation is the high sensibility to every kind of mismatch of the injected bunches. It is true for the six mean positions of the 6D phase space and for the 21 associated r.m.s. dimensions. While in the transverse plane, a standard dedicated transfer line optic can fit the beta functions at the injection point of the ring (see § 4.4) a special attention has to be done for the longitudinal case.

Regardless to any kind of collective effect, the relation between the relative energy spread σ_E and the bunch length σ_s in a ring is given by:

$$4.1)\quad \sigma_E = \sqrt{\frac{k_{ring} V_{RF}}{r_{56} E}}\sigma_s , \qquad k_{ring} = \frac{2\pi\ f_{ring}}{c} , \qquad r_{56} = \alpha \times Circonference$$

with V_{rf} the voltage, f_{ring} the RF frequency, E the energy, c the light speed and α the ring momentum compaction factor from the one turn matrix.

Neglecting space charge forces in the linac, the relative energy spread is directly given by the RF voltage curvature at null phase (max acceleration):

$$4.2)\quad \sigma_E = \frac{k_{linac}^2}{\sqrt{2}}\sigma_s^2 , \qquad k_{linac} = \frac{2\pi f_{linac}}{c}$$

With a 3 GHz linac frequency, the relative energy spread increases rapidly and quadratically with the bunch length. With 4 ps r.m.s. and 3 GHz, the energy spread is already about 0.5 % at the exit of the linac. There are two ways to match both sizes (fig.16):

1. Reduce the ring momentum compaction toward very low alpha values with the inconvenient of transverse position instability induced by inherent RF phase-energy jitter
2. Reduce the linac pulse length towards ultra short bunches with strong limitation in charge due to high electron density and possible emittance degradation

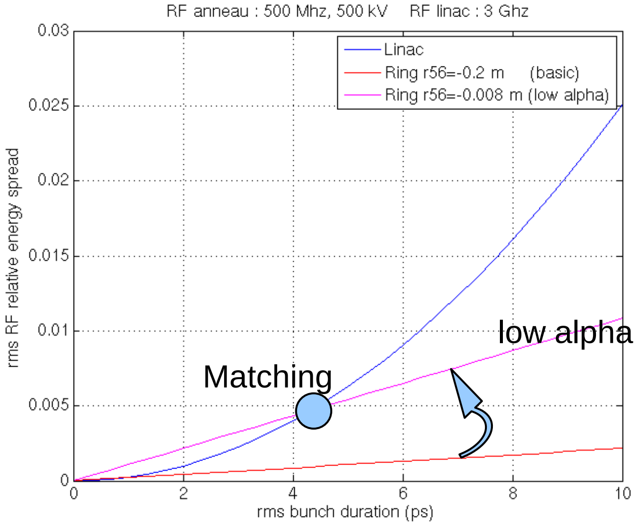

Figure 16 : Relative energy spread versus bunch length out of the linac and in the ring for both nominal and a low alpha configuration.

To overcome this difficulty, and to lengthen the bunches to reduce the instability risks, some longitudinal beam manipulations are necessary between the exit of the linac and the ring injection point. By means of a chicane and linac phasing (off crest acceleration) we are able to lengthen the bunches. The induced energy chirp has to be removed downstream by mean of a low voltage RF cavity added after the chicane (RF redresser) and phased on maximum slope (no acceleration).

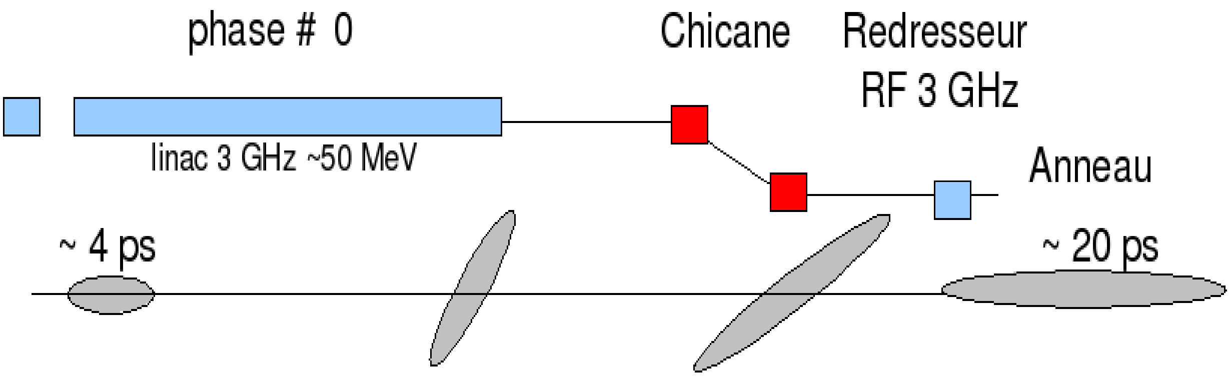

Figure 17 : Sketch of beam manipulation for longitudinal injection matching

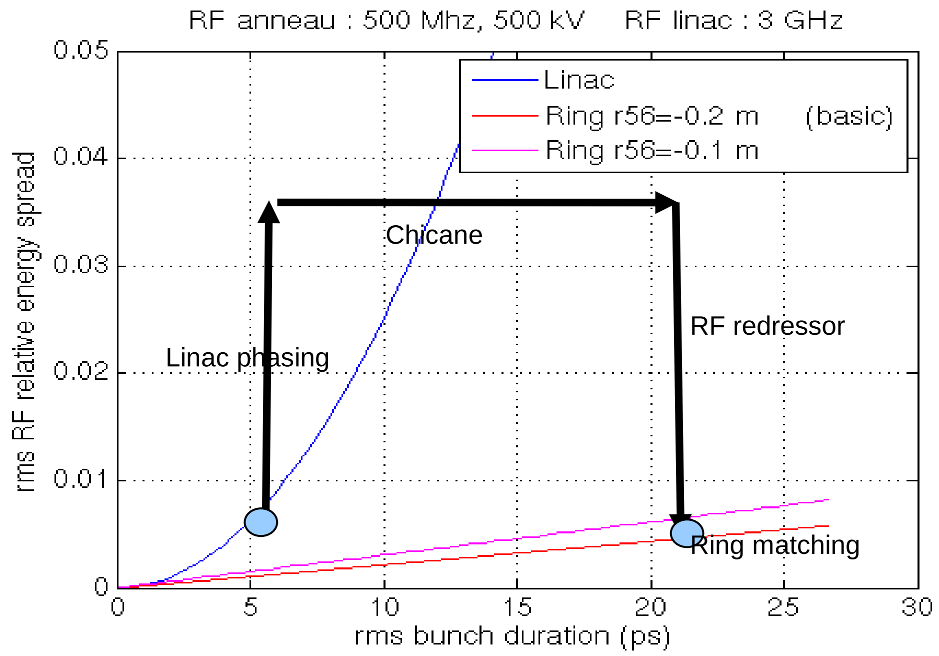

Figure 18: Chart of beam manipulation in the relative energy spread versus beam length space

The set of relations to solve (up to second order) between the linac phase and bunch length, chicane compression factor r_{56}, RF redresser phase and voltage, and ring parameters are given by:

$$\sin \varphi_{linac} = \frac{\left(\frac{\sigma_{ring}}{\sigma_{linac}} - 1 \right)}{k_{redresseur} \; r_{56\mathrm{chic}}}$$

4.3) $V_{redresseur} = \frac{Ek_{linac} \sin \varphi_{linac}}{k_{redresseur}} \frac{\sigma_{linac}}{\sigma_{ring}}$, $k = \frac{2\pi f}{c}$, $r_{56\mathrm{ring}} = \alpha_{ring} \times Circonference$

$$V_{ring} = \frac{k_{linac}^{4} \cos^{2} \varphi_{linac} \; r_{56\mathrm{ring}}}{2\mathrm{k}_{ring}} \frac{\sigma_{linac}^{6}}{\sigma_{ring}^{4}}$$

A possible solution that lengthen the electron pulse from 5 to about 20 ps with the nominal momentum compaction of the ring (0.015 or r_{56}=-0.22m) is listed in the table 6.

Linac	50 MeV	3 GHz	phase = -6°
Chicane	Compression factor r_{56} = -0.3 m		
RF redressor	2 MV	3 GHz	phase = 90°
Ring	300 kV	500 MHz	r_{56}=-0.22m

Table 6 : Linac and transfer line parameters for ring beam matching

With 6° phase off crest shift, the energy loss is small in the linac. At the entrance of the ring, the longitudinal r.m.s. sizes of 20 ps and the 0.3% relative energy spread match the ring configuration at zero current. The longitudinal phase space along the transfer line as well as the length profiles are plotted in fig.19 a,b.

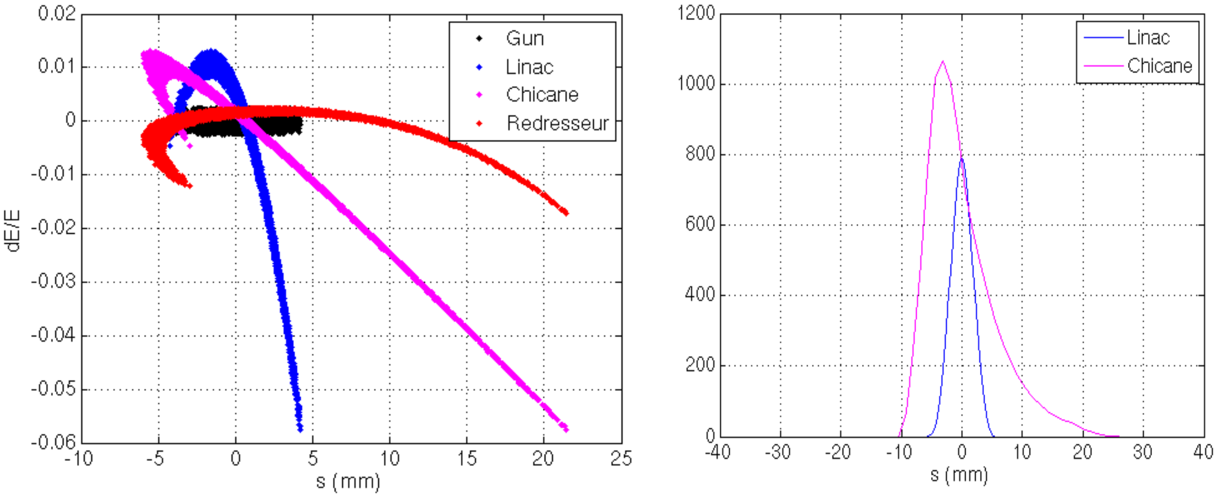

Figure 19a,b : a: Longitudinal phase space (length vs E-spread) along the transfer line. b: Bunch current profile.

In order to validate this matching process together with the presence of longitudinal collective effects, a 6D tracking simulations has been carried out on the first 0.5 ms (about 10.000 turns) after ring injection. The simulations follow the same scheme than the 2D case except that the lattice is now subdivided in ~200 steps per turns. At each step, depending on the concerned wakefields, an energy kick distribution is applied to the bunch. The ring settings are a momentum compaction of 0.015 and a RF voltage of 300 kV at 500 MHz. The transverse dynamic includes sextupoles tuned for zero chromaticities. The main results are plotted in the following figures.

In fig.20 the densities histogram, as well as the longitudinal phase spaces respectively at injection and 10.000 turns later, are presented. It mainly exhibits a fast mixing from initial curved shape toward quasi elliptical symmetry provided by the non-linear collective effects. Beside the density profile tends to be symmetric and Gaussian-like.

In fig.21 the r.m.s. emittances, as well as bunch length and relative energy spread all along the 10.000 turns, are plotted. The two transverse emittances remain unaffected while the longitudinal one is slightly increased by about 20 % in the very first turns. It is induced by a remaining profile mismatch due the apparent collective voltage already pointed out. In addition, the bunch length and energy spread exhibit a residual dipolar oscillation. These simulations confirm that it is possible to inject a 1 nC 20 ps bunch length at 50 MeV without prohibitive emittance deteriorations from transfer line beam manipulation with respect to short range longitudinal instabilities.

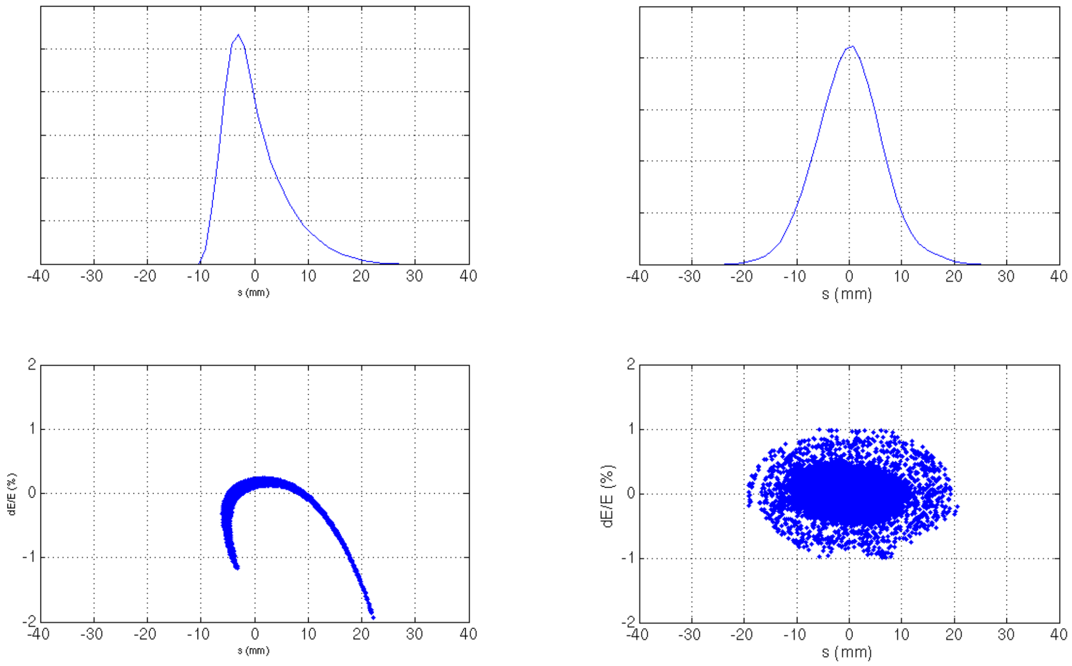

Figure 20 : Longitudinal bunch density (up) and phase space (down) at injection (left) and after 10.000 turns or 0.5 r.m.s. (right).

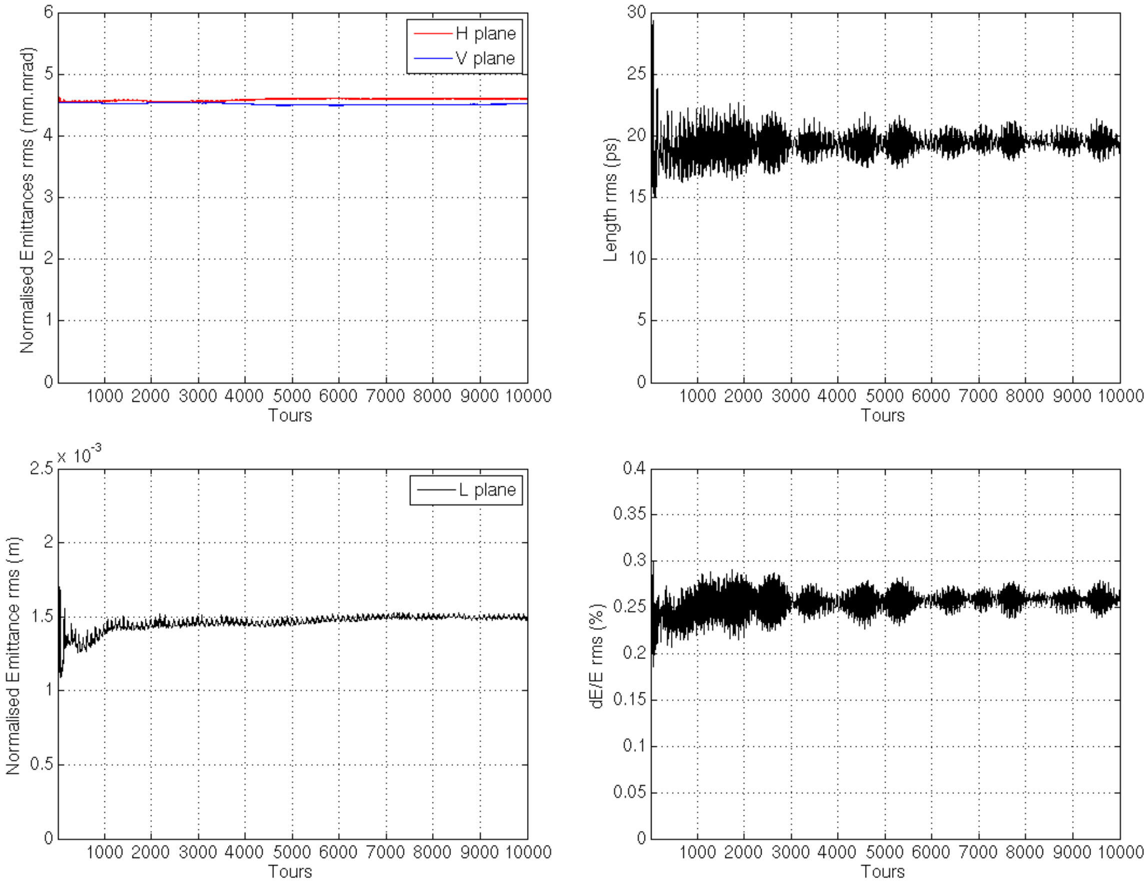

Figure 21 : R.m.s. normalized emittances (left) and rms bunch length and relative energy spread versus turns (right)

Appendix 1

Detailed element list of the ring lattice

Element	Length(mm)	Element	Length(mm)
Straight section	600	Straight section	100
HorizontalBPM	-	Quadripole	150
VerticalBPM	-	Straight section	70
Quadripole	150	Sextupole	60
Straight section	200	Straight section	70
Quadripole	150	Quadripole	150
Horizontal Steerer	-	Straight section	200
Verticall Steerer	-	Horizontal Steerer	-
Straight section	200	Verticall Steerer	-
Dipole	276	Quadripole	150
HorizontalBPM	-	Straight section	50
VerticalBPM	-	Sextupole	60
Straight section	120	Straight section	120
Sextupole	60	HorizontalBPM	-
Straight section	50	VerticalBPM	-
Quadripole	150	Dipole	276
Straight section	100	Straight section	100

Table 7 : description of the elements of a quarter of the ring.

Appendix 2

Modelisation of the 500 MHz ELETTRA type RF cavity with Gdfidl [14]. The corresponding longitudinal impedance and broadband wakes fitted model are also plotted.

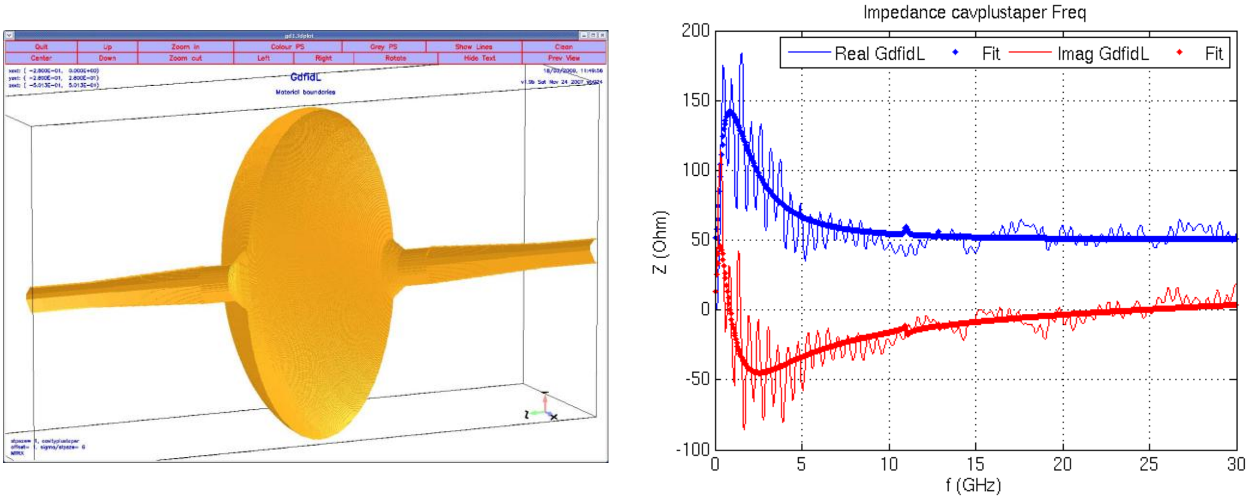

Figure 22 : Left: Sketch of the cavity cell. Right: longitudinal impedance and broadband wakes models.

	Broadband model			*RL model*	
	R	*Q*	*F*	*R*	*L*
500 MHz RF	92 Ohm	0,38	0,87 GHz	50 Ohm	0,0565 nH

Table 8 : Broadband (Resistance, Quality and frequency) and RL (Resistance and inductance) data model of cavity longitudinal impedance

The two following plots present the longitudinal impedances (and fitted broadband models) for SOLEIL BPM and flanges as example.

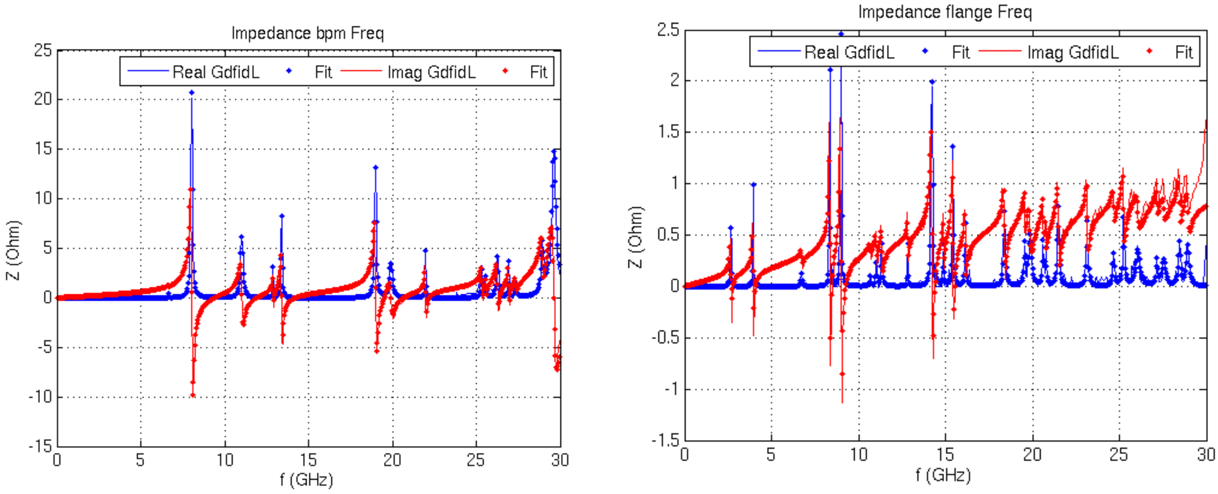

Figure 23 : Left : Sketch of the cavity cell. Right: longitudinal impedance and broadband wakes models.

4.5.9] Impact of Compton back scattering on the longitudinal and the transverse dynamics of the electron beam

In absence of Compton scattering, Synchrotron Radiation (SR) excites and damps longitudinal and transverse oscillations leading to equilibrium. The excitation originates in the random character of the photon emission that takes place in the dipoles, while the damping is provided by the restoration of the lost energy entailed by the radiation. When the electron beam interacts with a laser beam and produces X-rays by Compton Back Scattering (CBS), this electron beam-laser interaction also generates an excitation and a damping in analogy with the synchrotron radiation effects.
Let us also recall that, from a general point of view, the damping times of the various oscillation modes are given (within a factor two) by the time it would take for an electron to loose all its energy.

Longitudinal energy oscillations. We assume that E_0, the electron energy, is 50 MeV (see table 9 which resumes the parameters). Let ΔE be the energy loss due to the synchrotron radiation and ΔE_l the energy loss due to the Compton interaction, and $\tau_{rs} = E_0 T_0 / \Delta E$ and $\tau_l = E_0 T_0 / \Delta E_l$ being their respective damping times. If one of the two effects is negligible in respect to the other then the beam damping time will correspond to the one of the predominant (either SR or CBS). At the beginning of a ring refill, the energy loss due to the CBS is given by:

4.4) $$\Delta E_l = \frac{F_c T_0 \langle E_c \rangle}{N_e},$$

where F_c is the initial X-ray production rate, T_o is the period of the collisions between the electron bunch and the laser pulse, E_c is the mean value of the scattered photons' energy, and N_e is the number of electrons in the bunch. In our case, it turns out that the energy losses per turn are comparable for CBS and SR. Thus τ_{rs} et τ_l are comparable. The global damping time τ whose value is 0.6s results from the combined effects and is given by the relation $1/\tau = (1/\tau_{rs}) + (1/\tau_l)$. Concerning the SR excitation process or the CBS one, their strength is proportional to the mean square of the energy losses accompanying each event (photon emission or back-scattering). This quantity is considerably larger in the CBS case. The excitation of energy fluctuations is totally dominated in ThomX by the CBS process. Then, the energy spread within the electron bunch increases rapidly, the bunch lengthens and the flux decreases as illustrated by fig.24.

The equilibrium value of the energy spread resulting from both effects is about 1.4 % once it is stabilized by damping.

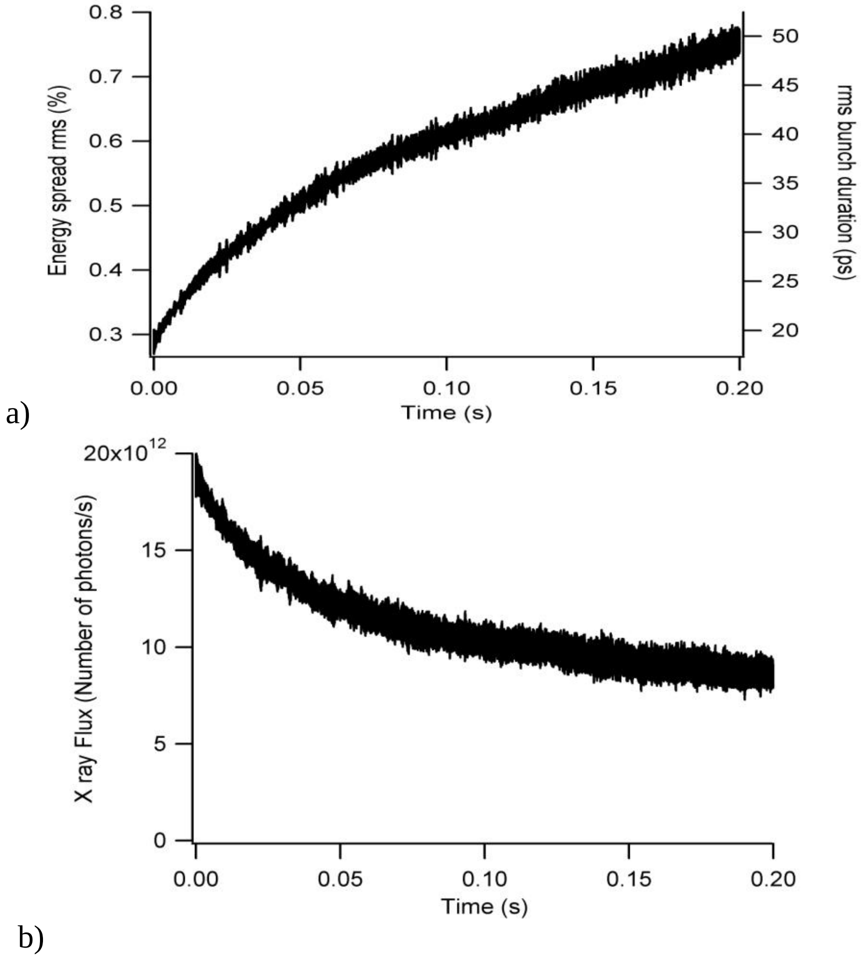

Figure 24 : Dynamics of the longitudinal/energy oscillations in presence of CBS and SR. The calculation does not take into account IBS and Touschek effects. a) Bunch length and energy spread, b) X-ray production rate versus time.

Obviously the energy losses due to CBS will be compensated by the RF cavity as well as those due to SR, and the synchronous phase of the cavity is obtained by taking both effects into account.

Electrons characteristics		
N_e	Number of electrons / bunch	$6.25\ 10^9$
σ_{xe}, σ_{ze}	Rms transverse size	70 μm
σ_{te}	Rms longitudinal size	6 mm / 20 ps
α_{el}	Angle between electron bunch trajectory and laser one	0.035 rad / 2°
Laser characteristics		
N_l	Number of photons/pulse	$1.6\ 10^{17}$
σ_{xl}, σ_{zl}	Rms transverse size	40 μm
σ_{tl}	Rms longitudinal size	1.5 mm / 1 ps
λ_l	Wavelength	1.06 μm
Compton Back Scattering (CBS) radiation characteristics		
σ_{th}	Thomson cross section	$6.66\ 10^{-29}$ m²
F_c	Initial flux	$1.2\ 10^{13}$ photons /s
ΔE_l	Energy loss per electron and per turn	2.3 eV
E_x	Maximum/Mean energy of CBS radiation	50/25 keV
T_0	Period	48 ns
τ_{xcbs}	Transverse damping time	2.1s
τ_{scbs}	Longitudinal damping time	1.1s
σ_{ecbs}	Energy spread	1.8%
ε_{xcbs}	Normalized emittance	$6.9\ 10^{-8}$
Synchrotron Radiation (SR) characteristics		
ΔE_0	Energy loss per electron and per turn	1.6 eV
E_{rs}	Critical energy of SR radiation	0.8 eV
τ_{xrs}	Transverse damping time	3.1 s
τ_{srs}	Longitudinal damping time	1.5s
σ_{ers}	Energy spread	$7\ 10^{-5}$
ε_{xrs}	Normalized emittance	$1.5\ 10^{-9}$
Equilibrium values of both SR and CBS		
τ_x	Transverse damping time	1.2s
τ_s	Longitudinal damping time	0.6 s
σ_e	Energy spread	1.4 %
ε_x	Normalized emittance	$6.5\ 10^{-8}$

Table 9 : SR and CBS characteristics in the ThomX ring.

Transverse oscillations. The transverse motion of the electrons is also affected by the CBS. As in the SR case, the normalized transverse emittance due to CBS is damped to its steady state value [15]

4.5) $\varepsilon_c = \frac{3}{10}\frac{\lambda_c}{\lambda_L}\beta^*_{x,z}$, where λ_c is the Compton wavelength of the electron (~2.43 10^{-12} m) and β^* is the beta function value at the interaction point (we assume a round beam). Since β^* is assumed to be low in order to maximize the X-ray production rate, the normalized emittance would be 7 10^{-8} π m rad (which is lower than the emittance of the beam produced by the linac: 4 10^{-6} π rad m). Similarly to the case of the longitudinal motion, the contributions of the SR and of the CBS to the transverse oscillations damping are about the same. The important point to note here is that the excitation of transverse (i.e. betatron) oscillations by the CBS is comparatively quite weak because the recoil effects due to each process take place at the interaction point where the dispersion function is close to zero.

It follows, from the above description of the impact of the Compton back scattering process on the ring dynamics, that the injection of a fresh bunch must be made every 20-50 ms in order to maintain a high level of the X-ray generation.

4.5.10] Touschek effect

The Touschek effect [16] originates in collisions between two particles that belong to the same bunch in a storage ring. Such a collision produces an energy transfer between the radial motion (betatron oscillations) and the longitudinal one (synchrotron oscillations). If the particles' final energies differ too much from the ring nominal energy, these particles are lost. Thus this effect puts a limit to the beam lifetime; it depends in a sensitive way on the particle density within the stored bunch and on the ring energy acceptance.

The ThomX storage ring presents some peculiarities regarding this effect: (i) the stored bunches have a high particle density; (ii) the energy acceptance of the ring is large since the momentum compaction factor is small (close to 1.5 %) and the RF peak voltage is 300 kV; (iii) the beams are stored for very short periods of time (about 20 ms), therefore the Touschek effect becomes harmful only if it restricts the beam lifetime to less than a second. In fact, in the case at hand, the relevant figure is not the loss rate but the (higher) rate at which internal collisions lead to such a large increase of the synchrotron oscillation amplitudes that, afterwards, the particles hardly participate in the X-ray production (because, most of the time, these particles miss the photon bunch in the interaction region).

Let dN/dt be the number of electrons that receive, each second, an energy kick such that they undergo synchrotron oscillations with a 8 mm amplitude or more (i.e. larger than the *total* interaction region length). This 8 mm amplitude corresponds to an energy deviation $\Delta E/E$ close to .4%. An analytic calculation shows that the time constant τ defined by $\tau^{-1}= (1/N)$ dN/dt which characterizes this process is on the order of a minute right after injection, and then becomes longer because the bunch density decreases. Thus the Touschek effect is not expected to introduce a significant limitation to the X-ray yield.

4.5.11] Intra-beam scattering

Multiple Touschek effect, also called intra-beam scattering (IBS) [17] contributes to the excitation of betatron and synchrotron oscillations. It consists in Coulomb scattering events that occur at a high rate but with comparatively large impact parameters, i.e. impact parameters which are on the order of the mean distance between a stored electron and its closest neighbours. Each one of these collisions produces a small energy-momentum transfer. In most cases the mean statistical effect of these transfers are only significant in the $\{\Delta E, \Delta s\}$ synchrotron space. An analytic calculation of this effect can be performed but the energy excitation that it produces must be combined with the ones originating in the synchrotron radiation and the X-ray production. Furthermore these excitations lengthen the stored e^- bunch; as a consequence the mean bunch number density decreases and so does the IBS rate during a storage cycle. Fig.25 shows the relative importance of these three sources of excitation of the synchrotron oscillations, while fig.26 shows the increase of $<\Delta E>$, the r.m.s. of the energy spread, during a 20 ms storage cycle.

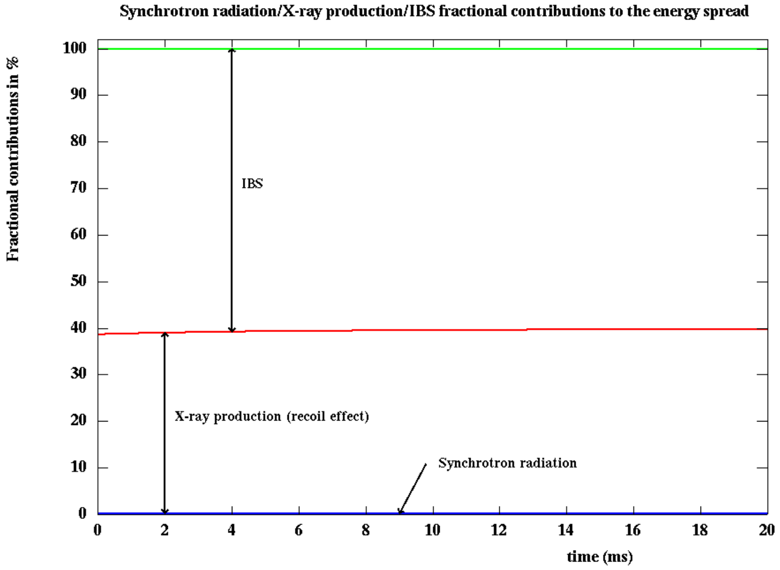

Figure 25 : The blue line shows the fractional contribution (in %) of the synchrotron radiation (RS) to the excitation of synchrotron oscillations in the Thom-X ring. The red line shows the sum of the RS and the X-production contributions to this excitation, while the Intra-beam scattering (IBS) contribution is the complement to 100 % above the red line.

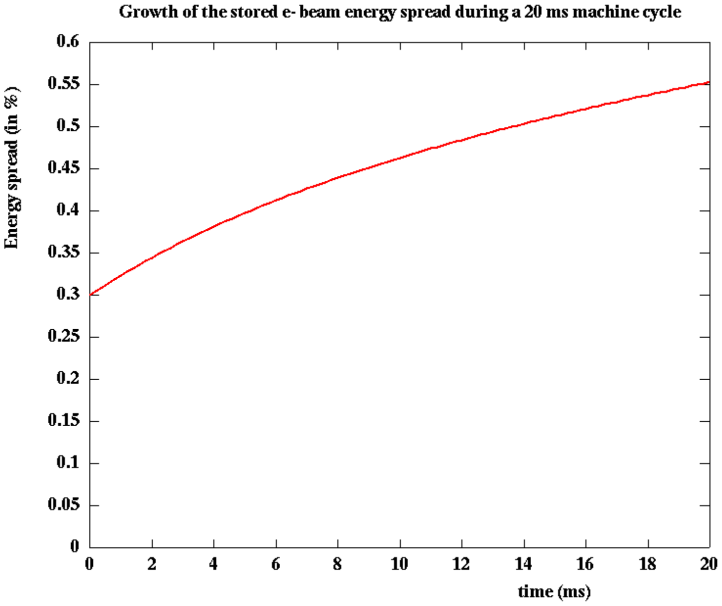

Figure 26 : Growth of the energy spread ($\Delta E/E_0$ in %) during a 20 ms machine cycle.

4.5.12] Vacuum effect

Coulomb scattering of the electrons on residual gas molecules induces an increase of the emittance of the circulating beam. This is proportional to the average value of the ring beta functions and to the partial pressure. Moreover it varies as the square of the atomic number of the considered molecule, and it is inversely proportional to the energy of electrons. With a low energy of 50 MeV, it is therefore essential to keep a low pressure to minimize the increase of the emittance. Fig.27 shows the growth of the transverse emittance in a period of 20 ms (50Hz injection) for the Nitrogen and Hydrogen cases respectively. Considering the Nitrogen at a pressure 8 10^{-7} Pa, the emittance increases by 4 10^{-6} mrad, which means that the original value, being 5 10^{-6} mrad, is doubled. To minimize this emittance growth due to coulomb diffusion on the residual gas, a pressure lower than 3 10^{-7} Pa must be maintained.

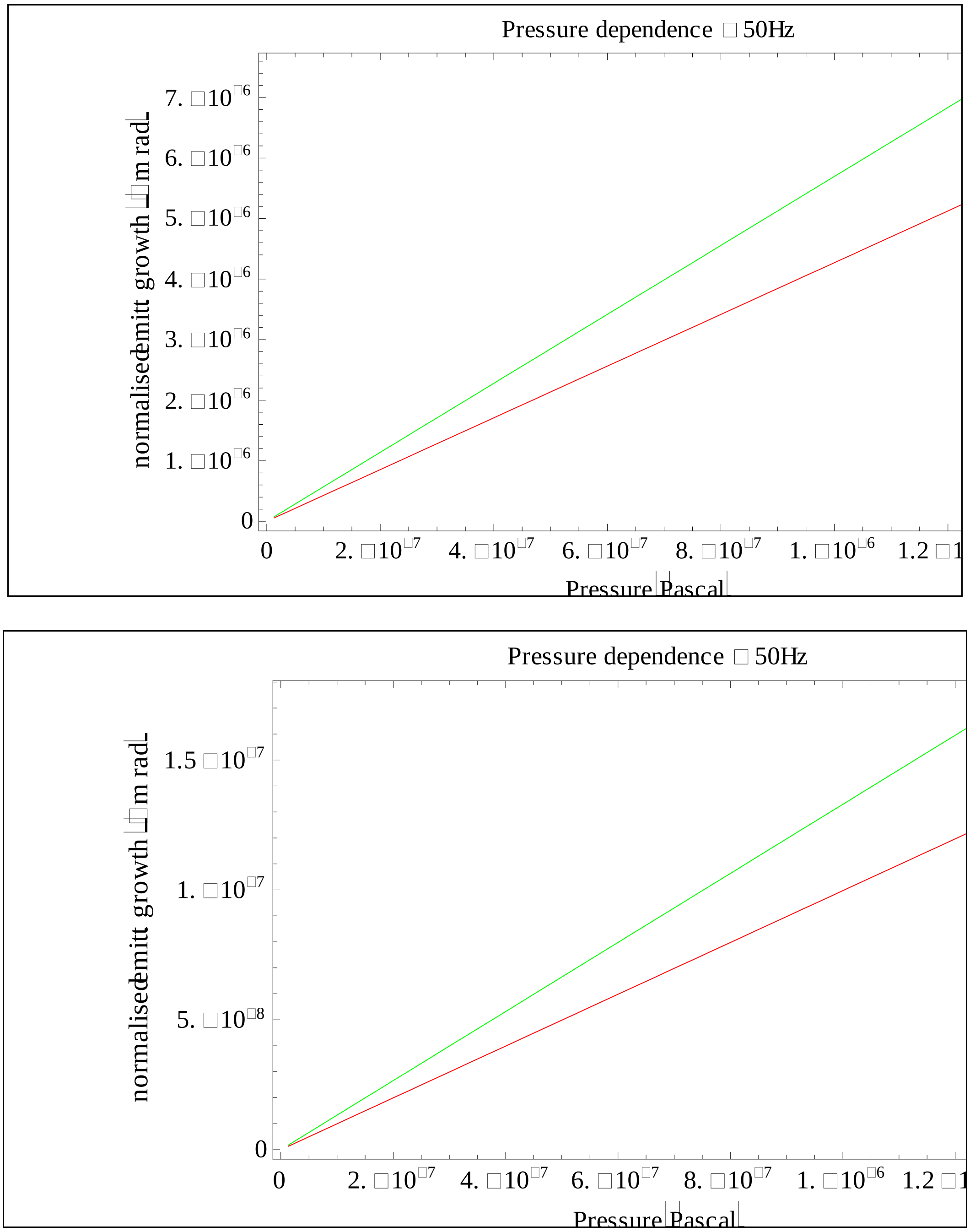

Figure 27 : Normalized emittance increase versus pressure considering a) Nitrogen, b) Hydrogen

4.5.13] Ions instabilities

The beam-ion instability [18,19,20] is due to the ionization of the molecules of the residual gas. Ions can then be trapped by the electron beam potential. This instability can strongly damage the quality of the electron beam inducing for example: coherent instability, tune shifts

and broadening, reduction of the beam lifetime (pressure increase). In a first step, we estimate here the coherent and incoherent tune.
The critical mass above which the ions are trapped is:

$$4.6)\quad A_{ion} = \frac{N_e L_0 r_p q_{ion}}{2\sigma_z(\sigma_x + \sigma_z)}$$

This critical mass in units of proton mass is in the order of the unity for the ThomX ring. This expression considered the most general case of the CO molecule, for which the ionization cross section is larger than others residual possible molecules. With such a critical mass, all ions can be trapped in our case.
The consequences on the stored beam depend on the neutralization factor η_{ion}, which represents the number of ions with respect to the number of stored particules. The accumulation point of the neutralizing ions is given by a number of ions equal to the number of stored particules then $\eta_{ion}=1$.
The electron beam is submitted to the electric field of the ion distribution. As a consequence the local quadrupole strength is modified inducing a coherent tune shift. It can be estimated with the following formulae [21]:

$$4.7)\quad \Delta\nu = \frac{r_e(2\pi R)\beta_{moy}}{2\gamma}\eta_{ion} d_e \qquad \text{with} \qquad d_e = \frac{n_e}{2\pi R\,\pi\sigma_x\sigma_y}$$

With r_e the classical radius of the electron, R the ring circumference, and σ_x the mean transverse size; β_{moy} the mean betatron function along the ring, γ the Lorentz factor and d_e the mean number of electrons per volume units. By considering β_{moy}=3m, σ_x=σ_x=0.6 mm and a fully neutralization (the worst case –> η_{ion}=1), the tune shift is 0.6, estimated from (4.7). There is also an incoherent effect (tune spread) due to the change of betatron frequency of single particle, which is estimated twice the coherent tune shift, 1.2 with fully neutralization [22]. With clearing electrodes, or leaving a period for ion clearing between different injections, the neutralization factor can be reduced to 1% [18, 19]. Then, the tune shift is 0.006 with a tune spread of 0.012.
The ion effect on tune shifts can be consequent on the beam and must be refining in the future. Nevertheless, as already said, the number of ions can be reduced (reducing the neutralization factor to a few percent) leaving time between the extraction and the reinjection of the beam or by introducing clearing electrodes [20,22,23]. Moreover the ions instabilities can be cured by means of feedback already developed [19].

4.6] Equipments

4.6.1] Magnets

A design of the different magnets has been done using the RADIA code [24]. They can be improved in terms of size in view of saving cost, weight and radial space. The detailed pole shape as well as multipole components has to be further investigated with respect to the non linear beam dynamics. Their main characteristics are listed in the table 10:

	Field	***Current per coil***	***Gap / Radius***	***Iron length***	***Weigth***	***Cooled***
Dipole	0.5 T	8000 A turns	40 mm	300 mm	260 kG	yes
Quadrupole	3 T/m	360 A turns	50 mm	150 mm	60 kG	no
Sextupole	30 T/m^2	120 A turns	50 mm	60 mm	10 kG	no

Table 10 : Magnets main characteristics at 50 MeV

With 0.5 T magnetic field, the dipole deviation is of 45° at 50 MeV. The straight dipole is positioned at mid deviation in order to minimise the curved trajectory sagitta. The pole faces are rotated to 22.5° providing an effective 0° face to the electron entrance and exit trajectory. With gradients of dB/dx= 3 T/m and 0.5 d^{2}B/dx^2=30 T/m in quadrupoles and sextupoles, the current densities in the coil are about 0.8 A/mm^2 in both cases. With a maximum current density of 1.5 A/mm^2 to prevent from cooling, their maximum gradients allow the machine to be operated up to 80 MeV.

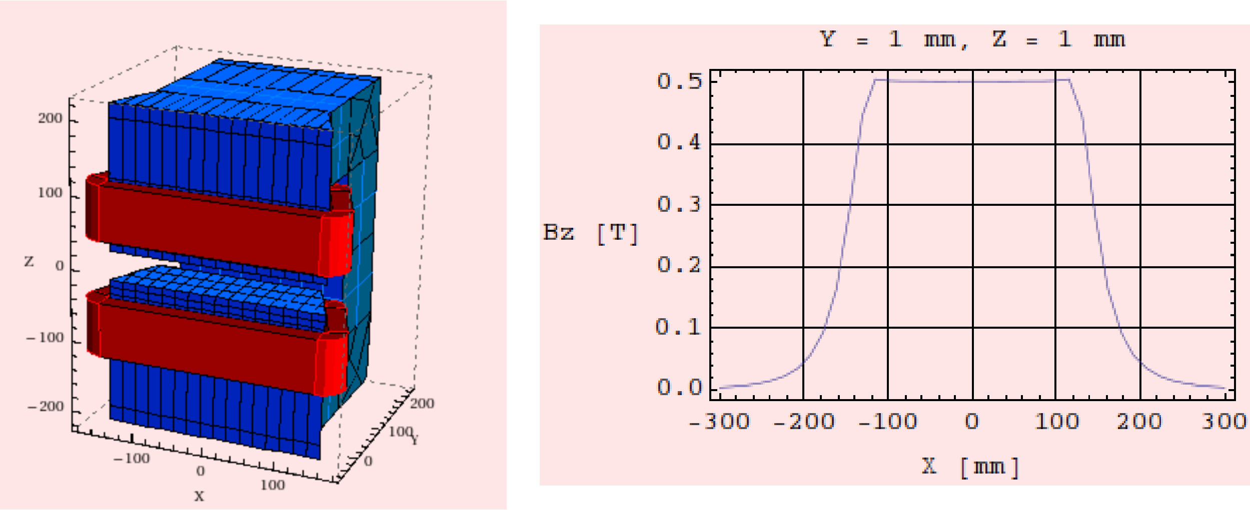

Figure 28 : Dipole yoke and longitudinal field profile

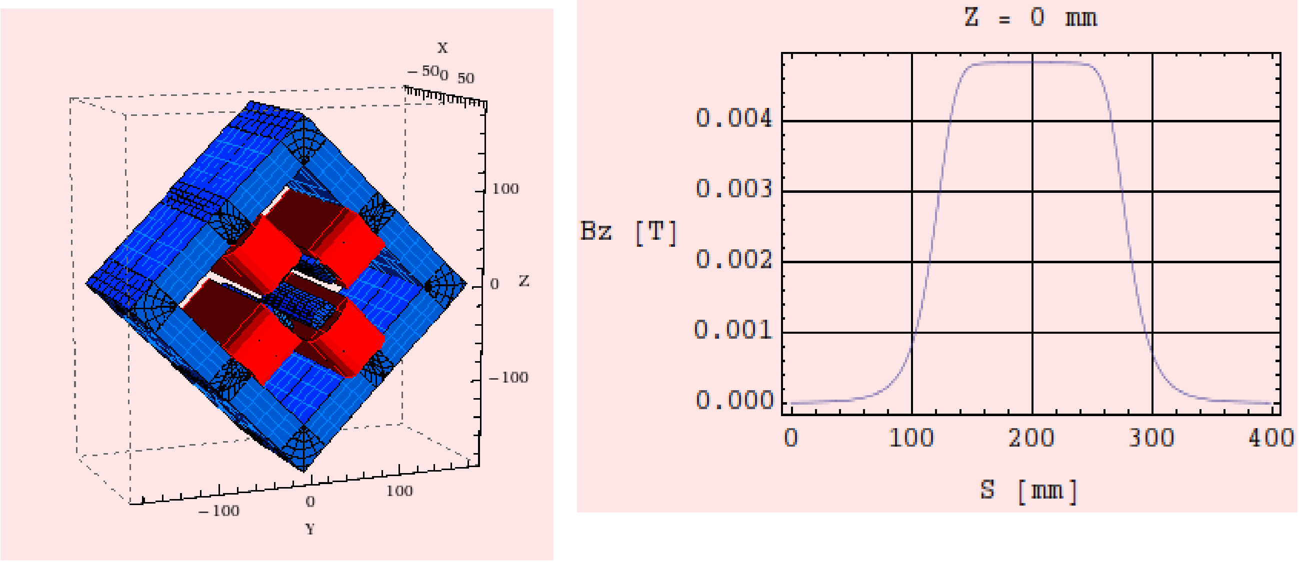

Figure 29 : Quadrupole yoke and longitudinal field profile

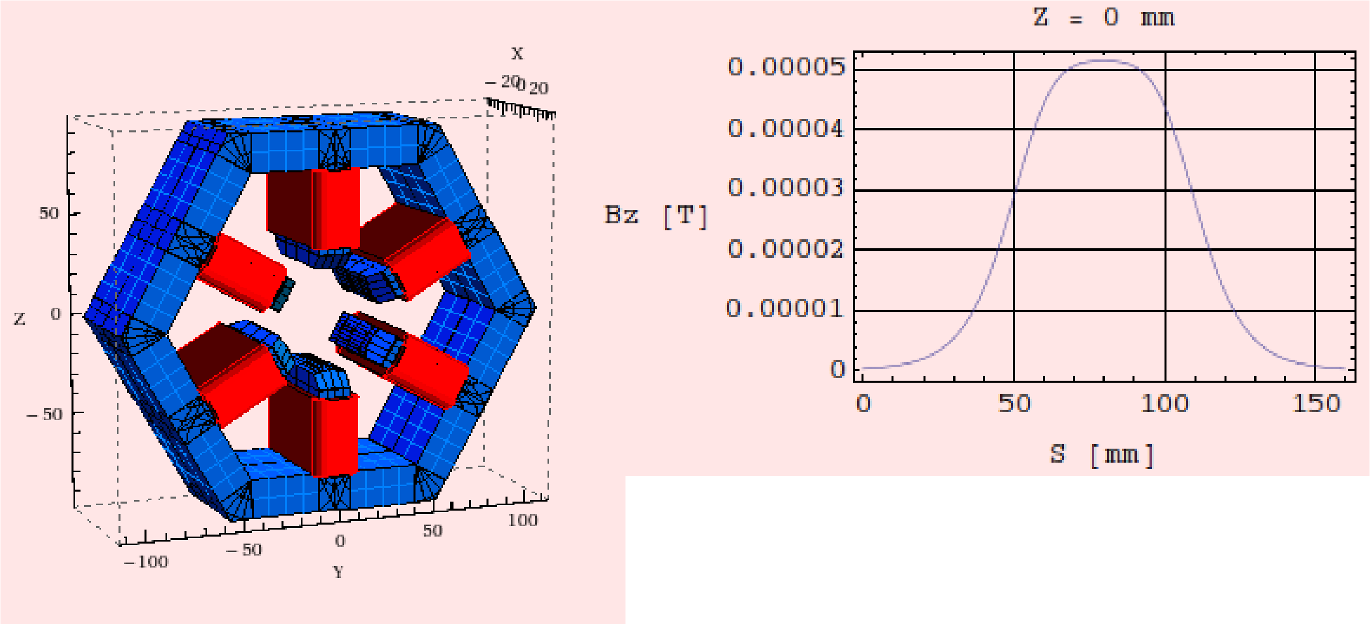

Figure 30 : Sextupole yoke and longitudinal field profile

The following graph presents the configuration of the 2 m Fabry-Perot optical cavity inserted in the short section between the two dipoles as well as the adjacent sextupoles and quadrupoles. The next figure plots the vertical magnetic field along the optical cavity. A residual field of 0.017 T is present at the interaction point. At 50 MeV, the large 10 m radius should not affect the X-ray flux. In counter part, this fringe field affects the real dispersion function, in particular at the IP, not included in the previous linear optics design. It will have to be investigated.

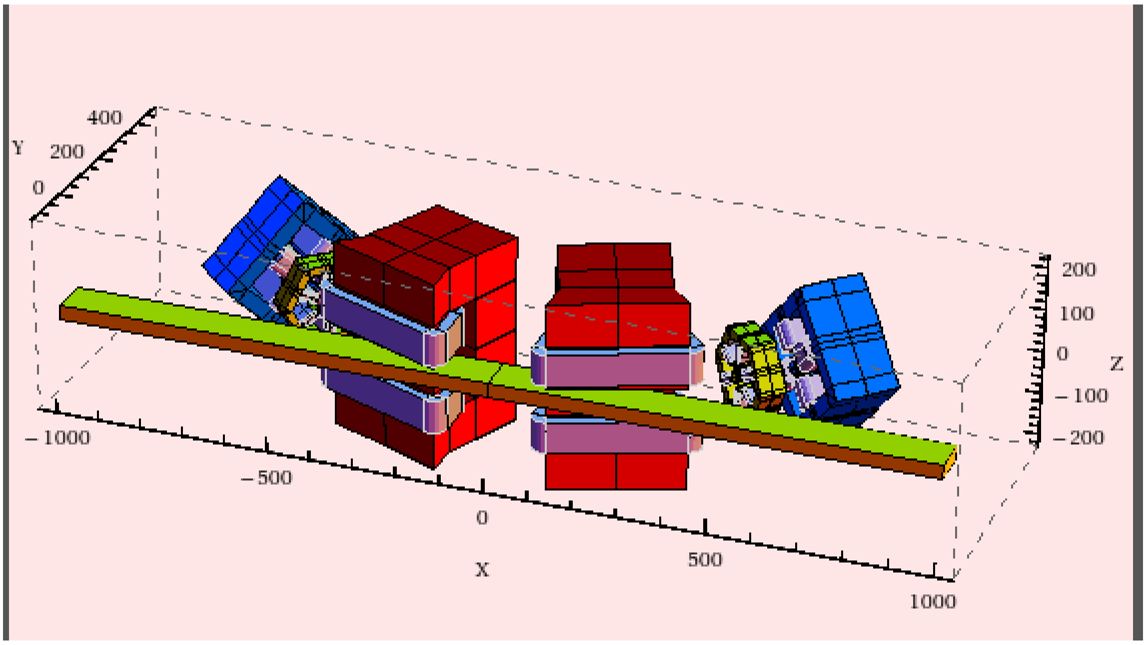

Figure 31 : 2 m Optical cavity and adjacent magnets

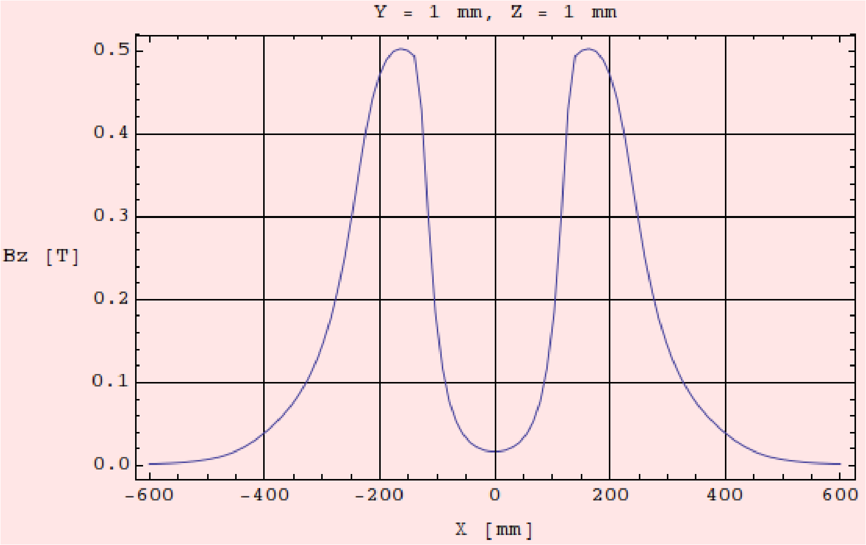

Figure 32 : Vertical magnetic field along the optical cavity and at IP

4.6.1.1] Power Supplies

In order to specify the ring power supplies characteristics, the coil dimensions and magnet numbers are listed in the following tables:

	Pole size	***Turn length***	***Coil size***	***Coil Surf***
Dipole	300 x 80 mm	760 mm	75 x 25 mm	1875 mm^2
Quadrupole	150 x 30 mm	360 mm	30 x 15 mm	150 mm^2
Sextupole	60 x 16 mm	152 mm	20 x 4 mm	80 mm^2

Table 11 : Magnet coil characteristics

	Total number	***Families***	***Nb per families***	***Coils in series***
Dipole	8	1	8	16
Quadrupole	24	6	4	16
Sextupole	12	2	8 & 4	48 & 24

Table 12 : Magnet families and coils in series

Neglecting the cabling connexions, the resistivity of each power load are simply given, with sigma the copper resistivity (σ=1.810^{-8} Ohm.m), by the relation:

4.8) $$R = \frac{(Nb\ \ Coils\ )\times(Nb\ \ Turns\ )\times(Turns\ \ \ Length\ )}{Conductor\ \ \ \ Surface}\times\sigma$$

For dipoles, with 75 turns per coils and a hollow conductor section of 18 mm^2 (5x5 mm & hollow radius 1.5 mm Luvata), the total resistivity is 0.9 Ohm. The nominal maximum current is then 106 A at 50 MeV.

For quadrupoles, with 48 turns per coils and a conductor section of 8.737 mm^2 (5x1.8 mm Von Roll metplat), the total resistivity is 0.7 Ohm. The nominal maximum current is then 3 A at 50 MeV.

For sextupoles, with 20 turns per coils and a conductor section of 3.785 mm^2 (4x1 mm Von Roll metplat), the total resistivity are respectively 0.7 and 0.35 Ohm. The nominal maximum current is then 3 A at 50 MeV.

	DC Supply Nb	***Load***	***Voltage / Current***	***Stability***
Dipole	1	0.9 Ohm	90 V / 100 A	10^{-5}
Quadrupole	6	0.7 Ohm	4.2 V / 6 A	10^{-5}
Sextupole	*2*	*0.7 - 0.35 Ohm*	*4.2 – 2.1 V / 6 A*	10^{-5}

Table 13 : List and characteristic of the ring power supplies

4.6.2] Pulsed magnetic systems for the ring injection

The beam generated by the LINAC has to be injected in a 1.2m long straight section of the storage ring. The quadrupole magnet located just before this straight section imposes an angle of 8 degrees between the transfer line and the ring straight section.

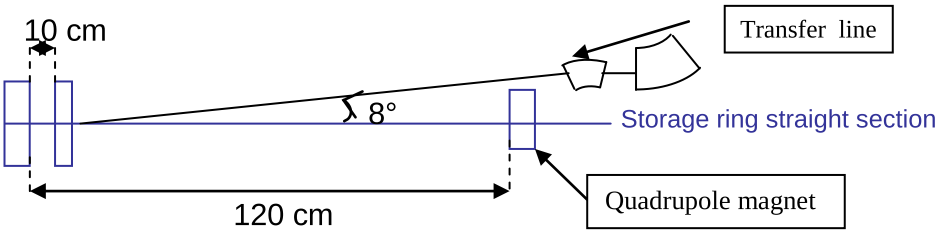

As the needed deviation is important, it has to be realized using two pulsed magnets: a thin septum magnet, insuring the most part of the deviation, and a very fast kicker which puts the injected beam on axis.

- *The septum magnet and its pulsed power supply*

The main constraints are to realize a large deviation (6.5-7 degrees), leading the injected beam very close to the ring straight section axis, without significant disturbance on the stored beam. So the magnet mechanics needs to preserve the stored beam vacuum chamber geometry, and its magnetic stray field has to be very small into the stored beam volume.
An eddy current septum magnet, installed in vacuum, will be convenient for the application. The effective magnet thickness can be 3 mm, allowing a small distance between stored and injected beam position at the output of the septum magnet yoke. An internal chamber, joined to the magnet yoke, extends the ring vacuum chamber and preserves the impedance continuity. The deviated beam penetrates by a small hole in this internal chamber.

Such a septum magnet is very asymmetric: it is driven by a copper loop around the steel yoke. In order to contain the magnetic flux, the whole yoke is full enveloped in a copper box, which drives the eddy current. On the side regarding the stored beam path, the copper box has a reduced thickness, constituting the thin septum. Such a structure is very efficient to avoid important magnetic stray field outside the magnet gap, because of the electric shielding provided by the eddy current circulating in the copper septum. With a full sine excitation, the residual stray field is reduced in duration and amplitude. An additional magnetic shielding will be realized with a 0.5 mm thick screen of Mumetal surrounding the internal chamber (stored beam path). With such a solution, combining eddy current shielding, full sine pulses excitation and high permeability magnetic material, the stray field can be reduced to a very low level (a few 10 ppm of the main pulsed field). [25]

Taking a septum opening of H x V = 18 x 15mm (for the injected beam) and an active length of 300mm, it results on these parameters for its pulsed power supply:

	Deviation	Field integral	Field	Peak current	Charging voltage
Septum	7 ° (= 122.2 mrad)	20.4 mT.m	68 mT	810 A	96.2 V

- The fast kicker magnet and its pulsed power supply

The kicker magnetic system is mainly dimensioned by:

- the physical opening necessary for the stored beam : H x V = 60 x 40 mm,
- the short revolution period of the storage ring : T_{rev} = 50 ns,
- the very short length of the injected bunch : σ_t = 25 ps (in 1σ RMS).

Two solutions of kicker were evaluated: a magnetic kicker out vacuum and an electromagnetic stripline in vacuum, taking an active length of 500mm for both.
The kicker magnet is built around a ceramic vacuum chamber which increases the magnet gap. The kicker magnet is supplied by a pulsing circuit delivering half sine pulses [26].
The in-vacuum stripline could permit to adjust the electrode aperture to the needed gap and benefit of both the electric and the magnetic fields provided by its travelling wave behaviour [27],[28].
Because of the short revolution period of the ring, 50 ns, the field pulses duration has to be less than 50ns and with very fast rising and falling times. Hopefully, with such a very short bunch length (25 ps r.m.s.), there is no need to have significant flat top on the pulses.
Both solutions were evaluated with the aim to keep the supply high voltage below ~25 kV, in order to be able to use solid state switches and standard cables and components, with a good safety margin. It results that either solution can be chosen, but the strip line option permits less deviation: <1° with a 25 kV pulse voltage. It is also a more delicate technique and the transverse field homogeneity is medium. In the case of a magnetic kicker, it is possible to get ≥1.5° with 25 kV pulse voltage (449 A peak) choosing a half sine excitation of 50ns duration, which is convenient for very short bunch length.
So we retain this solution of a magnetic kicker, of window-frame transverse geometry, including a 6mm thick ceramic vacuum chamber. The ceramic chamber has to be coated inside by a thin deposit of Titanium, in order to insure the electric continuity from flange to flange. This deposit thickness has been calculated so as to not deteriorate the fast pulse shape and to avoid thermal rising due to the mirror current [29].

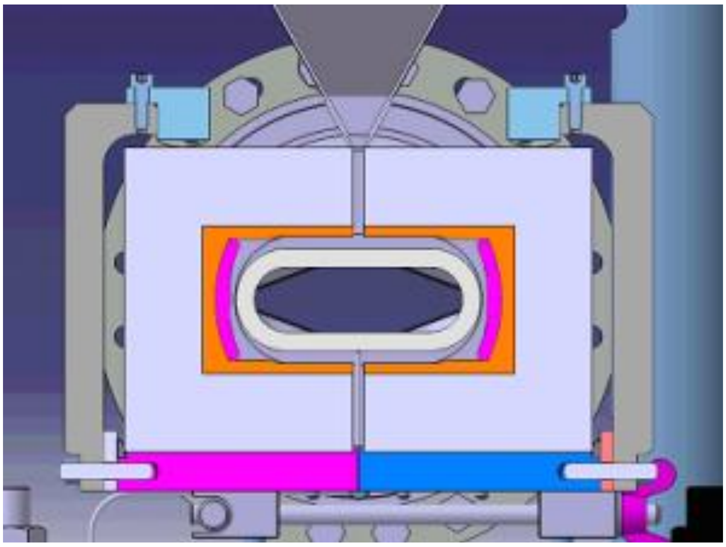

The resulting parameters are:

	Deviation	Field integral	Field	Peak current	Charging voltage	Coating thickness
Kicker	1.5 ° (26.2 mrad)	4.4 mT.m	8.7 mT	449 A	24 kV	20-40 nm

4.6.3] Storage ring RF system

The selection of 500 MHz as RF frequency leads to a quite good compromise in terms of cavity fundamental and high order mode (HOM) impedances, space requirements as well as the availability of RF power sources and other components. The required accelerating voltage of 500 kV can be provided using only one 500 MHz single cell cavity, powered with about 35 kW. As shown in the following, the choice of the cavity design is mainly dictated by the need for a strong damping of the HOM impedances.

4.6.3.1] HOM impedance thresholds for coupled bunch mode instability (CBMI)

When exciting a mode in resonance, the growth rate of the CBMI is approximately given by :

$(1/\tau)_l = I_b\ \alpha\ f_m\ R_l / (2\ Q_s\ E/e)$ for the longitudinal case;
$(1/\tau)_t = I_b\ \beta_t\ f_o\ R_t / (2\ E/e)$ for the transverse case;
f_m : HOM resonant frequency;
R_l and R_t : longitudinal (Ω) and transverse (Ω/m) HOM impedances;
$Q_s = f_s / f_o$: synchrotron tune, f_s and f_o being the synchrotron and revolution frequencies;
β_t : beta-function at the cavity location;
α : momentum compaction factor;
I_b : average beam current;
E/e : beam energy (eV).

Assuming typical cavity HOM impedances ($R_l . f_m =$ 0.1 to 1 MΩ .GHz ; R_t = 1 to 10 MΩ/m) and the machine parameters listed in table 14, one finds that the instability growth times are around 10 µs in both longitudinal and transverse cases.

Circumference : C	14.5 m	Max current : I_b	20.83 mA
Electron energy : E	50 MeV	Synchrotron freq. : f_s	498.7 kHz
Momentum compaction : α	0.015	RMS bunch length : σ_s	14 ps
RF freq. : f_{RF}	500 MHz	β-function : $\beta_{x,z}$	1 m, 4 m
Revolution freq. : f_o	20.7 MHz	Relative energy spread : σ_E / E	7.0 10^{-5}
Harmonic number : h	24	Peak accelerating voltage :V_{RF}	500 kV

Table 14 : Main ThomX storage ring parameters.

In a low energy ring like ThomX, the natural damping is so weak (damping time ~ 1 s) that a stationary stable condition can never be reached during the beam storage time, which is as short as 20 ms. On the other hand, it is sufficient to maintain the instability growth time larger than the beam storage time such that to keep at tolerable level the effect on the beam. In order to meet this condition, very strong attenuation of the HOM impedances is required, typically by a factor around 10^4.

4.6.3.2] Cures to HOM driven CBMI

There are essentially two different ways of coping with such HOM impedances, either a strong de-Qing of the HOM resonances or a tuning of their frequencies away from the CBM spectral lines such that to prevent resonant excitation by the beam.

In practice, the HOM de-Qing is achieved by extracting and transferring the cavity HOM power towards external dissipative loads. In this way, it is difficult to reach attenuation factors higher than 10^2 -10^3 over a large frequency range and that requires the use of rather heavy and cumbersome equipment around the cavity (coaxial lines with coupling antennas or ferrite loaded waveguides). Two illustrations of this technique are shown in fig.33 and 34, the DAMPY cavity, designed at BESSY [30] and which will be used in ALBA [31] and the PEP II cavity, developed at LBNL [32].

Figure 33 : 500 MHz DAMPY cavity

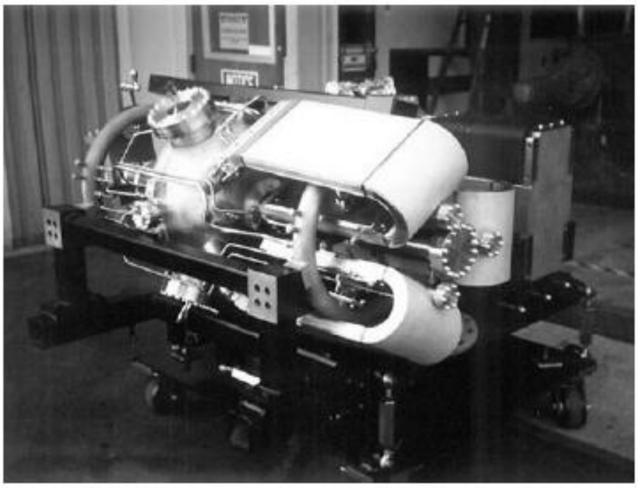

Figure 34 : 476 MHz PEP II cavity

The other method, which consists in controlling the HOM frequencies, is better suited to a small circumference machine like ThomX, where the CBM spectral lines spacing (~ 21 MHz) is very large as compared to the HOM bandwidth (BW of a few 10 kHz for Q_o of a few 10^4). As far as the HOM density is not too high and that they can easily be tuned far enough from the CBM spectral lines ($\delta f \gg f_m / Q_o$), it should be possible to reduce their effective impedances ("seen" by the beam) down to tolerable levels : $R_{eff} \approx R_s / (2\, Q_o\, \delta f / f_m)^2 \ll R_s$.

We have started to investigate the achievable performance by applying this technique to an ELETTRA type cavity [33], slightly modified with a cut-off pipe diameter reduced from 100 mm down to 60 mm, which fits our vacuum chamber. Fig.35 shows the shape of this 500 MHz single cell cavity, which was used as a basis for our first investigations. As for the ELETTRA cavity, we assume that the HOM frequencies can be precisely controlled by proper setting of the cavity water cooling temperature while the fundamental frequency is recovered by means of a mechanism which longitudinally deforms the cavity. Besides, a movable plunger tuner, also called HOM Frequency Shifter (HFS), located on the cavity equator, provides an additional degree of freedom [34].

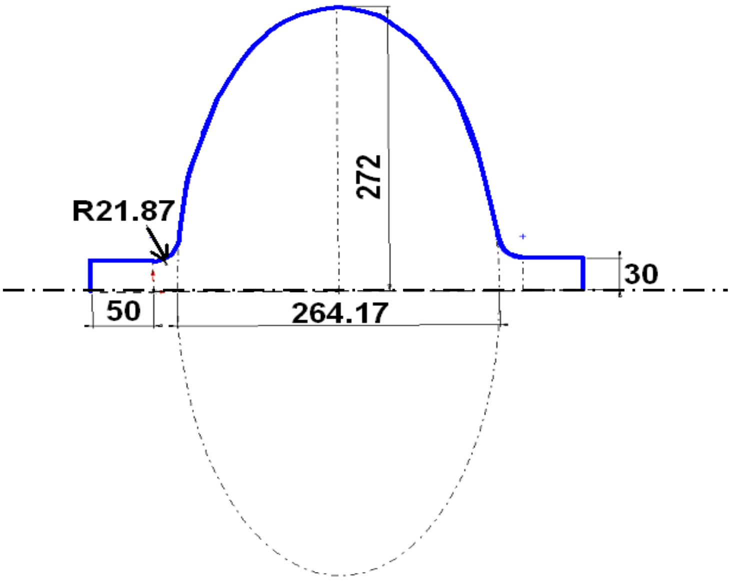

Figure 35 : shape of the 500 MHz ELETTRA-type cavity with a cut-off pipe diameter of 60 mm.

In tables 15 a,b, are listed the fundamental and HOM parameters of such a cavity, calculated with the 3D computer code GdfidL [35]. One finds 26 significant HOM (14 monopoles and 12 dipoles) with resonant frequencies lower than the cavity cut-off frequency. Figures 36 a,b represent the corresponding HOM spectra, $f_m . R_l(f)$ and $R_t(f)$, reported over a single base band of 20.8 MHz. The horizontal dashed line on the graph represents the impedance threshold corresponding to an instability growth time equal to 20 ms, the beam storage time. Although it remains somewhat critical, these preliminary results tend to confirm that it should be possible to find acceptable operating conditions, as far as the HOM frequencies can be shifted by a few MHz in combining temperature and HFS tuning.

a) Longitudinal modes	f_m [MHz]	Q_o	R_s / Q_o [Ω]	R_s [kΩ]	Δf_m (T) [MHz]	Δf_m (HFS) [MHz]
L0 (fundamental)	496,154	43618	84,2	3672,6	0.00	0.00
L1	958,759	47195	39,4	1859,5	0.45	-1.00
L2	1021,03	56190	1,49	83,723	0.78	3.69
L3	1401,65	49766	7,35	365,78	1.73	0.21
L4	1526,17	69033	8,9	614,39	1.33	0.86
L5	1544,86	62475	14,75	921,51	2.36	7.21
L6	1867,73	52320	1,39	72,72	1.43	-0.92
L7	1960,65	78048	2,43	189,66	2.54	1.43
L8	2054,53	62759	0,54	33,89	2.60	2.26
L9	2092,26	83828	12	1005,9	4.77	6.67
L10	2341,29	54311	1,42	77,121	> 4	?
L11	2421,29	90457	0,48	43,419	> 4	?
L12	2506,78	89378	1,91	170,71	> 4	?
L13	2550,00	60158	0,65	39,103	> 4	?
L14	2656,70	97745	9,05	884,59	> 4	?

b) Transverse modes	f_m [MHz]	Q_o	$R_{s\perp}$ / Q_o * [Ω]	$R_{s\perp}$ ** [MΩ/m]	Δf_m (T) [MHz]	Δf_m (HFS) [MHz]
T1	737,01	50267	33,5	25,99	0.4	0.75
T2	746,06	52566	9,2	7,557	1.55	2.85
T3	1152,02	47196	26,4	30,06	0.49	-3.12
T4	1255,65	55386	5,1	7,428	0.68	7.25
T5	1302,49	71674	3,6	7,039	0.97	?
T6	1699,81	69325	10,3	25,42	1.88	?
T7	1736,50	91039	1,65	5,463	> 2	?
T8	1773,37	59409	3,2	7,061	> 2	?
T9	1836,17	77697	5,5	16,43	> 2	?
T10	2061,42	88484	5,9	22,54	> 2	?
T11	2224,75	99092	1,1	5,079	> 2	?
T12	2259,33	56641	1,3	3,484	> 2	?

Table 15 a,b : Main characteristics of the monopole (a) and dipole (b) modes, computed with GdfidL, for the elliptical cell with a cut-off pipe diameter of 60 mm; Δf_m (T) and Δf_m (HFS) are the effective temperature and HFS tuning ranges at constant fundamental frequency.

* $R_{s\perp}/Q_o = |V(r_{offset})|^2 / (2 (k . r_{offset})^2 . (2 \pi f_m) . U)$ [Ω],
where U is the electromagnetic energy stored in the cavity and $k = (2 \pi f_m) / c$ [m^{-1}].

** $R_{s\perp} = (R_{s\perp}/Q_o) . Q_o . k$ [Ω/m].

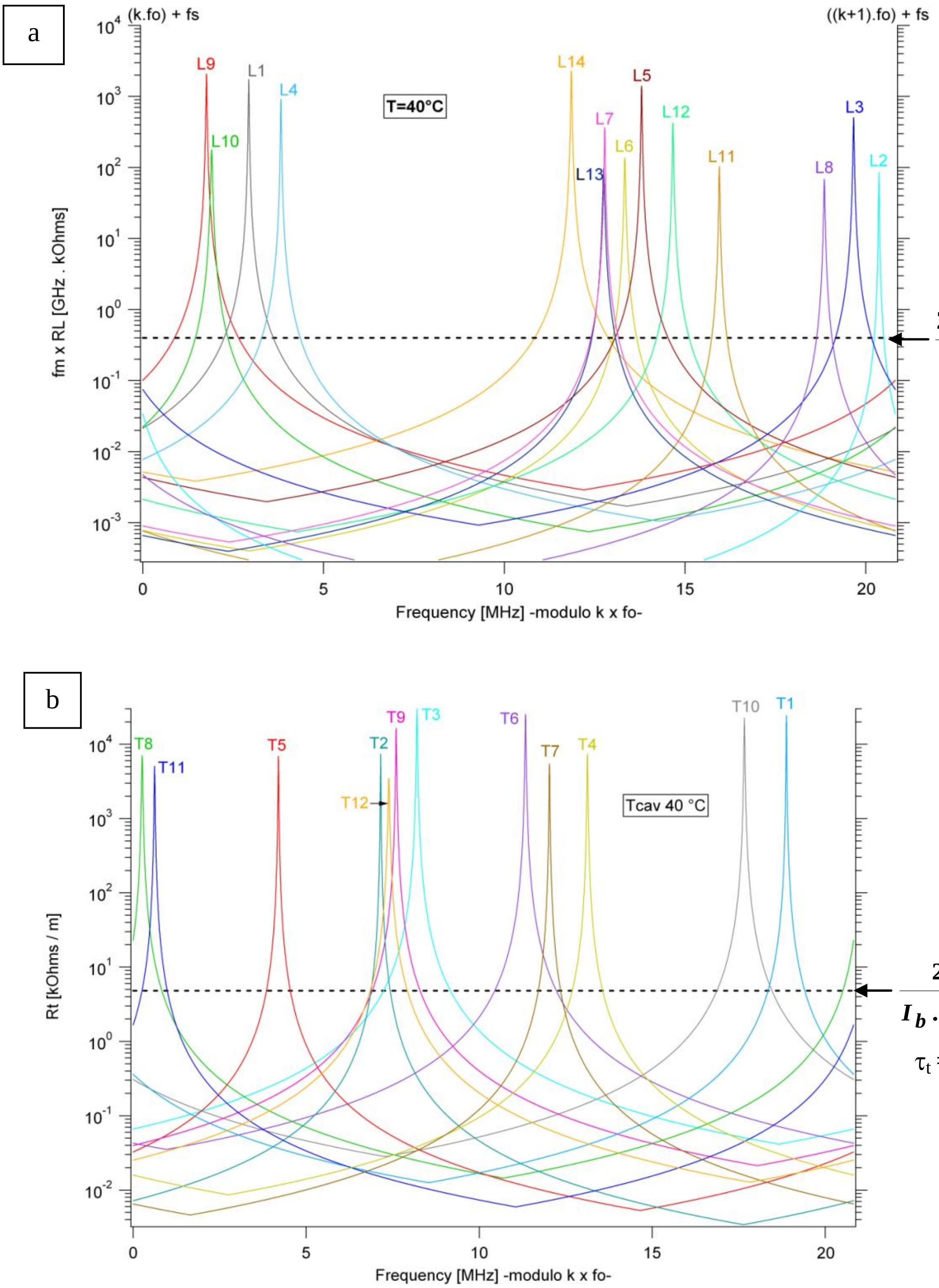

$$\frac{2Q_s E_o / e}{I_b .\alpha .\tau_l}$$

$\tau_L = 20$ ms

$$\frac{2E_o / e}{I_b . f_o .\beta_t .\tau_t}$$

$\tau_t = 20$ ms

Figure 36 a,b : longitudinal (a) and transverse (b) HOM spectra, reported over a single base band of 20.8 MHZ for the elliptical cell with cut-off pipe diameter of 60 mm.

Increasing the diameter of the cavity extremity pipes reduces the cut-off frequency and consequently the number of trapped HOM. This is illustrated in Figures 37a,b, which shows the HOM spectra for a similar elliptical cavity shape but with a cut-off pipe diameter of 100 mm. The number of significant HOM (tables 16a,b) has dropped down to 18 (9 monopoles and 9 dipoles), which should significantly facilitate the task. However, the impact of tapers was not considered in this preliminary study and it is mandatory to demonstrate that the impedances of the HOM propagating into the tapers are not critical. If they prove to be sufficiently damped, the choice of the actual ELETTRA cavity without modifications will be straightforward.

These conditions could be further improved, in a second stage, by providing additional damping, with the implementation of single bunch feedbacks and/or a 3rd harmonic Landau cavity.

a) Longitudinal modes	f_m [MHz]	Qo	R_s / Qo [Ω]	R_s [kΩ]	Δf_m (T) [MHz]	Δf_m (HFS) [MHz]
L0 (fundamental)	499.132	44164	76.5	3378,54	0.00	0.00
L1	958.618	48158	33.6	1618,11	0.37	-1.00
L2	1027.81	57861	0.36	20,8300	0.80	3.69
L3	1408.7	52562	2.20	115,636	1.74	0.21
L4	1515.28	69088	7.83	540,959	1.12	0.86
L5	1551.29	66375	8.50	564,188	2.40	7.21
L6	1869.12	55785	0.97	54,1114	1.42	-0.92
L7	1949.5	81752	0.08	6,54016	1.83	1.43
L8	2039.85	62729	0.86	53,9469	4.00	?
L9	2068.96	87300	5.30	462,690	4.45	6.67

b) Transverse modes	f_m [MHz]	Qo	$R_{s\perp}$ / Qo [Ω]	$R_{s\perp}$ [MΩ/m]	Δf_m (T) [MHz]	Δf_m (HFS) [MHz]
T1	728,458	52052	11.1	8,815	0.40	0.75
T2	734,55	49803	30.0	22,99	1.52	2.85
T3	1131,18	46047	22.6	24,65	0.64	-3.12
T4	1214,496	53972	9.60	13,18	2.00	7.25
T5	1636,985	64565	5.40	11,95	?	?
T6	1702,197	85862	2.20	6,734	?	?
T7	1723,526	88149	1.97	6,268	?	?
T8	1749,277	93715	1.77	6,077	?	?
T9	1769.55	60646	1.00	2,247	?	?

Table 16 a,b : Main characteristics of the monopole (a) and dipole (b) modes, computed with GdfidL, for the elliptical cell with a cut-off pipe diameter of 100 mm; Δf_m (T) and Δf_m (HFS) are the effective temperature and HFS tuning ranges at constant fundamental frequency.

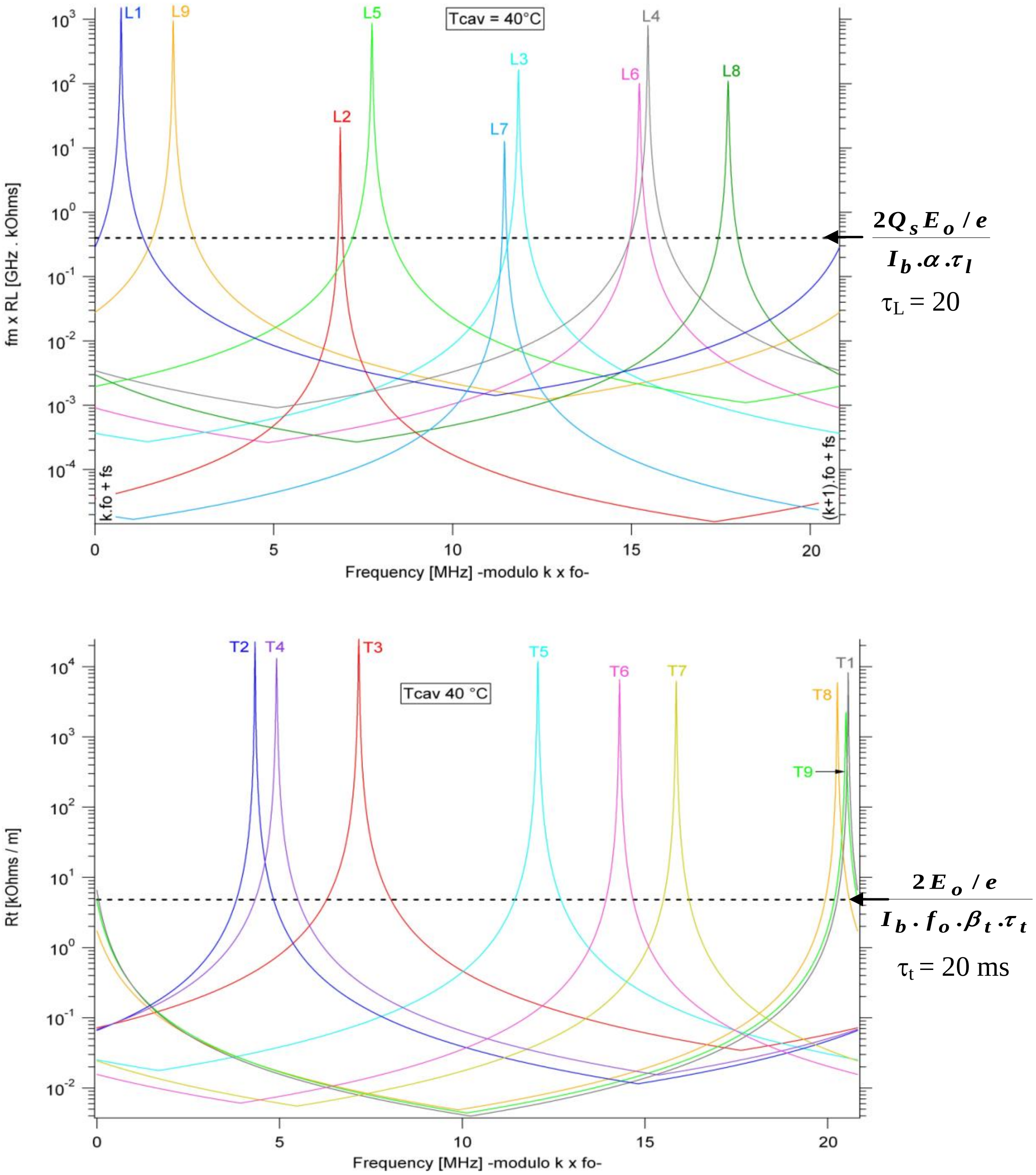

Figure 37 a,b : longitudinal (a) and transverse (b) HOM spectra, reported over a single base band of 20.8 MHZ for the elliptical cell with cut-off pipe diameter of 100 mm.

RF power source

A power of about 35 kW is required in order to generate the desired voltage of 500 kV in a single 500 MHz ELETTRA type cavity. For this frequency, there exists a wide choice of power sources, based on the vacuum tube (klystrons, IOTs, diacrodes) or solid state technologies. The low operating voltage and high modularity of the solid state version brings in significant advantages as compared to the vacuum tubes. The experience acquired at SOLEIL after few years of operation has largely demonstrated all the benefits of this technology. Fig.38 shows the 35 kW – 352 MHz solid state amplifier, used for the SOLEIL booster synchrotron and which consists in a combination of 147 modules of 330 W. This technology has been already extended to 500 MHz in the frame work of a SOLEIL-LNLS collaboration aimed at realising two 40 kW amplifiers for the LNLS storage ring.

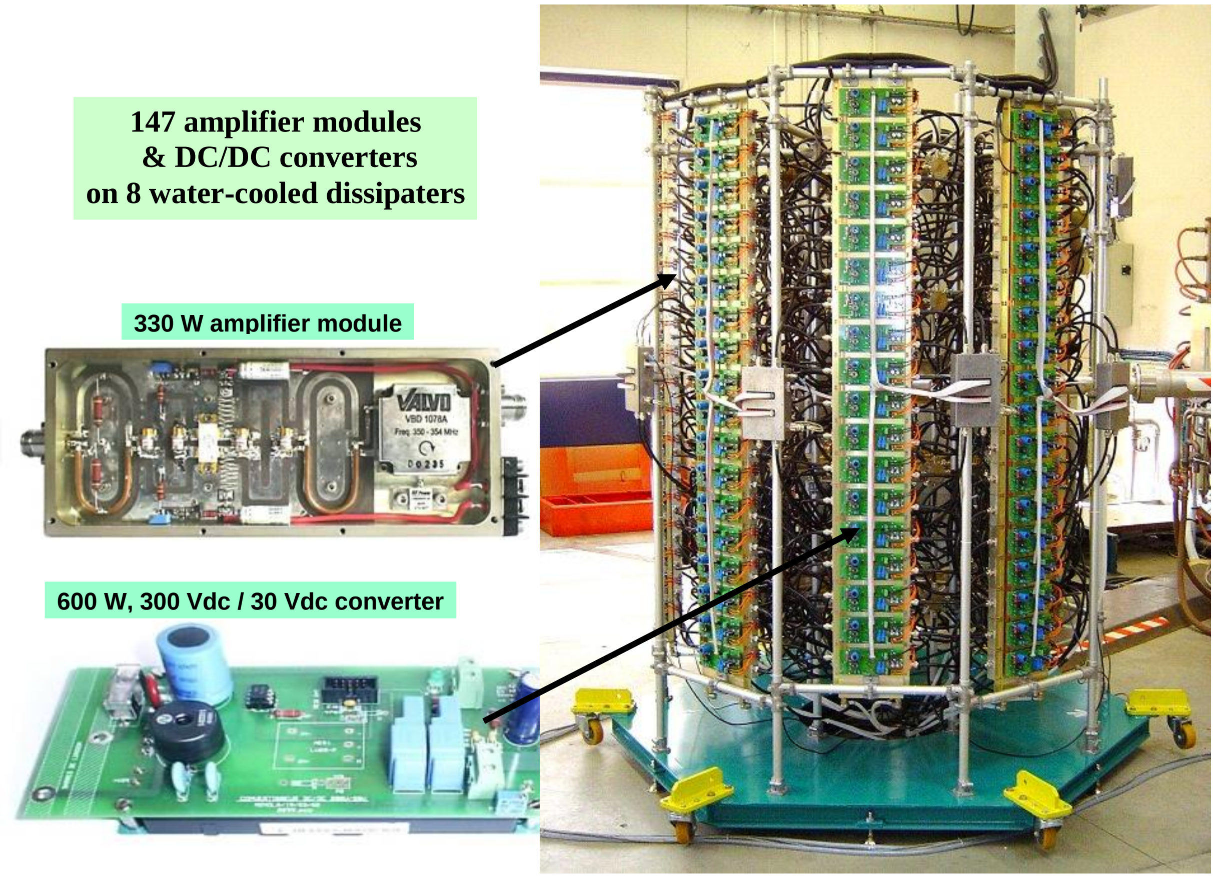

Figure 38 : 35 kW – 352 MHz solid state amplifier of the SOLEIL Booster

Conclusions

For the RF system of the ThomX storage ring, it is proposed to use one 500 MHz single cell cavity of the ELETTRA type. Maintaining at a tolerable level the CBMI driven by the cavity HOM is quite challenging. However, preliminary studies tend to demonstrate that it should be achievable with a proper control of the HOM frequencies, combining three different tuning means of the cavity : temperature, longitudinal elastic deformation and plunger.
In a second stage, the damping of the CBMI could be improved by implementing single bunch feedbacks and/or a 3rd harmonic Landau cavity.
In order to achieve the required accelerating voltage of 500 kV, the cavity can be powered with a solid state amplifier “SOLEIL-type”, able to deliver up to 40 kW of power.
The cavity voltage shall be controlled with typical stability of ± 0.1 % and ± 0.1° by means of conventional phase and amplitude loops (either analogue or digital) of few kHz bandwidths.
Les transitoires de phase à l’injection pourront être réduits à une fraction de degré grâce à une simple boucle de feedback RF direct.

4.6.4] Diagnostics and beam dump

4.6.4.1] Charge, current and life time

For the Linac and the transport line, beam charge monitors called ICT (Integrating Current Transformer) by its manufacturer (Bergoz Instrumentation), can measure the charge at a 50 Hz repetition rate.

For the Storage Ring, the best for accurate beam current and lifetime measurements would be a DCCT from Bergoz Instrumentation, which has a good absolute precision (1µA). It needs 30 to 40 cm of longitudinal space for its insulating gap associated to a short bellow, the toroid, and two flanges. An electrical shielding and a magnetic shielding are also necessary.

The electrically insulating gap can be made according to the Nelly Rouvière design [36] way, thanks to a high capacitance gap, the monitor presents a low impedance to the beam. The 10 kHz bandwidth with a rise time of about 16 µs, will allow to measure the life time in less than 20 ms.

A cheaper alternative would be to install an FCT (fast current transformer) connected to an oscilloscope that measures the bunch charge (integration of the pulse) at each turn. Apart from the cost, the advantage would be a slightly reduced longitudinal space (25 to 35 cm). However, with an FCT, it is necessary to distinguish each turn for a good accuracy, which implies a bandwidth of several hundred Megahertz. Then a high capacitance gap is not appropriate and the impedance to the beam is higher than with a DCCT.

4.6.4.2] Beam Position Monitors

Eight button type Beam Position Monitors (BPM) are foreseen on the Storage Ring. Ten millimetre diameter button electrodes should be appropriate for obtaining a 10 µm resolution on most of a 1-to-30 mA dynamic range.

The BPM impedance to the beam has to be checked after a first design is done. The two top electrodes will be mounted on a flange and the two bottom ones on another flange. In this way, the longitudinal space can be minimized to about 10 to 15 cm. Low-loss coaxial cables bring the electrode signals to the electronics, housed outside of the high radiation area. Due to the radiation levels expected in the Ring, the connectors on the BPM side of the cables must have their insulating material made of PEEK (PolyEtherEtherKeton), a radiation resistant material, instead of PTFE (Teflon).

The Libera electronics from Instrumentation Technologies working at 500 MHz (25th harmonique) will be adequate after 500 MHz narrow band filters have been introduced between BPM and electronics. This is to improve the button electrode signal level (factor ~25); otherwise, it would be too weak at the 20 MHz fundamental frequency.

Both the Linac and the transport line require a Beam Position Monitor (BPM). These BPMs are of the stripline type, ¼ wave coupler at 500 MHz. The Libera electronics, identical to that of the storage ring BPMs, is appropriate.

4.6.4.3] Bunch length measurements

In order to check the bunch length after the lengthening chicane, an insertable OTR (Optical Transition Radiation) screen is installed at the end of the Linac. It will provide the visible light for measuring the bunch length with a streak camera.

A streak camera is expensive, but it could be borrowed during the commissioning phase until the laser scan method, presented below, becomes possible. An alternative instrument instead of the streak camera could be a dissector commercialized by Femscan or from Novorsibirsk.

After the commissioning phase that will bring the Compton X-ray flux to a detectable level, it becomes possible to measure the amount of X-ray versus the laser trigger time with respect to the electron bunch after it is injected into the Storage Ring.
For that application, one needs both the laser pulse length and the trigger stability to be about 10 times less than the electron bunch length.

4.6.4.4] Transverse profile measurements

An emittance monitor after the quadrupole scan method is installed at the end of the Linac and another one at the end of the transport line before the beam is injected into the Ring. The low emittance requires a good beam size resolution; it can be reached with a YAG (Yttrium Aluminum Garnet) screen inserted into the beam.
For the Storage Ring, the emittance can be monitored with a synchrotron radiation monitor. Although the critical wavelength is in the infrared (1.5 µm), there should be enough photons within the 0.4-to-0.8 µm sensitivity spectrum of standard CCDs.One can also think of transverse scans of the electron beam with a transversally smaller laser beam, but it looks like a delicate and tedious measurement.

4.6.4.5] Beam dump

A low power (3W) beam dump, similar to the SOLEIL Linac dump is foreseen at the end of the Linac. After 20 ms in the storage ring, the spent beam could be extracted and directed into a 3 W and 50 MeV dump.

4.6.5] Vacuum

4.6.5.1] Pumping distribution in the ThomX ring

First calculations of outgassing have been realized in order to have a first estimation on the ion pumps localization . The calculation does not consider punctual and dynamical outgassing. In addition, the pressure gradient estimation has been carried out taking into account an approximate length and shape of the tube. Even the technology of the vacuum chamber is not definitively chosen. The main requirements are listed in table 17. The ion pump corresponding to the conductance of the pumping T are :

- DN 40 : « VacIon Plus 40 Varian » $S_0 = 3.10^{-2}$ $m^3.s^{-1}$ (N_2 equivalent)
- DN 100 : « VacIon Plus Varian » $S_0 = 6.10^{-2}$ $m^3.s^{-1}$ (N_2 equivalent)

A cylindrical inox chamber has been considered for the ring and a rectangular one for the optical cavity which is integrated in the dipole. The outgassing is uniformly distributed. The repartition of the ion pumps on this specific low conductance chamber has been done in the ring available space. Then the outgassing rate necessary to obtain the limit vacuum along the chamber has been determined. Two ion pumps have been disposed before the mirrors at the chamber end.

Designation	**Value**
Vacuum pressure	<3 10^{-7} Pa
Diameter of the beam pipe	40 mm
Specific conductance of the beam pipe	7.9 10^{-3} m^3 m s^{-1}
Dimensions of the rectangular chamber of the optical cavity	25 x 85 mm
Specific conductance of the rectangular chamber of the optical cavity	1.37 10^{-2} $m^3.m.s^{-1}$
Outgassing rate considered for inox τ	2.10^{-8} $Pa.m.s^{-1}$
Conductance of the pumping T	DN 40 : 6.4 10^{-2} $m^3.s^{-1}$,DN 100 :0.25 $m^3.s^{-1}$
Estimated area of the mirrors pots A	0.38 m^2

Table 17 : Vacuum system main requirements

In figure 39, the repartition of the ion pumps is shown on a quarter of the ring. Space for insertions is available:

- 1. Before the dipole, between the two quadrupoles
- 2. After the dipoles, between the two quadrupoles
- 3. At the middle of the free section

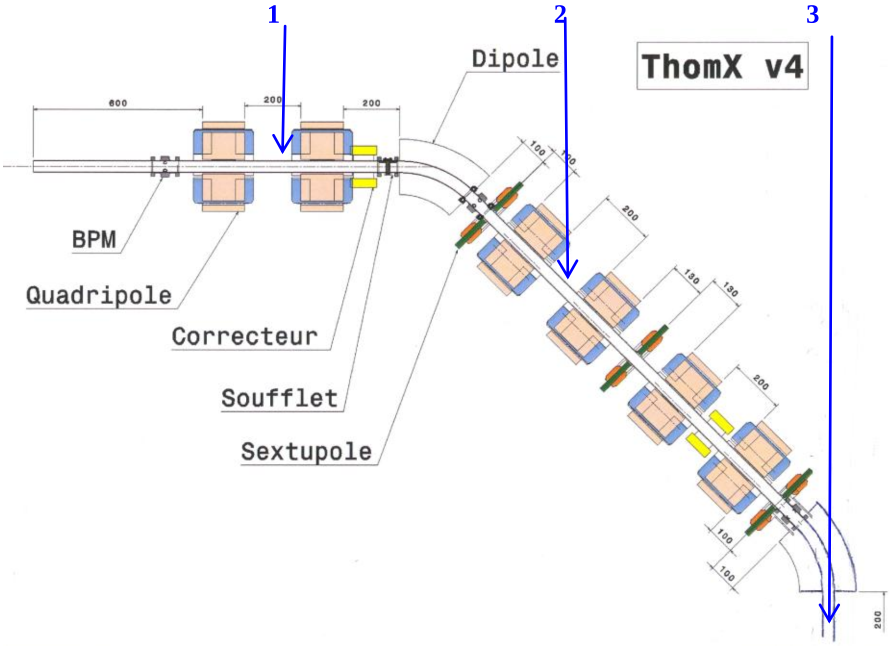

Figure 39 : Localization of the ion pumps on a quarter of the ring

In fig.40, the repartition of the ion pumps is shown on a quarter of the ring with the optical cavity. Insertions are possibles:

- 1. Before the dipole, between the two quadrupoles
- 2. After the dipoles, between the two quadrupoles
- 3. Before the mirrors pot

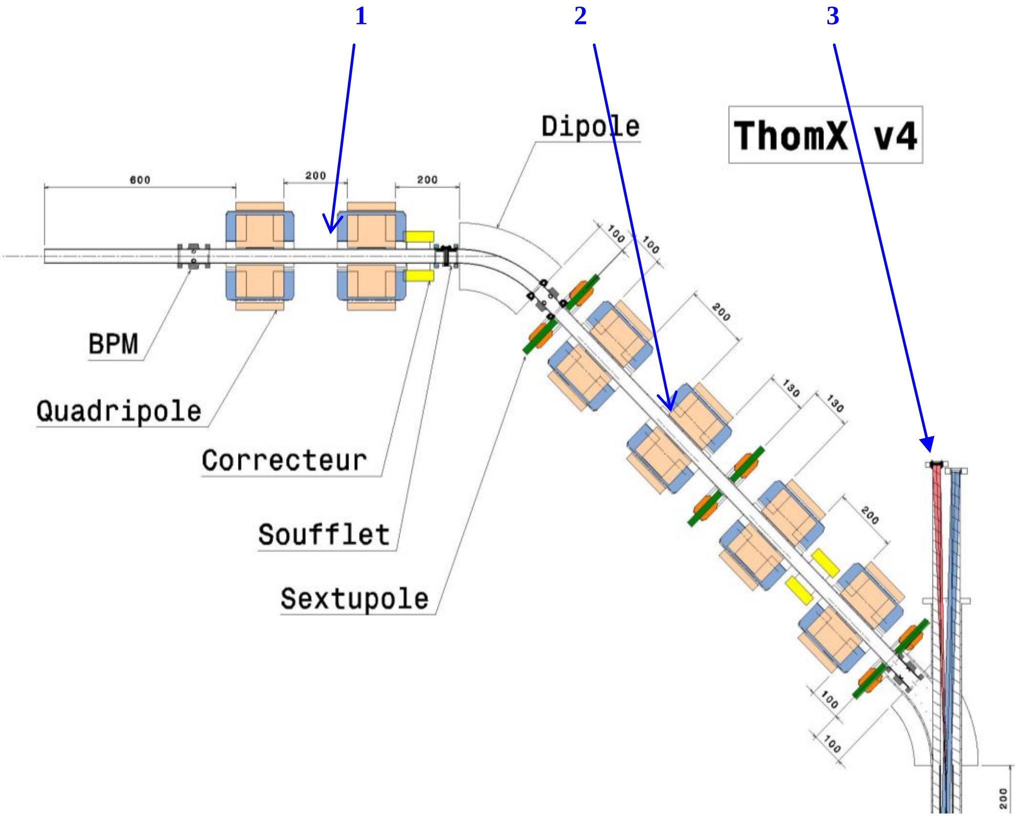

Figure 40 : Implantation of the ion pumps on a quarter of the ring with the optical cavity.

Fig.41a,b illustrate respectively the pressure along the quarter ring including or not the optical cavity. The maximum vacuum pressure is attained between the pumps 2 and 3. Its value is 3.23 10^{-7} Pa without considering the optical cavity and 4.18 10^{-7} Pa including the optical cavity. The minimum vacuum pressure is in both cases less than the desired value of 3 10^{-7} Pa. Neglecting the outgassing of the optical cavity, the desired vacuum pressure is almost attained on a quarter of the ring. However, as far as the optical cavity is concerned the vacuum pressure is affected. The desired pressure is obtained only on a half of the quarter of the ring. Additional available drift spaces should be envisaged especially near a sextupole. An increasing of the pumping T capacity can be also considered. In addition, it is possible to improve the outgassing rate of the beam pipe from 2 10^{-8} to 10^{-9} Pa. m. s^{-1}. In all cases, it is necessary to in situ bake all the vacuum chambers (with a rate $\tau < 2\ 10^{-8}$ Pa.m.s^{-1}) to obtain this vacuum pressure values without electron beam.

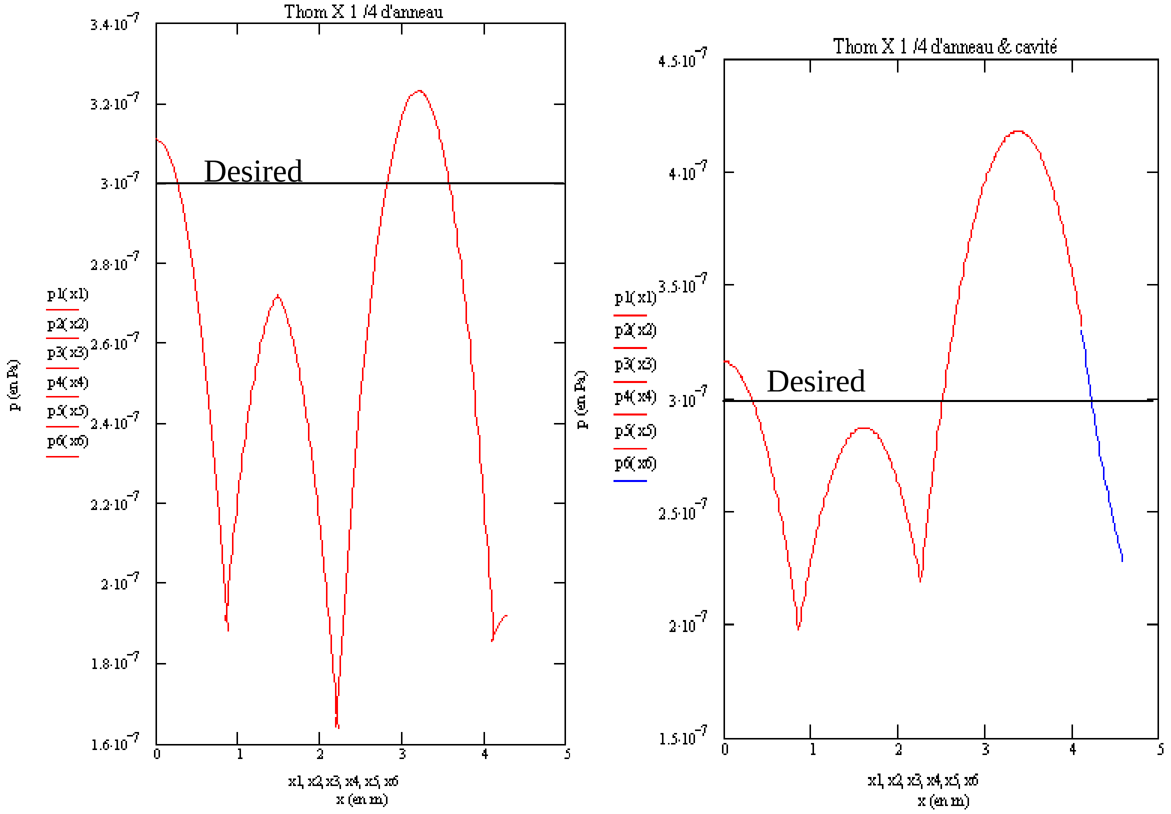

a) b)

Figure 41 : Pressure along the beam pipe. a) without the optical cavity, b) considering the outgassing of the optical cavity. In red: vacuum of the ring, in blue: vacuum of the optical cavity.

4.6.6] Synchronization

An efficient X-ray production requires a precise synchronization of the three main components of the set-up, namely the injector, the storage ring and the optical cavity.

i. The time at which the electron bunches are injected in the storage ring must correspond to the synchronous phase of the ring RF cavity.

ii. The electron bunches circulating in the ring and the photon bunches going back and forth in the Fabry-Perot cavity must go through the interaction region at the same time.

iii. In order to minimize the linac (i.e. the injector) energy jitter, the laser light pulses that strike the photocathode must be synchronized with the phase of the RF wave that accelerates the photo-produced electrons.

Let us look at these three constraints in some more detail. We will require that the overall decrease of the X-ray yield integrated over a machine cycle (whose duration is 20 ms), due to synchronization errors be less than ~30%, it follows that the loss due to errors in either one of the three synchronizations mentioned above must be less than ~ 15 %.(i) If the e^- bunches produced by the linac are injected in the storage ring when the RF cavity phase differs from the one of the synchronous particles, the electrons will undergo collective synchrotron oscillations whose damping is negligible during the 20 ms cycle. The effective bunch length is then increased and the luminosity reduced. An error in the injection time may come either from an error in the timing of the linac gun laser or from some change in the length of the electrons' path between the photocathode and the injection point in the storage ring. A $\Delta t = 1$ ps error in the injection time translates into a 0.18° shift with respect to the synchronous RF phase and generates coherent synchrotron oscillations whose amplitude is .3 mm for those electrons which are at the centre of the injected bunch and which have the nominal ring energy. For reference, the e^{-} bunch length is about 6 mm (rms) at injection, and then increases up to about 9.5 mm at the end of a cycle. It follows from these numbers that one must impose an upper limit of ~13 ps on Δt. As far as the e^{-} path length is concerned, it turns out that the constraint bearing on the linac energy jitter implies that the jitter of the transit time in the transfer line that connects the linac to the ring is negligible.

(ii) One has to ensure a proper overlap of the electron and the photon bunches while they travel in opposite directions in the interaction region. Since the transverse dimensions of both bunches are ~ 70 μm (rms) and the crossing angle is 2°, electron-photon collisions take place in a region whose *total* length is 8 mm. The photon bunch is assumed to be 1.5 mm long (rms) during the whole machine cycle while, as stated above, the electron bunch length is 6 mm (rms) at the beginning of a cycle, and is about 60% longer at the end of a cycle. Thus, at the beginning of a cycle, the two bunches would essentially miss each other if the difference between the times at which they pass the centre of the interaction region differ by more than ~ 40 ps. In absence of collisions, the lengthening of the e^{-} bunch would be very slow and a low luminosity would prevail during the whole 20 ms cycle. In order not to loose more than ~15% of the X-ray produced over a cycle, the times at which the two bunches travel through the interaction region should not differ by more than ~10 ps.

(iii) Finally, when the linac beam energy differs from the storage ring nominal energy, again the injected electrons undergo coherent synchrotron oscillations. More precisely, a $\Delta E/E$ error in the linac beam energy generates synchrotron oscillations whose amplitude is ~20 mm x $\Delta E/E$, where $\Delta E/E$ is expressed in %. Taking into account the initial e^{-} bunch length and its increase during a 20 ms cycle, one finds that the linac energy jitter should be kept below 0.2 %. Let us recall (cf. the section devoted to injection matching in § 4.5.8) that the injection phase of the e^{-} bunch produced by the linac photocathode will be shifted by 6° with respect to the peak electric field phase, and that the transfer line between the linac and the ring will perform a rotation of the bunch energy-displacement ellipse. This injection procedure implies that the above constraint on the maximum energy jitter translates into a maximum 1 ps jitter of the e^{-} gun laser pulse.

Furthermore, experience shows that in order to minimize energy jitter, the timing of the linac pulses must remain the same with respect to the mains' 50 Hz alternating voltage.

Synchronization	Purpose	Maximum error
e^{-} bunch injection time vs. the ring synchronous phase	To avoid coherent synchrotron oscillations in the ring	13 ps
e^{-} bunch and photon bunch running through the interaction region	To avoid luminosity losses	10 ps
Linac photocathode laser pulse wrt to the linac RF phase	To avoid linac beam energy jitter that generate coherent synchrotron oscillations	1 ps
Linac pulse wrt the mains' alternating voltage	To avoid linac beam energy jitter	0.2 ms

Summary of the synchronization constraints

The specifications obtained above are stringent but not beyond the present state-of-the-art. To meet them, we propose to implement the synchronization scheme shown in fig.42. Its main features are the following ones:

(1) The overall timing is provided by a 10 MHz master clock whose signal is fed to frequency multipliers and dividers in order to drive each one of the items involved in the synchronizations described above.
(2) The laser that feeds the Fabry-Perot cavity will be locked to the optical cavity resonance frequency.
(3) Small drifts of the Fabry-Perot cavity frequency will be taken into account by feeding these changes back to a 500 MHZ synthesizer which is itself driven by the master clock.
(4) The ring RF cavity will be driven by this 500 MHz synthesizer and thus its frequency will be locked to the resonance frequency of the optical cavity in order to avoid uncontrolled drifts between the times at which the electron and the photon bunches travel in the interaction region.
(5) An input from the mains' 50 Hz alternating voltage will be used to fulfill the last requirement of § iii above.

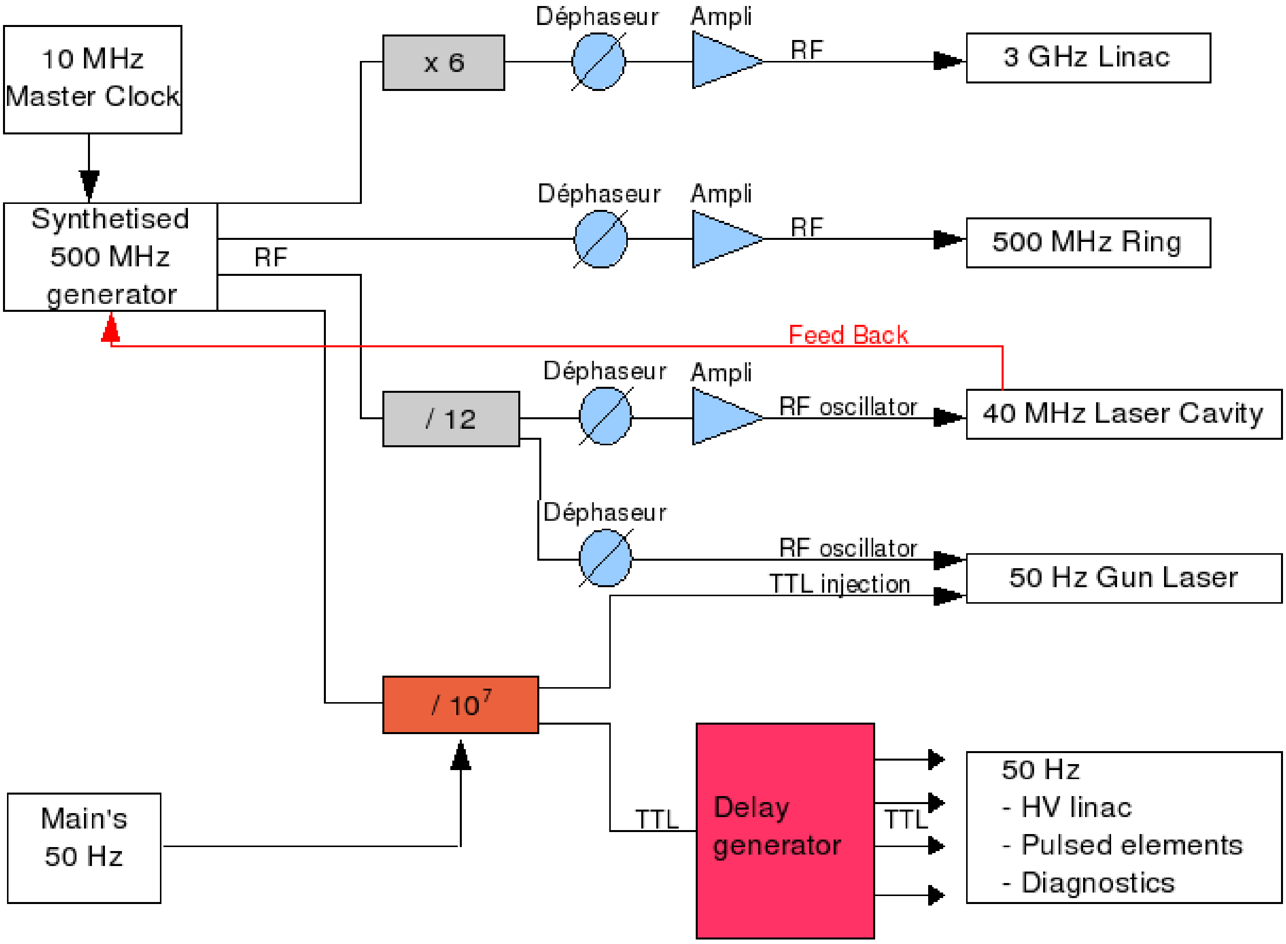

Figure 42: Sketch of the timing distribution

4.6.7] X ray beam extraction and characterisation

The principle of the characterisation of the X-ray beam is shown on fig.43. The aim is to measure the X-ray beam spectral intensity distribution, the beam divergence and its transverse spatial shape.

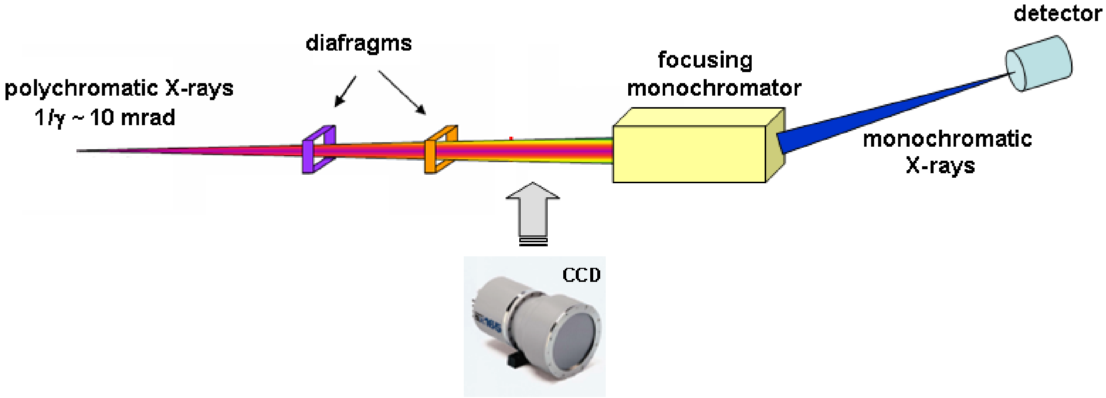

Figure 43 : Principle of the X-ray beam characterisation.

Taking into account the position of the cavity mirrors located at 1 m from the electron beam-laser beam interaction point, the angular acceptance of the X-ray beam is around 10 mrad. Hence, the transverse size of this polychromatic X-ray beam entering into the first optical element is around 1 cm.

After passing through diaphragms, the polychromatic beam is diffracted by a monochromator which consists to a double Si crystal allowing to select and focus a wavelength of light passed through: as the angle of the monochromator is changed, the wavelength "color" of the light exiting also change, as shown on fig.44.

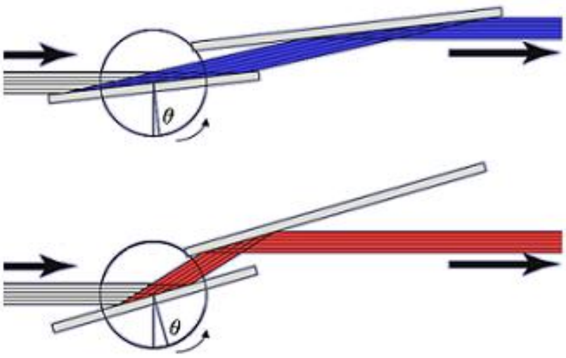

Figure 44 : Principle of a rotating double crystal monochromator: "white" light enters from the left and "monochromatic" light exits to the right with a "color" depending on the angle θ.

The detection system could be a Cadmium telluride (CdTe) sensor [37] which has a good stopping power with efficiency around 100% up to 50 keV. By rotating the monochromator and measuring the corresponding flux entering the CdTe photodiode, the spectral intensity distribution of the beam can be reconstructed.

Also for measuring the transverse spatial shape, the position and the divergence of the X-ray beam, a CCD X-ray detector with a large active diameter area (as a MarCCD camera [38] for instance) should be insert in the beam line as shown on figure 1.

References

[1] : "Conception of photo-injectors for the CTF3 experiment", R. Roux, Proceedings of the 46th workshop of the INFN ELOISATRON project, The Physics and applications of high brightness electron beams, 9-14 Octobre 2005, Erice, Italie, World Scientific, the science and culture series, 237-253.

[2] : "First full beam loading operation with the CTF3 linac", R. Corsini *et al*, Proceedings of the 9th European Particule Accelerator Conference, EPAC04, Lucerne, Suisse, 39-41.

[3] : "The LEP Injector Linac", R. Bossart, J. P. Delaye, J. C. Godot, J. H. B. Madsen, P. Pearce, A. Riche, L. Rinolfi, CERN/PS/90-56 (LP).

[4] : "Emittance growth due to the laser non-uniformity in a photo-injector", F. Zhou *et al*, proc. of the 8th Eur. Part. Acc. Conf. EPAC2002, Paris, p. 275, 2002.

[5] : "A shaper for providing long laser target waveforms", S. Cialdi and I. Boscolo, Nucl. Instr. Meth. in Phys. Research **A 538** (2005), 1.

[6] : "Commissioning of the Linac Coherent Light Source Injector", R. Akre et al, Phys. Rev. ST Accel. Beams **11**, 030703 (2008)

[7] "Sub-picosecond bunch length measurement at the TESLA test Facility", M. Geitz, G. Schmidt, P. Schmüser, G. V. Walter, Nucl. Instr. Meth. A **445**, 343 (2000).

[8] "TRANSPORT: a computer program for designing charged particle beam transport systems", K. L. Brown and F. Rothacker, SLAC, D. C. Carey, FermiLab, Ch. Iselin, CERN, CERN 80-04, 1980.

[9] J. Payet, Beta Code, CEA, SACLAY

[10] J.B. Murphy et al., Longitudinal Wakefield for an Electron Moving on a Circular Orbit, Vol. 57, Part. Acc. 1997.

[11] K. Bane, M. Sand, The Short-Range Resistive Wall Wakefields, SLAC-PUB, 95-7074.

[12] R. Nagaoka et al., Recent Studies of Geometric impedance At SOLEIL, PAC2006

[13] P. Fernandes, R. Massarino, R. Parodi, A.Tarditi (INFN, Italy), A. Massarotti (Sincrotrone Trieste, Italy), "The Design of the R.F Cavities for ELETTRA", IEEE, 1989

[14] W. Bruns, website : http//www.gdfidl.de

[15] Z. Huang and R. D. Ruth, Laser-Electron Storage Ring, Phys. Rev. Lett. 80, 976 (1998)

[16] C. Bernardini, G. F. Corazza, G. Di Giugno, G. Ghigo, J. Haïssinski, P. Marin, B. Touschek, Phys. Rev. Letters 10, p. 407 (1963)

[17] H. Bruck, Accélérateurs circulaires de particules, Ed. Bibliothèque des Sciences et techniques, p. 309 (1966).

[18] K. Ohmi, Phys. Rev. E **55** 7550 (1997)

[19] S. Haifets, D. Teytelman, Phys. Rev. Spec. Top. Acc. and beams **8** 064402 (2005)

[20] E. Weihreter, Compact synchrotron light sources, Series on Synchrotron Radiation Techniques and Applications - Vol. 3, World Scientific.

[21] Y. Baconnier, A. Poncet, P. Tavares, neutralisation of accelerator beams by ionisation of the residual gas, CERN-PS-94-40 (1995).

[22] A. Chao and M. Tigner, handbook of accelerator physics and engineering, world scientific.

[23] A. Poncet, Ion trapping and clearing, proceedings of the CERN accelerator school, edited by S. Turner CERN 90-04 p74 (1990).

[24] P. Elleaume, O. *Chubar*, J. Chavanne, Proceedings of the PAC, *Vancouver*, Canada, *1997*, p. 3509.

[25] P. Lebasque, et al., Synchrotron SOLEIL, « Eddy current septum magnets for booster injection and extraction, and storage ring injection at Synchrotron SOLEIL », EPAC 2006, Edinburgh, Scotland.

[26] P. Lebasque, et al., Synchrotron SOLEIL, « Four matched kicker systems for the SOLEIL storage ring injection, a full solid-state solution of pulsed power supplies working at high current », EPAC 2006, Edinburgh, Scotland.

[27] B.I. Grishanov et al., DESY, « Very fast kicker for accelerator applications », Note TESLA Collaboration 96-11, November 1996.

[28] D. Alesini et al., INFN/LNF, Frascati, Roma, “Design and tests of fast kickers for the DAΦNE collider and the ILC damping rings”, 2006.

[29] P. Lebasque, et al., Synchrotron SOLEIL, « Optimisation of the coating thickness on the ceramic vacuum chambers of SOLEIL storage ring”, EPAC 2006, Edinburgh, Scotland.

[30] F. Marhauser, E. Weihreter (BESSY), “Impedance Measurements of the HOM-Damped 500 MHz Metrology Light Source Cavity”, BESSY Gmbh, Germany, 08 January 2007.

[31] M. Langlois, P. Sanchez, M. Cornelis, F. Perez (ALBA), “Measurements on the RF cavity for the ALBA storage ring”, Proceedings of EPAC08, Genoa, Italy.

[32] R. A. Rimmer (Lawrence Bekeley Lab.) *et al.*, “Development of a high-power RF cavity for the PEP-II B factory”, DE-AC03-76SF00098 (LBL).

[33] P. Fernandes, R. Massarino, R. Parodi, A.Tarditi (INFN, Italy), A. Massarotti (Sincrotrone Trieste, Italy), ”The Design of the R.F Cavities for ELETTRA”, IEEE, 1989.

[34] M. Svandrlik, A. Fabris, C. Pasotti (Sincrotrone Trieste), ”Improvements in curing coupled bunch instabilities at ELETTRA by mode shifting after the installation of the adjustable higher order mode frequency shifter (HOMFS)”, IEEE 1998.

[35] W. Bruns, web site: http://www.gdfidl.de

[36] N. Rouvière, Le joint composite, Journées d’étude de la SFV « les joints d’étanchéité », Noisy-le-Grand, 10-11 décembre 2002.

[37] http://www.amptek.com/x123cdte.html

[38] http://www.marresearch.com/pdf/Brochure.sx165.pdf

CHAPTER 5: Radioprotection and Integration

5.1] Radiation Shielding Design

The radiation safety design is based on calculations on radiation outside the shielding. The dose limit we employed at the boundary area is 0.5 μSv/h.

The beam characteristics used for simulations are: energy 50 MeV, mean current 50 nA, mean power 2500 mW.
The required thickness is obtained for worst-case conditions, i.e. intentional beam losses in beam dump mounted in the straight line of the electron beam pipe. The full beam power is scattered on a solid cylinder of copper target, placed in a cylindrical lead shield envelope. But we have to keep in mind that we have also an injection area in the storage ring where we loose a part of beam and another beam dump for the beam extracted from the storage ring.

To do investigations we use a multi-particle transport code Fluka [1,2], using a Monte Carlo method. To obtain a good estimation of the shielding we need 100 millions of requested annihilation samples.

Owing to the incertitude on the location of the machine, we study two problems geometries. The first one is an existing room (10.60 m by 5.90 m) of Institut Gustave Roussy (IGR) and the second one is in a building so called ”Aile7” of LAL. The Aile7 building has a width of 11.50 m where we have to build walls to enclose the accelerator. In each case we have to increase thickness of all existing walls.

The first radiation leakage was calculated, using empirical formula and leads to a concrete (density 2.35 g/cm^3) thickness of 1.7 m, which gives a starting point for the thickness of the walls. The aims of the calculations are to optimize the structure of the beam dump and to minimize walls.

Most of the preliminary simulations are done in the IGR room hypothesis with only 5 millions of primary histories in the run to reduce the computer time.

For the dump we choose a cylindrical beam dump located 2 m from the end of the linac, having a lead length of 40 cm and a radius of 30 cm, with inside, at 10 cm of its entrance face, a copper cylinder of radius 4 cm and 4 cm length.

With this type of beam dump, we found that walls composed of lead in front the concrete walls allow one to drastically reduce the thickness of the shielding (1.05 m instead of 1.7 m. The composition of these global walls is 25 cm of lead and 80 cm of concrete. As far as the roof is concerned we put 1.00 m of concrete and for the hall floor, 25 cm of concrete, assuming we are on ground, which is the case in the two hypotheses.

In each implantation we have a 10 cm thickness door of lead with a chicane.

In the figure the colour scale is in μSv/h

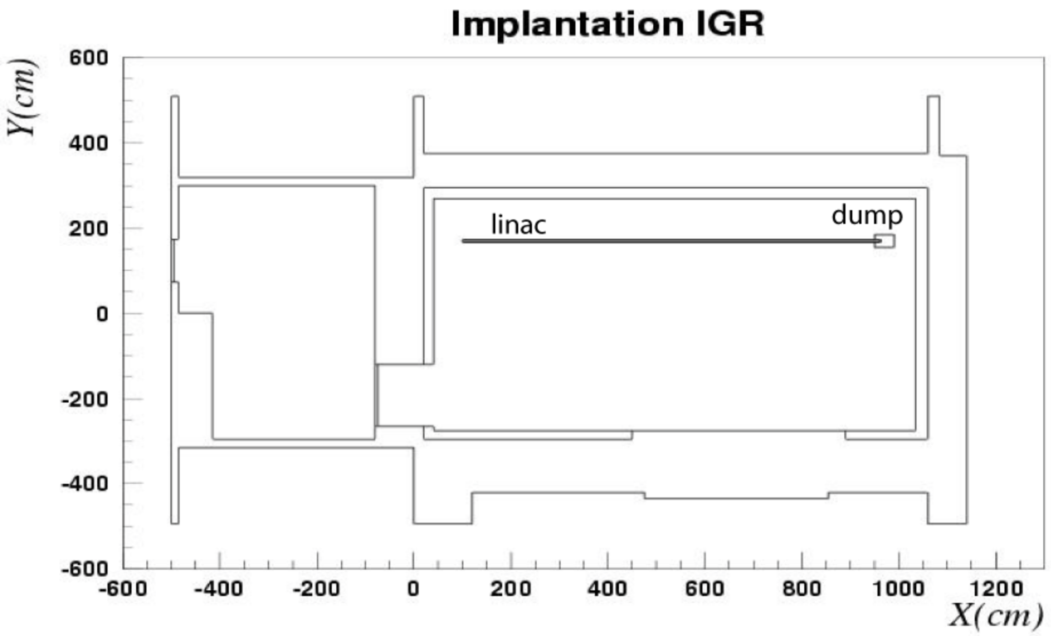
Implantation IGR
Y(cm)
600
400
200
0
-200
-400
-600
-600
-400
-200
0
200
400
600
800
1000
1200
X(cm)
linac
dump

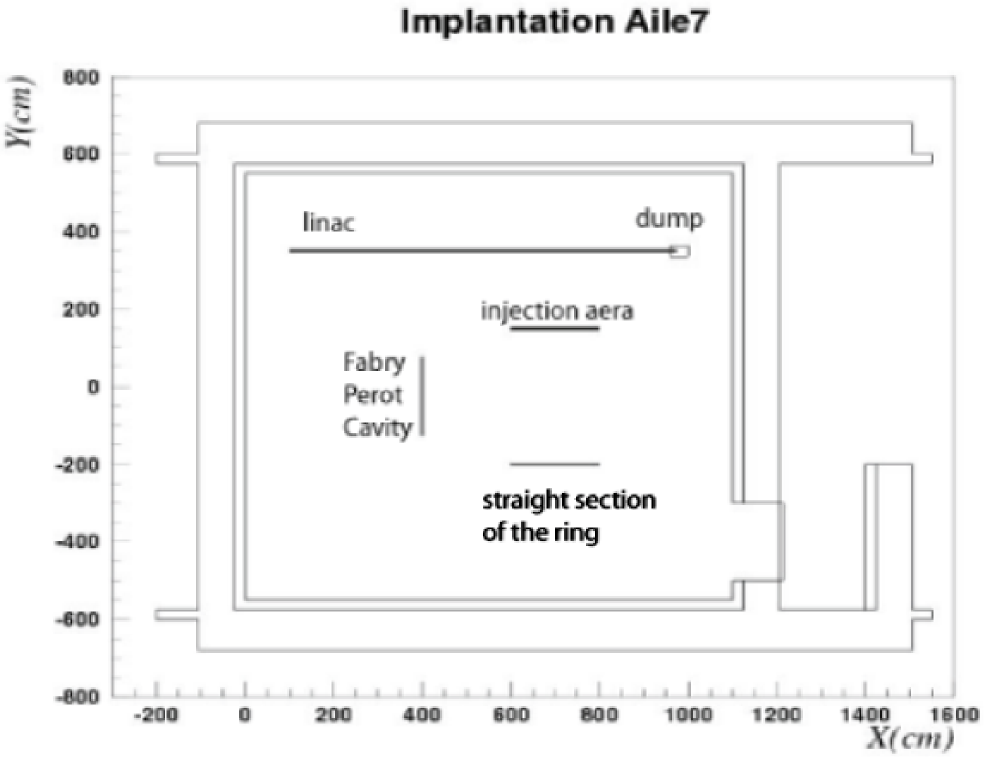
Implantation Aile7
Y(cm)
800
600
400
200
0
-200
-400
-600
-800
-200
0
200
400
600
800
1000
1200
1400
1600
X(cm)
linac
dump
injection aera
Fabry
Perot
Cavity
straight section
of the ring

Implantation IGR

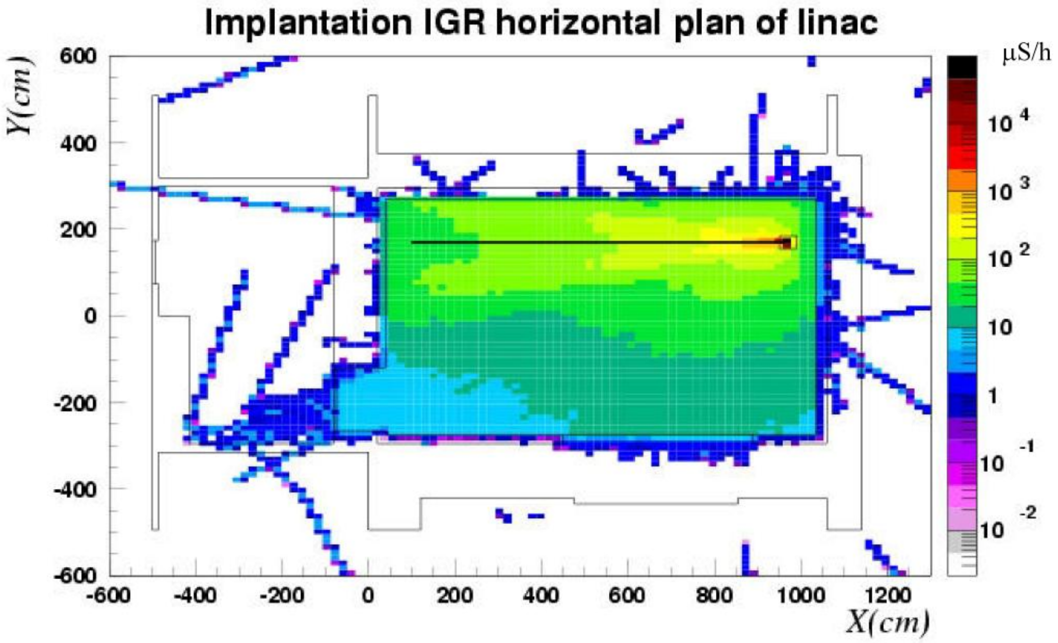

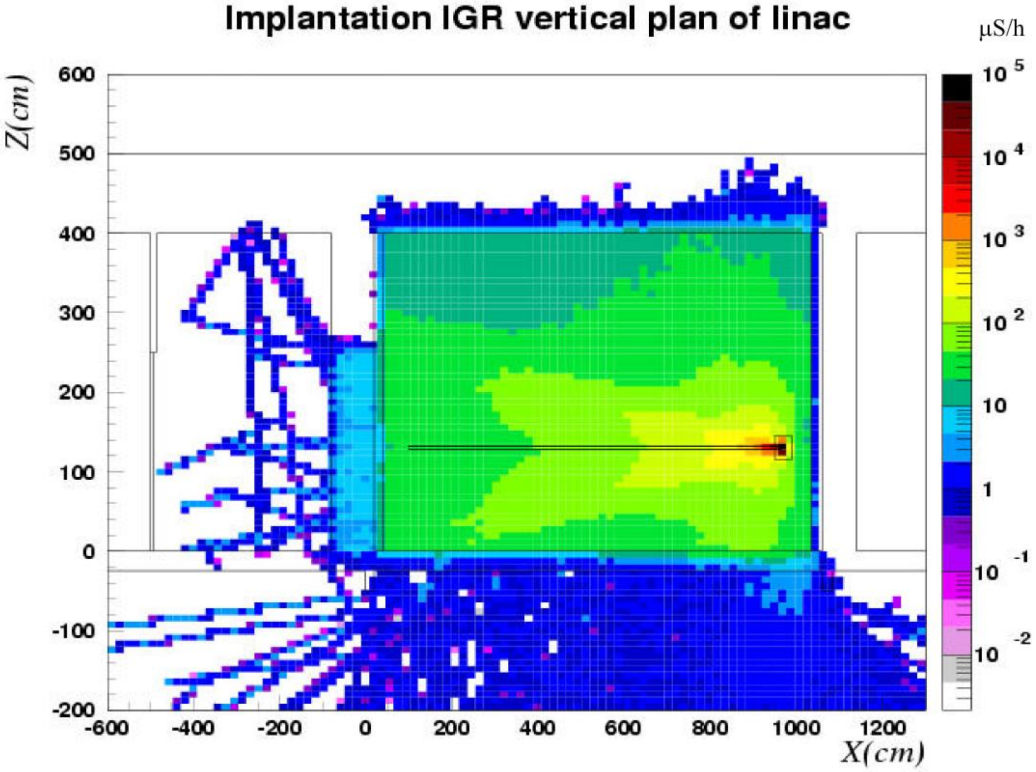

Implantation Aile7

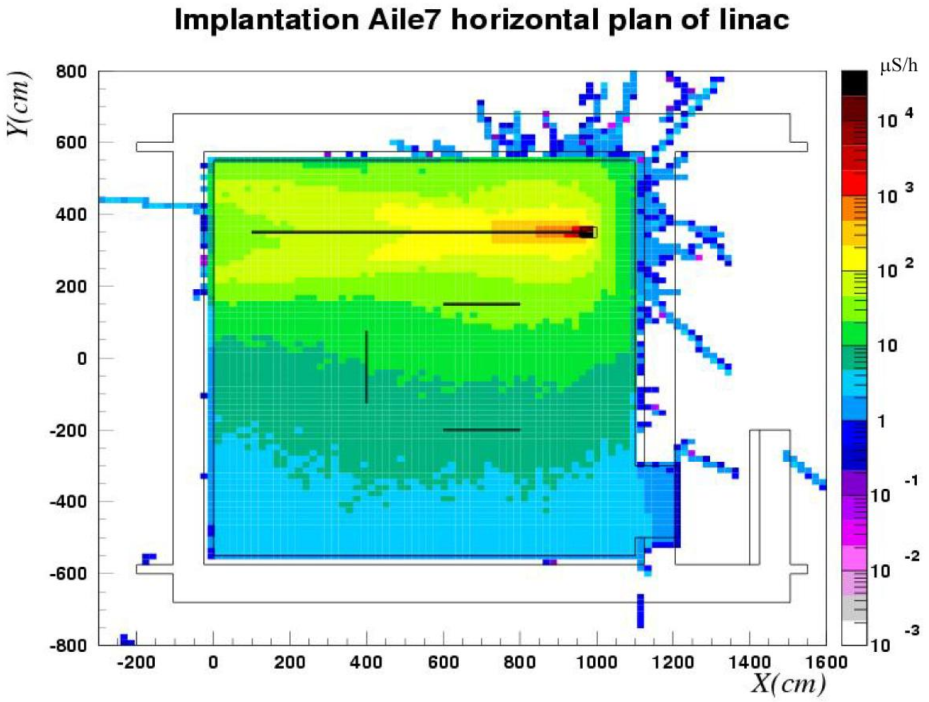

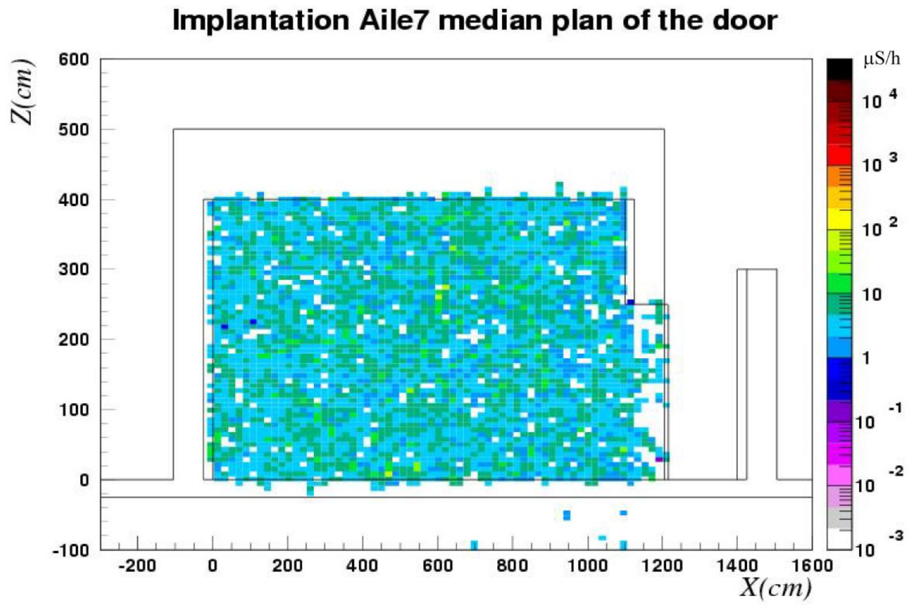

References

[1] “The FLUKA code: Description and benchmarking”, G. Battistoni, S. Muraro, P.R. Sala, F. Cerutti, A. Ferrari, S. Roesler, A. Fasso, J.Ranft, Proceedings of the Hadronic Shower Simulation Workshop 2006, Fermilab 6—8 September, M. Albrow, R.Raja eds. AIP Conference Proceeding 896, 31-49, (2007)

[2]“FLUKA : a multi particle transport code”, A. Fasso, A. Ferrari, J. Ranft and P.R. Sala, CERN-2005-10 (2005), INFN/TC_05/11, SLAC-R-773

CHAPTER 6 : ERL and LINAC solutions. Feasibility considerations

6.1] Introduction

Different accelerator scheme have been envisaged before choosing the ring solution. As shown in previous sections, the Compton interaction can spoil the quality of the beam and therefore the X-ray flux. It is therefore important to compare the two solutions, either with renewing the electron bunches after each interactions, or without (storage ring case). Unlike storage ring, the electron bunches in single pass linacs are renewed at each Compton interaction. The significant advantage is that the beam quality is preserved for each interaction. In return, the difficulty lies in obtaining either a high repetition rate (normal conducting cavities) or large enough charge to achieve a similar flux as in storage rings. In this section, we will compare the alternative linacs possibilities for the project.

6.2] Normal conducting LINAC

The simplest configuration is to suppress the ring, and to keep the linac alone to interact with the laser in the Fabry-Perot. In this case, the bunch length can be smaller (4ps) than in the ring (20ps), but the repetition rate is decreased from 20.8 MHz to 100-200 Hz hence reducing drastically the Xray flux (see Table 1). The flux can be enhanced with a bunch train inside the macropulse. In this case, the X-rays flux is no more continuous. Moreover, it is difficult and costly to produce such a scheme with a photoinjector. An experience has been already developed on ELSA at the CEA Bruyères le Châtel. ELSA can produced typically 10000 electron bunches at 20 Hz (bunches are at 144 MHz of repetition rate) with 1 nC charge, a bunch duration of 30 ps and a normalised emittance of 3 π mm mrad. The major drawback of such a scheme is the relatively high cost to produce such bunches with a photoinjector, and an X-rays flux, which is no more continuous. To decrease the cost and having a simplest user installation, thermoionic guns may be used instead of a photoinjector but the emittance can be consequently degraded. For example, with a thermoionic gun (or field-emission) one can provide at 20 Hz 10000 bunches (pulsed at 1-3 GHz) with 0.2 nC and an emittance (normalised) of 20 π mm mrad. As a consequence, the fabry perot must be adjusted at the bunch repetition rate (reducing the cavity length or injecting several pulses in the optical cavity). Then, considering the same energy stored in the cavity, the level of energy per pulse is smaller in this case than for the ring case.

.

6.3] Superconducting LINAC

Another competitive alternative is a superconducting linac enabling high repetition rate to the detriment of the cost being two to three times higher than the ring solution. In order to achieve a similar flux as in the case of the storage ring, studies have been done for a linac of the ERLP type [1]. Changes were made in order to meet the requirement of compactness of the project.

A superconducting linear accelerator coupled to a DC photocathode gun is chosen to produce high repetition rate electron bunches. Achieving a similar emittance as the storage ring case leads to limiting the electron bunch charge in the hundreds of picocoulombs. The choice of high repetition rate and bunch duration (in the order of tens of ps) requires a JLAB DC gun-type with a GaAs photocathode [2]. Because of the properties of this type of photocathode and the relatively low DC voltage (350 kV), electron bunches will be produced quite long. As the desired length is about 10 ps, it is necessary to use a buncher which could be a normal conducting cavity at 1.3 GHz, similar to that used at ELBE [3]. Two solenoids after the gun and the buncher are necessary for transverse focusing and compensation of the increase in emittance due to the space charge force. Upwards of the second solenoid, the transfer line of the beam is identical to that employed for ERLP. Simulations were carried out using the computer code ASTRA [4], which takes into account the space charge effect. The laser is supposed to have a Gaussian longitudinal distribution of 20 ps rms duration and a radial distribution with a radius of 2.4 mm.

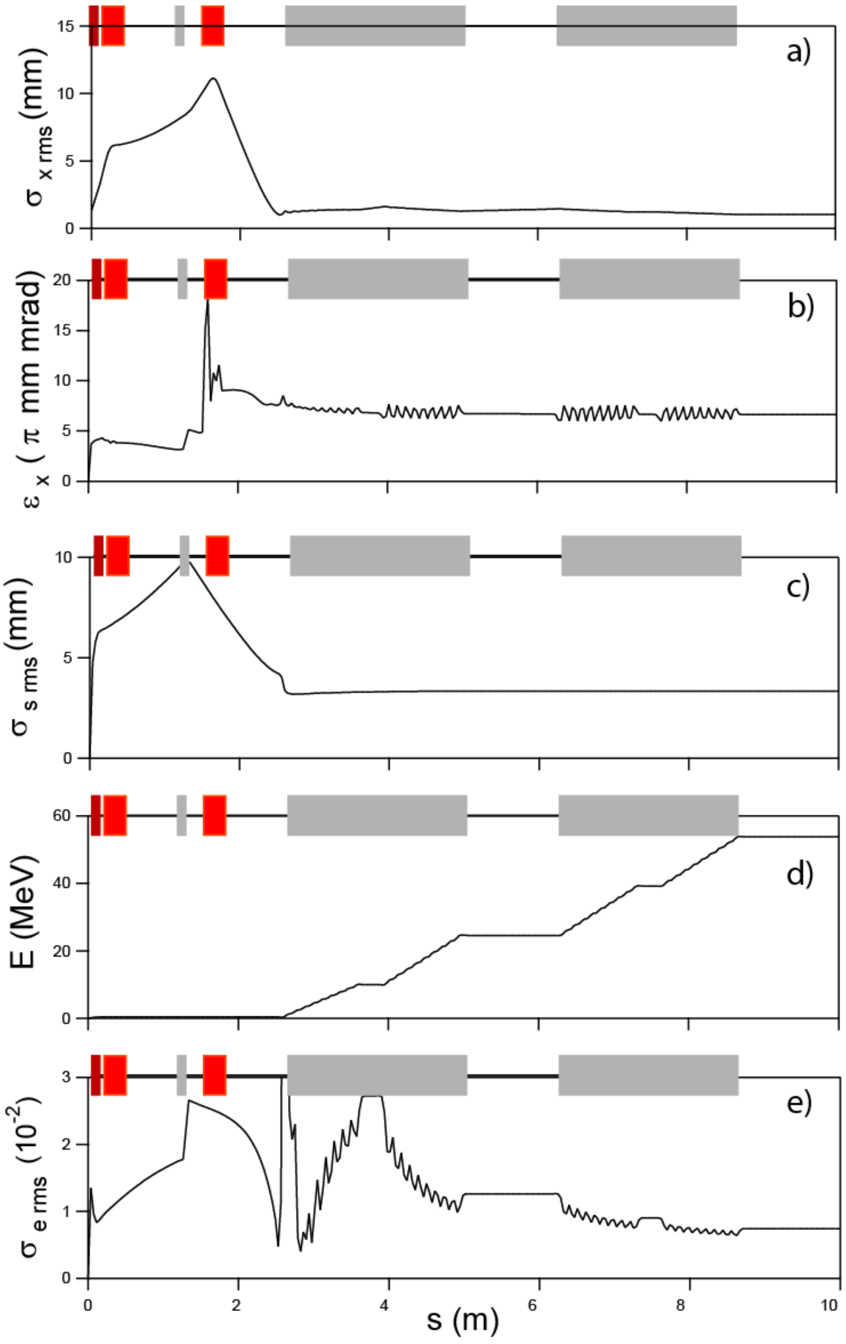

Figure 1 : Electron bunch characteristics along the accelerator. a) rms transverse horizontal size, b) horizontal normalized emittance, c) rms longitudinal dimension, d) energy, e)energy spread. maroon) gun, red) solenoids, grey) accelerating cavities.

Fig.1 illustrates the characteristics of the beam along the accelerator. After the gun (s = 0m) and a solenoid (s = 23 cm), the emittance reaches 4 π mm mrad for a charge of 0.3 nC and an energy of 350 keV. It is important to note that the total emittance results from several contributions, including a component of thermal emittance ε_{th}, a component related to the effects of space charge ε_{sc}, a RF component ε_{rf}, generated by field non linearities and it expressed as follows:

6.1) $\varepsilon_{x,y} = \sqrt{\varepsilon_{th}^2 + \varepsilon_{sc}^2 + \varepsilon_{rf}^2}$

The lowest achievable emittance is limited by the thermal component. In our case, for a GaAs photocathode with a radius of 2.4 mm, it is 1 π mm mrad [5]. Its contribution to the emittance may be reduced in the case of an ellipsoidal distribution of the laser (parabolic in the three directions). However, it remains reasonable in the case of a cylindrical distribution. The largest degradation is for a Gaussian distribution as presented here. The rf component is not a major contribution to the increase in transverse emittance. On the other hand, the longitudinal emittance is dominated by the space charge forces and the nonlinearity of the rf fields. Although solutions exist to compensate for the non-linearities, the longitudinal emittance being not a limiting factor for the Compton radiation, they will not be considered here.

Due to the space charge forces, the bunch lengthens up to 9.8 mm (33 ps). For this reason, a cavity (s = 1.24 m) is necessary to shorten the bunch with "velocity bunching" [6], which reduces the length down to 3.3 mm (11 ps). At this energy of 360 keV, the bunch is sensitive to transverse fields in the cavities since the transverse dimension is large. Accordingly, it is necessary to adjust the transverse dimension of the bunch at the entrance to the first accelerating cavity. This focusing is produced through a second solenoid (s = 1.65 m), which allows to compensate partially the second increase of emittance (6 π mm mrad) due to the reduction of the bunch length.

The use of TESLA-type cryomodules [7], which contain 8 superconducting cavities of nine cells, is proposed. Two such cryomodules are needed for accelerating the beam up to 50 MeV. The main difficulty lies in the first booster cavity for which the electrons are not relativistic and therefore the phase of the bunches with respect to the RF field will vary in time. The initial phase and the amplitude of the field must be precisely adjusted. In order to make the accelerator more compact, the accelerating gradient of the first cavity has been increased up to 19MV/m with a phase shift of 25°, as compared to 9 MV/m and 20° in the ERLP case. In the following cavities the theoretical maximum gradient at 27 MV/m is used with a zero phase shift.

The characteristics of the beam at the end of the linear accelerator are summarized in Table 1. The emittance is 6.4 π mm mrad for a charge of 0.3 nC. The emittance can be improved by shaping the pulse of the laser illuminating the photocathode.

6.4] Comparison of x rays fluxes

Table 1 summarizes the characteristics of the three accelerator schemes. It appears that the ring and the SC linac cases give rise to very similar fluxes but the spectral width is larger in the SC linac case (see fig.2). One must notice that in the SC linac case the bunch is renewed for each interaction, and therefore the flux is constant versus time. The NC Linac achieves worse performances due to its low repetition rate. Contrarily to the ring, the linac can be extended by a magnetic compressor, which can reduce the bunch length and moreover, linacs alone can operate at different beam energies. Concerning the NC linac, we can refer to the performances of CTF3 [8], which can generate about 2000 bunches in few microseconds at 10 Hz repetition.

	SC LINAC	RING	NC LINAC
Energy (MeV)	53	50	50
rms transverse emittances (π.mm.mrad)	6.6	4	4
rms energy spread (%)	0.7	0.3	0.6
RMS bunch length (mm)	3.3	6	1.2
Bunch charge (nC)	0.3	1	1
Repetition rate (MHz)	80	20	$100\ 10^{-6}$
Mean Current (mA)	24	20	$1\ 10^{-4}$
Expected X Ray flux	$2.0\ 10^{13}$	$1.2\ 10^{13}$	$1.3\ 10^{8}$

Table 1: Electron bunch characteristics in the superconducting linac, storage ring and normal conducting linac cases

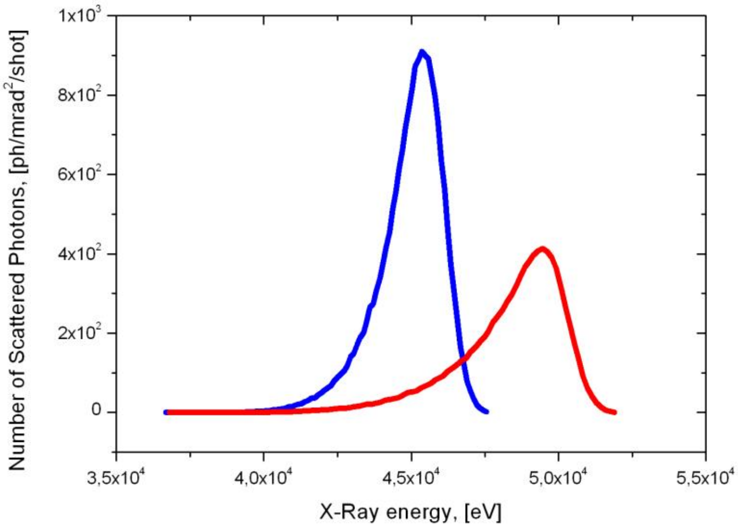

Figure 2 : Spectral distribution of the scattered Xray photons. The red and the blue curves panels respectively the SC LINAC case (or ERL) and the ring case

6.5] Energy Recovery Linac

The RF power needed to operate the SC linac is about 1.2 MW. A way of recovering this energy is to recirculate the beam with an opposite RF phase to the cavity RF field. In our case, one or both cryomodules can be energy recovered thus reducing also drastically the power absorbed by the beam dump.

In the ERL the cumulative effect of cavity misalignments may lead to instabilities. Indeed, when an electron bunch passes through a cavity off-axis, it excites transverse high order modes of the cavity. This excitation creates a transverse force disrupting the particle transverse momentum at the next passage of the bunch in the cavity. Particles transfer energy to transverse modes. By cumulative effect, beyond a given current threshold, the transverse position of the particles can grow exponentially, resulting in the loss of the beam, hence the name of instability: Beam Break Up (BBU) [9]. This instability limits the average current of the accelerator, despite the performance of the gun. It is especially noticeable in the case of an ERL for which instability can be interpreted as a feedback loop between the beam and RF cavities.

In our simulations (using the bi code [10]), we assumed a recirculation loop injected at 24 MeV (see fig.3). The first cryomodule (or booster), which is out of the recirculation loop, will be powered without the energy recovery mode. Accordingly, the recirculation loop includes a single "small" cryomodule. The loop contains the cryomodule and a triplet of quadrupoles on both sides of the cryomodule. The focusing is achieved with a constant gradient which is perfectly adapted to the case of an ERL with low energy electrons. The quadrupoles magnetic length is 15cm and their deflection parameter of 0.5 m^{-2}. The optical functions are symmetrical between the acceleration and deceleration and thus maximize the current threshold of the BBU instability, which is evaluated around 130 mA. In our case, with 80 MHz and 0.3 nC, the average current is 24 mA, which is largely below the BBU current threshold.

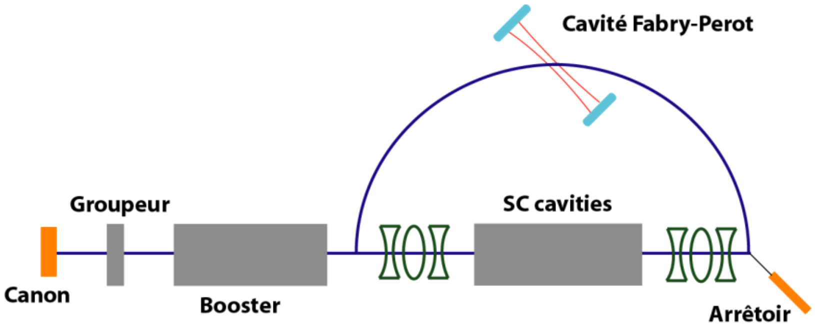

Fig 3 : schematic representation of the ERL for the ThomX project

6.6] Conclusion

Alternative solutions as the SC ERL is very attractive in terms of X-ray flux produced. This solution has been excluded mainly because of the high cost of the installation and the constraint on the maintenance (e. g. Cryogeny), which need an operation expertise. So, this type of accelerator scheme can not be reasonably envisaged for a user installation. Other cheeper installation such as normal conducting linac has been also excluded due to the low level of the X-ray flux produced compared to the ring case. To conclude, the ring configuration appears to be the best arbitration between X-ray source performance, cost and a dedicated to users installation.

References

[1] C Gerth et al., PAC, 1643 (2005)
[2] D.J. Holder et al., LINAC, 93 (2004), http://accelconf.web.cern.ch
[3] E. Wooldridge, et al., EPAC, 467 (2004), http://accelconf.web.cern.ch
[4] K. Floettman, ASTRA code, https://www.desy.de/mpyflo/astra
[5] I.V. Bazarov et al., PAC, 1221 (2007), http://accelconf.web.cern.chAccel
[6] L. Serafini and M. Ferrario, AIP Conf. Proc. 581 (2001)
[7] A. Buchner et al., EPAC, 732 (2000), http://accelconf.web.cern.ch
[8] “First full beam loading operation with the CTF3 linac”, R. Corsini *et al*, Proceedings of the 9th European Particule Accelerator Conference, EPAC04, Lucerne, Suisse, 39-41
[9] F.J. Sacherer, Tranverse Bunched Beam Instabilities – Theory, Proceeding of High Energy Accelerator, 347 (1974)
[10] I. Bazarov, http://lepp.cornell.edu/ ib38/bi

CHAPTER 7: Risk analysis, planning, budget, and industrialization

7.1] Risk analysis

The ThomX design relies on a conservative approach and was carried out by people having a long experience in this field. Therefore we expect no unmanageable risks during the development phase. Main issues are already well prepared thanks to prior investment and developments such as the PHIL test facility to perform photo-injector optimization and the high finesse Fabry-Perot which already demonstrated very promising results. These key on-going developments are far ahead the general schedule and will induce no delays to the global program.
However, even if the required technology is well under control, the beam dynamics of the ring is quite unusual which makes quite challenging the mastering of the Compton X-ray production so as to reach in a stable, reliable and reproducible manner the expected photon flux. This is why such an R&D program is essential.
Moreover there are essential components that will require prototyping (e.g. the laser system at 40 MHz).

Probably the main risk is associated with the limited available resources in skilled people to handle such a large program: the tradeoff is between minimization of costs (but with a risk of a longer development) and subcontracting part of the engineering tasks (with a need of budget increase to cover the associated expenses).

7.2] Planning

The first task will be to perform the complete engineering of the machine (TDR) including:

- Full systems analysis with detailed modelling of the beam dynamics, vacuum and thermal calculations, command/control detailed analysis, drawing for RF, vacuum, electrical and cooling connection
- Complete breakdown of the system in well specified subassemblies
- Subassembly specifications and freezing of the main parameters and well defined interfaces with the other subsystems and the building.
- Detailed drawing for the parts that are not purchased on specifications

This task is planned on a 9 month period

Manpower requirements for the TDR phase:

	FTE	FTE (BE)
Photoinjector Gun	1.2	0.5
LINAC	1.4	0.4
Transport line and ring	2.8	0.6
Fabry Perot	0.1	0.1
Laser and fiber amplifier	2.2	0.2
Control-Synchro	1.0	
Infrastructure, support & cabling	1.6	0.8
Total	10	2.6

A prototyping phase in the TDR concerning the high power laser is strongly recommended. This should increase the required budget of ~100 k€.

The next step will be to develop the key subassemblies that have to be delivered within two years. This allows a sufficient time to prepare the LAL Aile 7 building to accommodate the machine in order to start integration & tests

The integration & tests phase is expected to last one year and will permit to finely tune the machine to the goal performances. It will be done in the exact final configuration as required by the C2RMF (Louvre laboratory) in order to minimize the integration there.

Then, the machine will be dismantled (1 month) and re-assembled identically in the Louvre facility. No major issue is expected during this period and we expect a very quick reinstallation (5 months). This period will include proper training of the future users of the machine.

This scheme permits to limit the integration duration in the Louvre premises to minimum while offering the highest reactivity during the primary installation & tests of the machine due to close connection with LAL/SOLEIL specialists.

7.3] Budget

A preliminary budget estimate has been made, based on what is known at this early CDR stage. It doesn't include any contingency to cover the lack of accuracy in the cost evaluation of the unidentified expenses that may show up when working out a TDR. Usually, at this stage a 15% contingency is considered.

This primary budget estimate considers only the direct costs of the various parts of the machine without any staff costs, and associated management, engineering tasks, integration & tests costs. As a typical rule of thumb for systems of this complexity the total cost including manpower is twice the hardware cost. Overhead shall also be included in case of subcontracting.

This budget estimate also excludes the costs required for:

- The diagnostics and X-Ray optical components to characterize the photon beam (flux, energy, energy spectrum...)
- The building and associated infrastructure (cooling station, power station, air conditioning, lighting…)
- The radioprotection (shielding, personnel safety system, radiation monitors,.),
- The transportation
- The industrialization costs.

ThomX parts cost estimate:

Photoinjector Gun	422
LINAC	1176
Transport Line	219
Ring	1919
Fabry Perot	339
Laser and fiber amplifier	246
Control-Synchro & Services	490
Infrastructure & cabling	200
X ray beam extraction and characterisation	200
Spares	222
total cost for parts (k€ - VAT excluded) [3]	**5433**

7.4] Industrialization

Industrialization can be split into two main tasks:

- Adaptation of the ThomX performance to specific requirements
- Adaptation of the ThomX machine to meet industrial standard criteria

Adaptation of the ThomX performance to specific requirements

The main trends will be:

- To increase the instantaneous and/or total flux : this will be performed by optimisation of the parameters of the ThomX machine and careful control. In particular the interaction area will be minimized as well as the photon flux within the Fabry Perot cavity.
- To increase the X-ray photon energy: this will be done by increasing the electron beam energy and/or adapting the Fabry Perot design to operate at 532 nm.
- To tune the machine to various X-ray energies : this will be done by setting the LINAC energy accordingly and by optimizing the associated ring parameters
- To condition the X-ray output to specific needs. Various techniques to monochromatize or to control the X-ray beam can be used but have to be adjusted on a case by case basis depending on the requirements.
- To decrease the X-ray pulse duration

Adaptation of the ThomX machine to meet industrial standard criteria

The industrial criteria are also key parameters for acceptance by a customer. Among them are the following:

- Availability:

---

[3] no provision for risk has been taken

The availability of an industrial system depends on two issues

  - Reliability:

    Usually reliability issues arise during the first operation period, ThomX extensive tests will permit to localize potential weak points in the design or in the technology choices.

  - Maintainability:

    Preventive maintenance associated with tele-diagnostics and local spare parts will minimize the fault risks and will shorten the repairing time. The training of the people who will perform operation and preventive maintenance is also very critical to achieve optimal availability

- Ease of use

The command control shall be easy to use, even for non expert. In particular no action leading to catastrophic issue shall be permitted by the system. In case of a defect, clear information and guidance shall be provided to the operator

- Performance

Required performance depends on the application and shall be adjusted with the simpler possible architecture. R&D beyond ThomX delivery will be necessary to implement some of them. Part of ThomX operation time shall be kept for such developments..

- Affordability

Effort shall be made to lower the machine cost since the present ThomX cost is too high (or the potential application not enough mature) to lead to large machine production.

ThomX machine design shall meet these criteria whenever possible (i.e. whenever this can be done without risks increase or performance degradation) and the remaining extra works have to be planned to prepare the industrialization phase whenever these criteria are not fully met by the initial ThomX machine.
In particular the low operating voltage and high modularity policy already experienced for the RF power source of SOLEIL will be expanded to the klystron modulator.

Annexe 1: Main source parameters

INJECTOR LINAC	
RF GUN	
Charge per bunch [nC]	1
Number of bunches per train	1 - 4
Normalised r.m.s. emittance [π mm mrad]	5
R.m.s. energy spread [%]	< 1%
R.m.s bunch length [ps]	< 5
RF linac frequency (MHz)	2998
Repetition frequency [Hz]	50 - 100
Q_0	15244
Shunt impedance [MW/m]	54
Peak power [MΩ]	4
τ [μs]	81
LINAC	
Linac Energy [MeV]	50.
Normalized r.m.s. emittance @ extraction (π mm.mrad)	4.2
Non-normalized r.m.s. emittance @ extraction (π mm.mrad)	0.0426
R.m.s. transverse sizes @ extraction (x/y) [mm]	1.2
R.m.s. bunch length [ps]	4.6
R.m.s. energy spread [%]	0.68
TRANSFER LINE FOR INJECTION BEAM MATCHING	
Chicane compression factor R56 [m]	- 0.3
RF redresser gradient [MV]	2
RF redresser frequency [GHz]	3
RF redresser phase [degrees]	90
STORAGE RING	
GENERAL CHARACTERISTICS	
Circumference [m]	14.47
Nominal energy [MeV]	50
Period [ns]	48.5
Synchrotron frequency [kHz]	498.7
Revolution frequency [MHz]	20.7
Betatron tunes ν_x, ν_z	3.4, 1.4
$\beta_{max\ x,z}$ [m]	11, 11
Max dispersion function [m]	0.9
$\beta^*_{x,z}$ [m], beta function @ IP [m]	0.1, 0.1
R.m.s. transverse size @ IP [μm]	70

Dispersion function @ IP [m]	0
Momentum compaction factor α	0.0148
Max current : I_b [mA]	20.83 mA
Natural chromaticities $_{x,z}$	-3.2, -8.2
RF SYSTEM	
RF frequency [MHz]	500
Harmonic number	24
Peak accelerating voltage [kV]	500
RING MAGNETS	
Dipole number, family & field [T]	8 / 1 / 0.5
Dipole current per coil [A turns]	8000
Dipole gap radius [mm]	40
Dipole iron length [mm]	300
Dipole weight [kg]	260
Dipolr cooling	Yes
Quadrupole number, families & field [T/m]	24 / 6 / <3
Quadrupole current per coil [A turns]	360
Quadrupole gap radius [mm]	50
Quadrupole iron length [mm]	150
Quadrupole weight [kg]	60
Quadrupole cooling	No
Sextupole number, families & field [T/m^2]	12 / 2 / <30
Sextupole current per coil [A turns]	120
Sextupole gap radius [mm]	50
Sextupole iron length [mm]	60
Sextupole weight [kg]	10
Sextupole cooling	No
Kicker deviation [degrees], [rad]	1.5, 0.0262
Kicker field integral [mT m]	4.4
Kicker field [mT]	8.7
Kicker peak current [A]	449
Kicker charging voltage [kV]	24
Kicker coating thickness [nm]	20-40
Septum deviation [degrees], [rad]	7, 0.1222
Septum field integral [mT m]	20.4
Septum field [mT]	68
Septum peak current [A]	810
Septum charging voltage [kV]	0.096
VACUUM SYSTEM	
Design vacuum pressure [Pa]	$< 3\ 10^{-7}$
Diameter of the beam pipe [mm]	40
Specific conductance of the beam pipe [m^3 m s^{-1}]	0.0079
Dimensions of the rectangular chamber of the optical cavity [mm x mm]	25 x 85
Specific conductance of the optical cavity rectangular chamber [m^3 m s^{-1}]	

LASER AND CAVITY SYSTEM – IP	
Number of photons/pulse	$1.6012\ 10^{17}$
R.m.s. transverse size [μm]	40
R.m.s. longitudinal size [ps]	1
Wavelength [μm]	1.06
Angle between electron bunch trajectory and the laser one [degrees], [rad]	2, 0.0349
COMPTON BACKSCATTERING RADIATION CHARACTERISTICS	
Thomson cross section [m^2]	$6.66\ 10^{-29}$
Initial flux [photons s^{-1}]	$1.2\ 10^{13}$
Energy loss per electron and per turn [eV]	2.3
Maximum, mean energy of CBS radiation [keV]	50, 25
Period [ns]	48
Transverse damping time [s]	2.1
Longitudinal damping time [s]	1.1
Equilibrium energy spread [%]	1.8
Equilibrium non-normalised Emittance [p mm mrad]	$6.9\ 10^{-8}$
Transverse damping time with synchrotron radiation [s]	1.2s
Longitudinal damping time with synchrotron radiation [s]	0.6 s
Equilibrium energy spread with synchrotron radiation [%]	1.4 %
Equilibrium non-normalised emittance with synchrotron radiation [π mm mrad]	$6.5\ 10^{-8}$
SYNCRONIZATION CONSTRAINTS	
Bunch injection time with respect to the ring synchronous phase [ps]	13
Bunch and photon bunch running through the interaction region [ps]	10
Linac photocathode laser pulse with respect to the linac RF phase [ps]	1
ALTERNATIVE SOURCES CHARACTERISTICS	
SUPERCONDUCTING LINAC – ENERGY RECOVERY LINAC	
Energy {MeV]	53
R.m.s. transverse emittances [π.mm.mrad]	6.6
R.m.s. energy spread [%]	0.7
R.m.s. bunch length [mm]	3.3
Bunch charge [nC]	0.3
Repetition rate [MHz]	80
Mean Current [mA]	24
Expected X Ray flux [photons sec^{-1}]	$2.2\ 10^{13}$

Annexe 2: Costing

ThomX SYSTEM MAIN EQUIPMENT BREAKDOWN	quantity	unit cost	intermediate cost	subassembly cost
		(k€ - VAT excluded)		
Photoinjector Gun				**422**
Girder	1	15	15	
Gun cavities	1	20	20	
Gun magnets	2	10	20	
Gun magnet power supplies	2	30	60	
Laser and optical beam transport	1	150	150	
preparation chamber	1	120	120	
Vacuum				
Ionic pumps	1	7	7	
Vacuum Vanes	1	5	5	
Diagnostics				
Integrating current transformer	1	25	25	
LINAC				**1176**
Accelerating section	1	180	180	
Injector girder	1	15	15	
Waveguide feeder	1	20	20	
Timing and LPRF cabinet	1	85	85	
low power 3 GHz reference	1	20	20	
3 GHz Amplifier	1	40	40	
RF measurement	1	10	10	
Vacuum & cooling cabinet	1	110	110	
Magnet supply cabinet	1	5	5	
Klystron Amplifier				
Klystron with coil	1	200	200	
Modulator	1	300	300	
Coil power supply	1	30	30	
RF waveguide	1	30	30	
RF Circulator	1	30	30	
RF Phase Shifter	1	20	20	
Diagnostics				
Integrating current transformer	2	25	50	
Vacuum				

Ionic pumps	3	7	21	
Vacuum Vanes	2	5	10	
Transport Line				**219**
Girder	1	15	15	
Beam pipe	1	10	10	
Diagnostic				
Integrating current transformer	1	25	25	
Vacuum				
Ionic pump	1	7	7	
Vacuum vane	2	5	10	
Dipole 45°	4	13,5	54	
dipole power supply	1	10	10	
Dipole 8°	1	7	7	
dipole power supply	1	10	10	
Quadripole	5	4,2	21	
quadripole power supply	5	10	50	
Ring				**1918,6**
Girder	1	22	22	
Beam pipe	1	20	20	
Dipôles	8	13,5	108	
Dipôle power supply	1	10	10	
Quadripôles	24	4,2	100,8	
Quadripôle power supply	6	10	60	
Vacuum	1	150	150	
Ionic pumps	3	7	21	
Vacuum Vanes	2	5	10	
Sextupoles				
Type 1 (8)	8	3,9	31,2	
Sextupôle T1 Power Supply (1)	1	10	10	
Type 2 (4)	4	3,9	15,6	
Sextupôle T1 Power Supply (1)	1	10	10	
RF 500 MHz cavity (1)	1		300	
LLRF (MO,distribution,réguls,mesures)			100	
RF 40 kW amplifier			150	
Diagnostics			500	
Pulsed elements			300	
Fabry Perot	1	300	300	**339**
Optical table	1		0	
Mirror vessel	2		0	

Mirror positioning system	2		0	
Vacuum				
Vacuum vanes	3	5	15	
Ionic pump	2	7	14	
Beam pipe	1	10	10	
Laser and fiber amplifier				**246**
Low noise ps oscillator	1	80	80	
Optical table	1	4	4	
Large core microstructured Yb doped fiber	3	10	30	
Wavelengths stabilized diodes	1	30	30	
Optics	1	20	20	
Mounts and mechanics	1	20	20	
VBG	2	6	12	
Diagnostics	1	30	30	
Custom mechanics	1	20	20	
Others				**490**
Command Control	1		200	
Synchronization			50	
Cooling system	1	180	180	
Beam dump	2	30	60	
Infrastructure & cabling			200	**200**
Spares				**222**
Gun magnet power supplies	1	30	30	
Ionic pumps	1	7	7	
Vacuum Vanes	1	5	5	
Dipôle power supply	1	10	10	
Quadripole Power Supply	1	10	10	
Sextupôle T1 Power Supply (1)	1	10	10	
various optical parts	1	50	50	
various electronics parts	1	50	50	
various mecanical parts	1	50	50	
X ray beam extraction and characterisation		200	200	**200**
				Total cost
				5433

CONCLUSIONS

There is an industrial and scientific growing interest in bright monochromatic and tunable X-ray sources. These sources are being widely used in various research, medical, technology and industrial fields. Synchrotron Radiation (SR) is currently the primary high quality X-ray source that satisfies both brilliance and tunability. The high cost, large size of SR facilities are however serious limitations for a large local diffusion of these devices. There are compact (or even table-top) X-ray sources already in use, as X-ray tubes or experimental exotic sources using moderate electrons energy interacting periodic layer structures. However, these sources suffer from a modest photon flux and that the emitted photons energy is relatively low. Nevertheless, recent results have shown that laser Compton Back Scattering (CBS) with relativistic electrons can produce directional, quasi-monochromatic and polarized photon beams with intensity order of magnitude higher than these already existing compact sources. In this latter process, the backscattered photon from an eV laser is kinematically boosted up to the keV range also taking into account moderate electron energy (few MeV). X-ray sources based on this process may become inexpensive and attractive.

Based on the combined recent progress in both accelerator and laser technologies, we propose a compact CBS X-ray able to produce an X-ray flux in the region of 10^{13} ph/s. The photon energy spectrum cut off is ~ 50 keV. To meet this high flux, both electron bunch and laser pulse are stacked respectively in a compact ring and a high gain optical cavity. The laser-electron interaction occurs at each revolution (20 MHz) by means of a dedicated synchronisation system. The photon pulse in the high gain Fabry-Pérot cavity is continuously injected by a laser system of high average power (100 W).
As consequence, the stacked pulses energy increases up to a few mJ (typically 25 mJ). The electron bunches are delivered by RF gun followed by a 3 GHz warm linac at an energy of 50 MeV. At this low energy the cumulative injection in the same bucket of the ring is not possible since the synchrotron damping time is longer that the instabilities growing time. Hence, a high charge (~ 1 nC) and low emittance (5 mm.rad) is directly injected in the ring. As mentioned, at this low energy and high charge bunches, the dynamics in the ring is very sensitive to various perturbations (collective effects, intra beam scattering, CBS recoil effect, etc ...). As a consequence, to prevent from X-ray flux degradation, we estimate that the electron bunches have to be stored to a maximum of about 20 ms. They are then renewed with a rate of 50 Hz. For this purpose, we design a compact dedicated storage ring (Circ= 15 m) with an original CBS interaction scheme located in between dipoles. It offers the advantages to free the long straights sections, to locate the optical mirror outside of the ring and to have the X-ray extraction cone close to the interaction point. Therefore, a dedicated optical cavity design has been provided taking into account the different integration constraints. It is based on a 2D crossed geometry that naturally accommodates the ring dipole gap geometry.

All the subcomponents, from the electron RF gun to the Fabry-Pérot cavity as well as the laser systems of the proposed machine, are very performing but they are widely in use in various facilities. The real challenge will be the locking of the high power laser with a very high finesse optical resonator and, to meet the high flux X-ray, the high electron charges and laser pulse energy stored respectively in the ring and the optical cavity. It is then strongly advised to consider a gradual approach for the commissioning phases.
The construction of this machine will strongly benefit of the momentum provided by the "Plan Campus", a special operation launched by the French government to upgrade

infrastructure facilities in the Orsay campus. The building in which the prototype will be installed will be refurbished starting in 2010, starting with the necessary electrical power plant, ground preparation and clean room assembly. LAL infrastructure teams will be fully mobilised to accomplish these various tasks.

The commissioning of this machine will require a lot of careful coordination and a detailed plan will be prepared well in advance to optimize its strategy. It will also be a very exciting adventure that will attract many students, engineers and physicists. We are therefore really looking forward this exciting goal.

INDEX